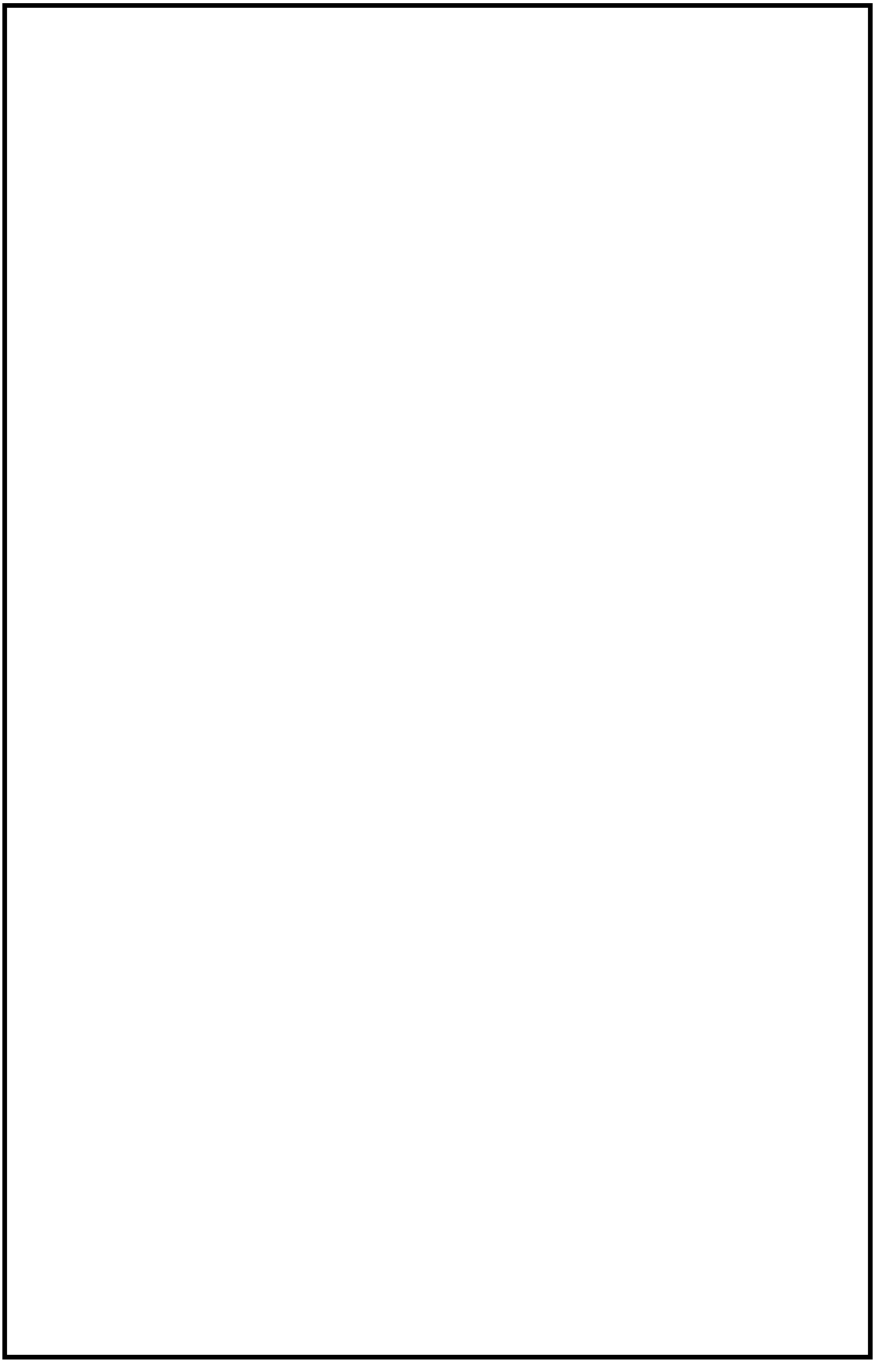

Measuring the Partonic Orbital Angular Momentum in the Proton from Two Particle Azimuthal Correlations at PHENIX in Run3pp

by

Robert F. Hobbs

D.E.U.G. Physique, Université Louis Pasteur, 1991
Licence de Physique, Université Louis Pasteur, 1992
Maîtrise de Physique, Université Louis Pasteur, 1993

DISSERTATION

Submitted in Partial Fulfillment of the

Requirements for the Degree of

Doctor of Philosophy
Physics

The University of New Mexico

Albuquerque, New Mexico

May, 2006

Dedication

To my wife Kimberly and my son Zachary.

Acknowledgments

I would like to thank all members past and present of the University of New Mexico Medium Energy Physics group, specifically Bernd Bassalleck, Doug Fields, Jan Rak, Imran Younus, and Nicki Bruner. I would also like to thank the entire PHENIX collaboration, and in particular the members of the Muon Working Group and the Spin Working Group. Finally I would also like to thank my dissertation committee members not already mentioned, Michael Gold and Musoumi Roy as well as Martin Hoeferkamp, electrical engineer at UNM.

Measuring the Partonic Orbital Angular Momentum in the Proton from Two Particle Azimuthal Correlations at PHENIX in Run3pp

by

Robert F. Hobbs

ABSTRACT OF DISSERTATION

Submitted in Partial Fulfillment of the
Requirements for the Degree of

Doctor of Philosophy
Physics

The University of New Mexico

Albuquerque, New Mexico

May, 2006

Measuring the Partonic Orbital Angular Momentum in the Proton from Two Particle Azimuthal Correlations at PHENIX in Run3pp

by

Robert F. Hobbs

D.E.U.G. Physique, Université Louis Pasteur, 1991

Licence de Physique, Université Louis Pasteur, 1992

Maîtrise de Physique, Université Louis Pasteur, 1993

Ph.D., Physics, University of New Mexico, 2006

Abstract

By measuring the azimuthal correlations between two high p_T hadrons, one can extract jet properties such as the fragmentation transverse momentum j_T and the intrinsic transverse momentum k_T. In longitudinally polarized p+p collisions, differences in the extracted average k_T for parallel and anti-parallel helicity combinations (double asymmetry) may give information on the relationship between the polarization and k_T, and the orbital angular momentum of the hard-scattered partons. In this dissertation we present the theoretical motivation, physics technique, analysis method, Monte Carlo modeling and simulation, and results of the analysis for π^0 - $h^{\pm}$ azimuthal correlations in PHENIX with data from Run3 at RHIC.

Contents

List of Figures

List of Tables

List of Tables

Chapter 1

Introduction

The study we propose to make supposes a ready knowledge of a very specific field: spin physics. Spin physics is a branch of experimental (and theoretical) particle physics; in order to ease the non-expert reader gently into the subject matter we will begin with a review of experimental particle physics, laying a heavy accent on the information relevant to spin physics and more particularly to the present analysis.

1.1 High Energy Particle Physics

Particle physics deals with the study of the elementary constituents of matter. The word "elementary" is used in the sense that such particles have no known structure, they are considered to be pointlike. How pointlike is pointlike? That depends on the spatial resolution of the probe used to investigate the possible structure. The spatial resolution of a beam of momentum p is given by:

$$\Delta r \approx \frac{h}{p \sin\theta} \tag{1.1}$$

where θ is the viewing angle of the probe to the target and Δr is the distance between elements that are to be distinguished. In the early 20^{th} century, particle beam energies from accelerators reached only a few MeV , and their resolution was so poor that protons and neutrons could be considered pointlike. Today the fundamental particles appear to be quarks and leptons, unified in what is called the Standard Model.

1.1.1 Experimental Setups

Two types of experiments exist as shown in Fig. 1.1.

1. An accelerated beam on a fixed target can be used for the production of a secondary beam of relatively short-lived particles for kinematic reasons, or, if a particular aspect of the fixed target (like polarization) is difficult to achieve in a beam. The center of mass energy available for particle production is:

$$\sqrt{s} = \sqrt{2m_t E} \tag{1.2}$$

where E is the energy of the beam particles and m_t the mass of the target particles. The rest of the energy goes into the kinetic energy of the produced particles. Early experiments in spin physics would use fixed targets of polarized protons and a beam of accelerated leptons.

2. For beam-beam collisions the center of mass energy available for particle production is:

$$\sqrt{s} = 2E \tag{1.3}$$

with E the energy of each beam (assuming equal energies). This type of collision also has the advantage of spreading out the region of particle production

more evenly over all of space instead of focussing the created particles mainly in the forward region. This enables easier characterization but often requires more detectors.

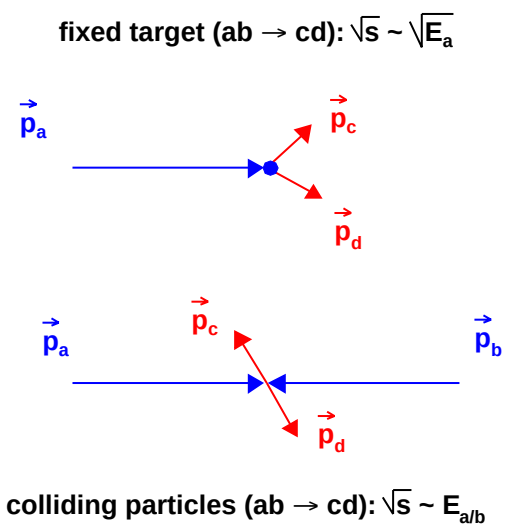

Figure 1.1: The two basic types of colliding particle experiments: fixed target and center-of-mass collisions.

In either type of collision a physical quantity that is of paramount importance is the luminosity. It is a measure of the amount of beam and the expected number of collisions. If two beams cross, or a beam collides with a fixed target, the probability for an interaction is proportional to the intensity of the beam(s) and the density of the target material. For an intersecting storage ring collider (the case of the present analysis) the luminosity is given by:

$$L = fn\frac{N_1 N_2}{A} \tag{1.4}$$

where f is the revolution frequency, n the number of bunches in the ring, N_i the number of particles in each beam, and A is the cross-section of the beam. Luminosity is given in units of inverse surface area per unit time. The integrated luminosity $\hat{\mathcal{L}}$ is a quantity that is quoted even more frequently and is given by:

$$\hat{\mathcal{L}} = \int L(t)dt \tag{1.5}$$

Integrated luminosity is given in units of inverse area, usually pb^{-1}, nb^{-1} or μb^{-1} where b is a barn $= 10^{-28}m^2$. By multiplying $\hat{\mathcal{L}}$ by the cross-section for a particular process or particle, the number of corresponding processes or particles, respectively, is obtained:

$$N = \hat{\mathcal{L}} \cdot \sigma \tag{1.6}$$

1.1.2 The Standard Model

In 1964 Gell-Mann and Zweig posited the existence of quarks to explain the hadronic "zoo", the large number of strongly interacting particles that had been created in the 1950's and 1960's by higher and higher energy particle accelerators. Quarks have flavor, fractional charge, spin $\frac{1}{2}$, and later it was discovered, a new quantum number called "color".

There are three colors labeled: red, blue and green. Quark combinations can only exist in colorless states: 3 differently colored quarks form a baryon; a colored quark and an anti-quark with the corresponding anti-color form a meson. Baryons and mesons together are called hadrons.

Practically all experimental data from high energy experiments can be accounted for by the Standard Model of particles and their interactions. All matter is made of

six quarks and six leptons plus their anti-particles. The quarks feel the strong nuclear force, the leptons do not. The charged particles feel the electromagnetic force and they all feel the weak nuclear force and gravity. All these particles are fermions because they are spin $\frac{1}{2}$ particles; they are categorized in Table 1.1. Strangely, these particles are grouped into three families, each identical to the other except for the particles' mass and flavor.

Family 1	Family 2	Family 3	$Q/\|e\|$
electron (e)	muon (μ)	tau (τ)	-1
e-neutrino (ν_e)	μ-neutrino (ν_μ)	τ-neutrino (ν_τ)	0
up quark (u)	charm quark (c)	top quark (t)	$+\frac{2}{3}$
down quark (d)	strange quark (s)	bottom quark (b)	$-\frac{1}{3}$

Table 1.1: Standard Model fermions. The first two rows are leptons, the second two rows are quarks. The columns represent the "families" of particles.

The Standard Model also includes the interactions between particles. The forces are described in quantum language as the exchange of bosons (spin 1 particles) between the fermions (see Table 1.2).

In 1969 after the discovery of point-like particles within the proton, R. Feynman invented the "partonic model" to describe experimental results [1]. Partons are found to have quark-like properties, and eventually partons become a term used for quarks and the vector bosons that carry the color charge, the gluons.

Force	Particle	Relative Strength
Strong	gluon (G)	1
Electromagnetic	photon (γ)	$\frac{1}{137}$
Weak	$Z^0, W^{\pm}$	10^{-7}
Gravity	graviton (g)	10^{-39}

Table 1.2: Standard Model bosons. Note that the graviton (g) has spin 2, not spin 1 as the others do.

1.2 The Proton

In this quark model the proton is a baryon, composed of two up quarks and a down quark (Fig. 1.2). The three quarks each carry one of the three colors and by assigning a spin up for two quarks and spin down for the third many of the physical attributes of the proton can be explained:

- It's charge is the sum of the three quark charges:

$$Q = \frac{2}{3}e + \frac{2}{3}e - \frac{1}{3}e = e \tag{1.7}$$

- It is colorless because of the red-green-blue color combination.

- At first glance a simple sum of quark spins would appear to give the proton its spin:

$$S_z = \frac{\hbar}{2} + \frac{\hbar}{2} - \frac{\hbar}{2} = \frac{\hbar}{2} \tag{1.8}$$

- Even a more complicated derived product such as the magnetic moment appears to be explained by the simple model [2]. The magnetic moment of the proton could be written as a sum of the magnetic moments of the three quarks. To do so the wave function of the polarized proton would first be written as the normalized linear combination of the different spin (2↑,1↓)- flavor (uud)-color (colorless) combinations:

$$\begin{aligned} P^{\uparrow} = \; & \tfrac{1}{\sqrt{18}}\left(2u_r^{\uparrow}u_b^{\uparrow}u_g^{\downarrow} + 2u_b^{\uparrow}u_g^{\uparrow}u_r^{\downarrow} + 2u_g^{\uparrow}u_r^{\uparrow}u_b^{\downarrow} + u_r^{\uparrow}u_b^{\downarrow}u_g^{\uparrow} + u_b^{\uparrow}u_r^{\downarrow}u_b^{\uparrow}\right. \\ & \left. + u_b^{\uparrow}u_r^{\downarrow}u_g^{\uparrow} + u_r^{\uparrow}u_b^{\downarrow}u_g^{\uparrow} + u_g^{\uparrow}u_r^{\downarrow}u_b^{\downarrow} + u_r^{\uparrow}u_g^{\downarrow}u_b^{\downarrow}\right) \end{aligned} \tag{1.9}$$

  from this equation we deduce that the magnetic moment of the proton would be:

$$\mu_P = \frac{4}{3}\mu_u - \frac{1}{3}\mu_d \tag{1.10}$$

  where the magnetic moments of the quarks are given by:

$$\mu_q = \frac{Q_q}{2m_q} \tag{1.11}$$

  with Q_q the charge of the quark, and m_q the mass of the quark obtained by attributing a third of the mass of the proton for each quark, which of course ignores binding energy. The value for the proton's magnetic moment thus obtained is $2.79nm$ which is in remarkable agreement with the measured value of $2.7928456nm$ obtained experimentally [3].

Why does this model not stand up to closer scrutiny? The answer to this question lies with Quantum Chromodynamics (QCD), the theory of quarks and gluons which describes all strong-interaction experiments at all energies, high and low.

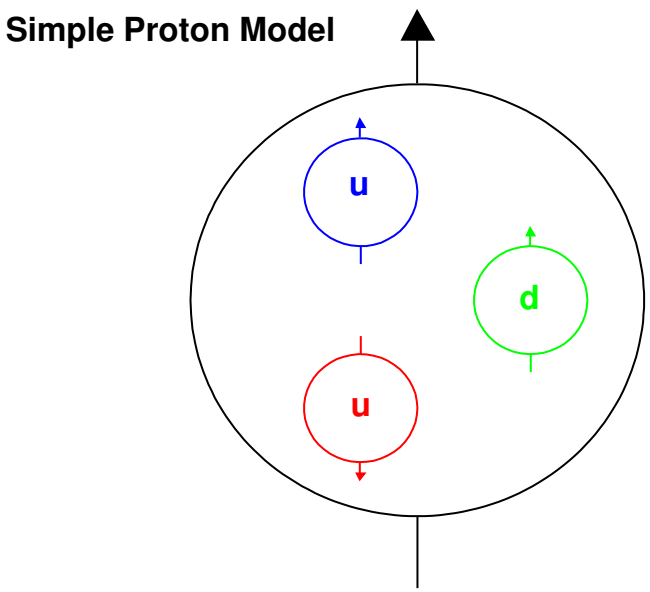

Figure 1.2: The simple quark model of the proton

1.3 Quantum Chromodynamics

The Standard Model is a well established theory applicable over a wide range of conditions. Beyond the simple cataloging of particles, it combines two theories of particle physics into a single framework to describe all interactions of subatomic particles, except those due to gravity. These two components of the Standard Model are Electroweak theory, which describes interactions via the electromagnetic and weak interactions, and Quantum Chromodynamics (QCD).

To understand the effects and workings of QCD a quick comparison with QED (Quantum Electrodynamics) is useful:

- Photons couple to electric charge, but are chargeless themselves. Gluons couple

to and carry color. Therefore gluons can interact with each other.

- The coupling constant for the strong force is $\alpha_S \approx 1$ while the coupling constant for the electromagnetic force (QED) is $\alpha \approx 1/137$. This means that higher order diagrams in QCD as illustrated in Fig. 1.3 carry as much probability weight as the lower order diagrams, unlike QED.

The consequences of these are twofold: Asymptotic Freedom and Confinement. In fact the strong coupling constant is misnamed. It is not really constant, but varies as a function of the distance between interacting particles. This is also known as the running of the coupling constant α_s. At low momentum transfer and large distance α_s is much stronger (and effectively ≈ 1) than at small distances and high momentum transfer. Asymptotic Freedom refers to the weakness of the short-distance interaction (high energies). Confinement on the other hand, follows from the fact that strong interaction is very strong at long distances (low energies), with $\alpha_S \approx 1$. The detailed evidence for the coexistence of Asymptotic Freedom and Confinement in QCD is based on a complicated web of analytical and numerical results and inferences.

At close distance then, calculation of cross-sections from Feynman Diagrams is possible. This regime is known as perturbative QCD (pQCD). Non-perturbative QCD is essentially concerned with the composite hadrons. It models the formation of hadrons, the structure of hadrons and interactions between the different hadrons. The crux of the problem with QCD is that although it is able to accurately explain many strong phenomena, it leaves some issues unresolved. For example, although the necessity of having colorless hadrons explains the baryon and meson structure it does not explain why no other colorless combinations, such as dibaryons, dimesons, pentaquarks or others have been observed.

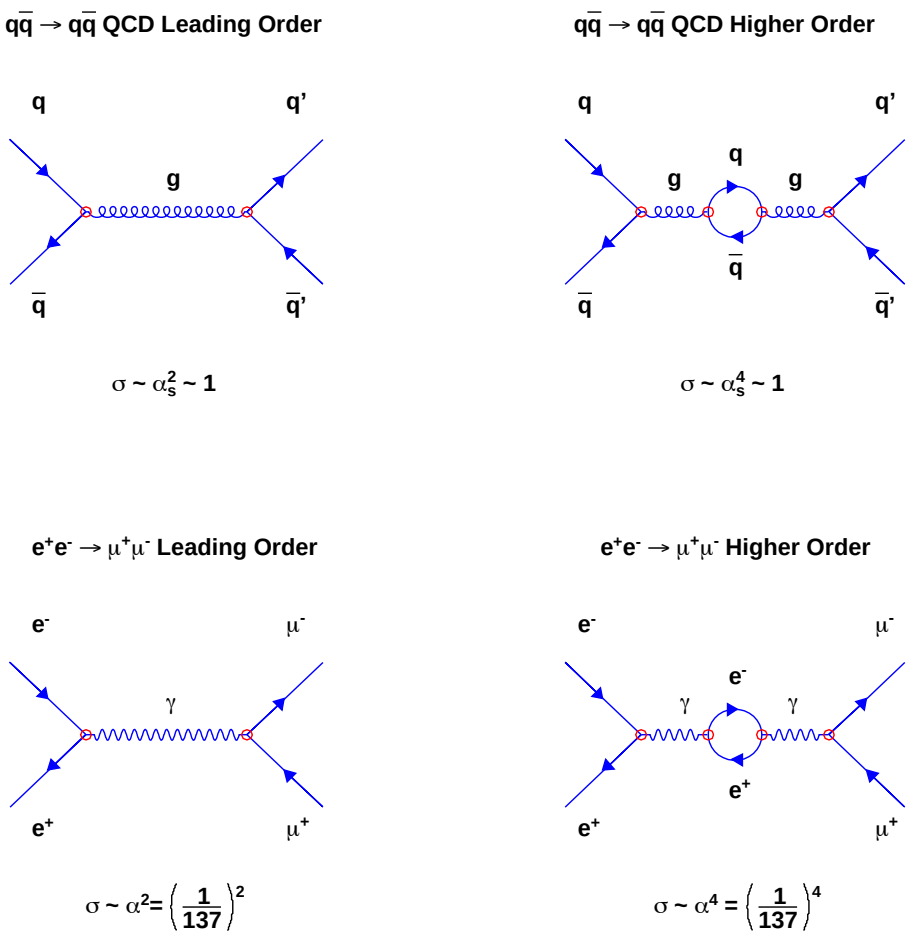

Figure 1.3: QED and QCD Feynman Diagrams. The probability amplitude of a particular diagram is proportional to the factors that are given by each particle line and vertex. Each vertex carries a $\sqrt{\alpha}$ factor, so that higher order processes, even though they are more numerous occur less frequently in QED because of this attenuation factor. This is not true in QCD as $\alpha_S \to 1$. The cross-section for a particular diagram is then the square of all these factors.

Another way of looking at these attributes is to consider the potential:

$$\begin{cases} \text{QED:} & V & = & -\frac{\alpha}{r} \\ \text{QCD:} & V_s & = & -\frac{4}{3}\frac{\alpha_s}{r} + kr \end{cases} \tag{1.12}$$

The second term in the QCD potential acts like a spring, the greater the distance, the stronger the attractive force. When separating two electrically charged particles, the number of field lines remains the same, so the density diminishes and so does the force. The field lines between quarks can be thought of as strings; when the quarks are pulled apart the lines come together forming a dense flux tube. At the limit of the strings' length it is impossible to pull the quarks apart without breaking them. In doing so enough energy is provided to create $q\bar{q}$ pairs from the vacuum so that each quark now has a new, closer neighbour to interact with. The result is that no quark has ever been seen alone, they always come contained in baryons (qqq) or mesons ($q\bar{q}$). The process of creating such particles by breaking quarks (or gluons) apart is called hadronization or fragmentation. The probability of a particular flavor of parton hadronizing in a certain way is given by Fragmentation Functions (FFs). Fragmentation Functions are determined by matching the experimental data to various models [4].

If the process is hard enough a number of particles will be created, all of which will move in approximately the same direction as the original interacting parton. This is called a jet (see Fig. 1.4).

The results of this more in depth look at the strong force means we must modify our picture of the proton:

- In addition to the three quarks that carry the quantum numbers (valence quarks), the proton is composed of gluons which carry the force as well as quark - anti-quark pairs that are constantly appearing and disappearing (sea quarks).

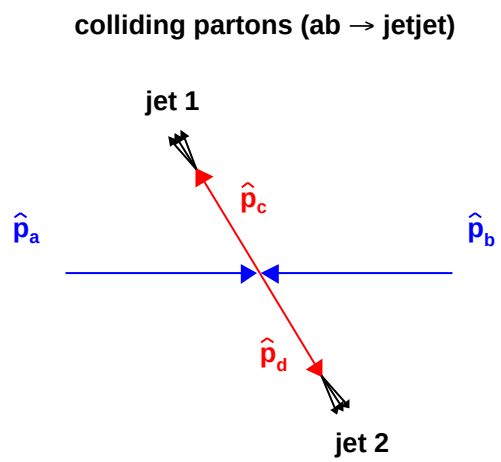

Figure 1.4: Jet-jet production cartoon. Two colliding partons result in two jets. Note that jet momentum is conserved: $\hat{p}_c = \sum_i \vec{p}_{jet1}$ and $\hat{p}_d = \sum_i \vec{p}_{jet2}$.

- The mass of the quarks cannot be considered to be 1/3 of the mass of the proton.
- The simple model for magnetic moments has no Confinement. The effective radius of the proton is infinite and therefore invalidates the calculation (yet it is still an intriguing result).

1.4 Initial and Final State Variables

One of the fundamental problems in particle physics is obtaining information about the initial colored partons from the measured physical quantities of the colorless

hadrons. In other words, describing initial state variables as a function of final state variables.

1. Some of the most often used initial state variables that relate to our analysis include:

   - Momentum fraction

     When two protons collide, the interaction takes place at the partonic level. In actuality, it is as if two partons (quarks or gluons) collide. The parton carries momentum, and the momentum fraction is defined as:

     $$x_i = \frac{P_i}{P_p} \tag{1.13}$$

     with P_p being the momentum of the proton and P_i the parton momentum. Many of the physical quantities which we are seeking to determine depend on this quantity.

   - Intrinsic partonic transverse momentum: k_T

     This is the initial variable that interests us the most in this analysis. The parton has intrinsic transverse momentum (perpendicular to the beam momentum) k_T which may or may not be in part correlated with spin direction.

   - Partonic spin direction.

     Up or down for quarks. Up, down or zero for gluons. For this initial variable we know the spin of the proton (or at least the polarization, see below) and we try to correlate spin of the various flavors of quarks and of the gluons to the spin of the proton. Note that for longitudinally polarized protons, *i.e.* polarized in the direction of momentum, the nomenclature for spin is replaced by that for helicity.

- Helicity.

  Although it has general usage, it is used essentially in this dissertation instead of spin direction (partonic or protonic) for longitudinally polarized particles. Helicity is defined as:

  $$H = \frac{\vec{\sigma} \cdot \vec{p}}{|\vec{p}|} = \pm\frac{\hbar}{2} \tag{1.14}$$

  the last equation is valid for spin $\frac{1}{2}$ particles. The particle is said to posess positive or negative helicity. Moreover, two colliding beams which have the same helicity are said to have parallel helicity, and colliding beams that have opposite helicities are said to have anti-parallel helicity.

- Polarization.

  This is a measure of the spin orientation of a beam in a given direction. Basic quantum mechanics tells us that the spin of a spin $\frac{1}{2}$ particle measured in a given direction will be one of two possible outcomes: $\pm\frac{\hbar}{2}$, or more simply, either in the positive or in the negative direction of the axis along which the spin is being measured. As the chance for an individual particle to be measured in either the positive or negative direction is 50%, for a large number of such particles, the outcome will be 50% in the positive direction and 50% in the negative. A beam is polarized if there exists an imbalance in the number of spin-up (+) versus spin-down (-) particles where the spin may be projected onto any direction, be it longitudinal, transverse, or other. The formula for polarization is:

  $$P = \frac{N_+ - N_-}{N_+ + N_-} \tag{1.15}$$

  Thus, polarization of 100% means all spin-up (or spin-down), and a polarization of 0% means half up and half down.

- Impact parameter.

The distance b between the center of mass of the two colliding protons in the transverse plane.

- Angle β between the centers of mass of the two protons projected into the transverse plane as measured from the x-axis, *i.e.* the relative orientation of the protons at the time of collision.
- Angle κ of the $\vec{k}_{T\text{pair}}$ due to the sum of the two partonic $\vec{k}_T$, also measured from the x-axis in the transverse plane.
- The angle ζ of the outgoing partons and jets in the transverse plane as measured from the x-axis. This is not strictly speaking an initial state variable, neither is it a final state variable. Moreover, it is a theoretical quantity which exists only in the absence of k_T.

Three of the last parameters; b, β, κ (see Fig. 1.5) have so far proven difficult to characterize, although theoretical modeling attempts are currently underway. Knowledge of these three parameters would vastly improve the quality of analyses such as ours; it is more likely, however, that in the near future these analyses will contribute to a better understanding of these parameters rather than the other way around. The final parameter is closely related to the azimuthal angular position of detected particles. In and of itself, it is not particularly useful. If there are correlations to be found for spin physics they are most likely to be functions of $\kappa - \zeta$.

2. Final state variables include: total momentum, energy, charge, and location of the detected particles as well as some not quite so obvious ones such as:

   - Transverse Momentum: p_T

     While the concept of momentum in the transverse direction is a fairly straightforward one, it isn't necessarily a concept that is à priori important enough to warrant discussion. It is important for the simple reason

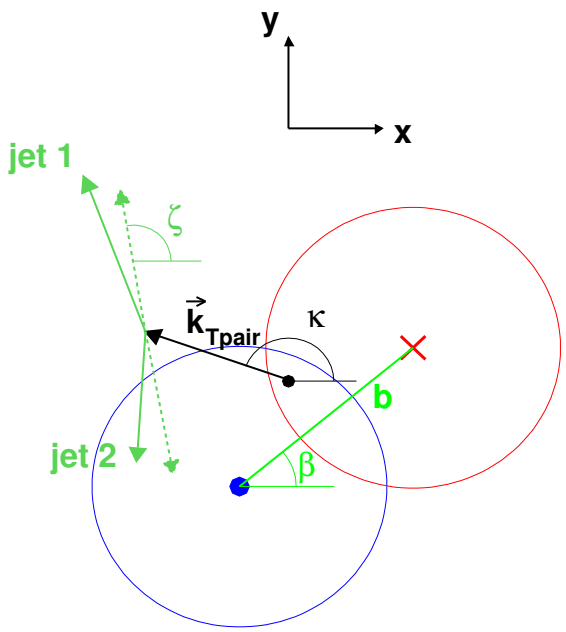

Figure 1.5: This diagram shows the collision of two protons in the transverse plane. The black dot represents the collision point. The parameters b, β, κ, and ζ are shown. All three angles are measured from the x-axis. ζ is the theoretical angle of the k_T-free jet-jet direction. Note that the $\vec{k}_{T\text{pair}}$ vector is not drawn to scale in order to space out the elements in the diagram.

that although much energy goes into each collision, conservation of momentum tells us that the net momentum is zero and that the momentum of each proton is along the beam axis (in the plus z-direction and minus z-direction, respectively) before collision. Traditionally (without considering k_T), any momentum in the transverse plane comes from the interaction in the collision itself, from a transfer of longitudinal momentum p_z to p_T. Regardless of the origin, any p_T gained must be matched by an equal and opposite p_T carried away by some other particle(s). The amount of p_z

transfered to p_T is characterized by x_T:

$$x_T = \frac{2p_T}{\sqrt{s}} \tag{1.16}$$

- Rapidity

  The definition of the rapidity y of a particle is given by:

$$y = \frac{1}{2}\ln\left(\frac{E + p_z}{E - p_z}\right) \tag{1.17}$$

  A nearly identically equivalent quantity, pseudo-rapidity, is related to the polar angle θ, and is more easily measured experimentally:

$$\eta = -\ln\left(\tan\left(\frac{\theta}{2}\right)\right) \tag{1.18}$$

There are certain general correlations between initial and final state variables that exist that are good to be aware of. In particular, there is a correlation between momentum fraction of a parton and the rapidity and p_T of the detected hadron. Though not necessarily true for a particular collision, statistically speaking, the greater the momentum fraction, the more boost the parton and its decays will most likely have. Forward rapidity hadrons (closer to the beam axis) generally come from partons with higher momentum fraction as opposed to central rapidity hadrons (perpendicular to the beam axis), for particles with the same p_T.

The relation between k_T and p_T is even more complex and generalizations cannot be made. Most of the detected particle's p_T comes from the strength of the interaction and momentum transfer x_T and is only slightly modified by k_T.

1.5 Experiments with Protons

1.5.1 Proton Probes

In order to study the proton and its constituents we must probe the proton. There are essentially two kinds of probes used on protons:

1. Lepton scattering off of protons (Fig. 1.6). This type of probe is relatively simple as the intial and final state lepton variables are easier to connect. The problem is that the leptons do not interact strongly, to first order, but only electromagnetically (and weakly). This helps for a cleaner picture of the charge structure of the proton, but does nothing for our understanding of the gluon distribution, except by elimination.

2. Protons scattering off of protons (Fig. 1.7). Here we are able to probe the protons strongly. The difficulty arises from the fact that:

   - The strong interaction can take place between any partonic combination: quark-quark, quark-gluon, or gluon-gluon.
   - We are unable to turn off the electroweak interaction, so we do not get a clean strong picture of the proton. In particular some effects are due to the interference between strong and electromagnetic interactions (see Appendix A).
   - Our probe is itself a fiendishly complicated object instead of being point-like. The extraction of intial state variables becomes more involved and delicate.

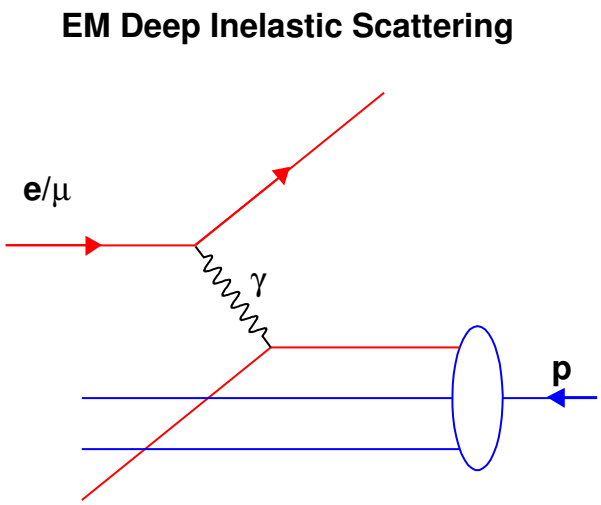

Figure 1.6: Electromagnetic probe. To probe the electromagnetic structure of the proton, leptons are used. In this diagram red denotes a negative charge, blue a positive charge, and black a chargeless particle.

1.5.2 From Structure Functions to PDFs

Using the electromagnetic type of probe described above, many Deep Inelastic Scattering (DIS) experiments measured the nucleon structure during the 1970's and 1980's. By measuring the angular distribution of leptons, the charged structure of the proton was calculated in a manner similar to that used by Rutherford in his famous experiment.

The scattering cross-section of electrons off of quarks is the relativistic version of

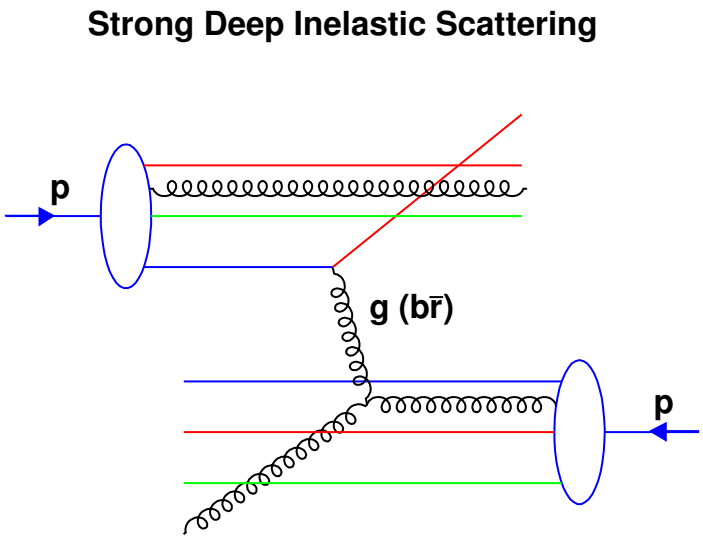

Figure 1.7: Strong probe. To gain access to gluon information, a strong probe (hadron) which is itself composite must be used. The red, blue, and light green colors represent the colors of the quarks. The colors of gluons, represented here by black springs, are not so easily represented visually. In the case of the quark-gluon vertex, the gluon changes the color of the quark from blue to red and so must be $b\bar{r}$. It may only interact with a red quark or a gluon directly.

Rutherford's formula, which is given by:

$$\frac{d\sigma}{dq^2 d\nu} = \frac{\pi\alpha^2}{2k^2 \sin^4\left(\frac{\theta}{2}\right)} \frac{1}{kk'} \left(e_i^2 \cos^2\left(\frac{\theta}{2}\right) + e_i^2 \frac{q^2}{2m_i^2} \sin^2\left(\frac{\theta}{2}\right) \right) \delta\left(\nu - \frac{q^2}{2m_i^2}\right) \quad (1.19)$$

where: q^2 is the momentum transfered, ν is the energy transfered, e_i the fractional charge of the quarks and m_i the mass fraction of the quark given as the fraction of the proton mass M relative to the ratio of the quark momentum to the proton's

momentum:

$$m_i = xM \tag{1.20}$$

The delta function insures conservation of energy. The original Rutherford's formula in $sin^{-4}(\theta/2)$ is modified by two terms, which can be identified as the electric and magnetic components of the interaction. We have:

$$\begin{cases} W_1^i = e_i^2 \frac{q^2}{4M^2x^2} \delta\left(\nu - \frac{q^2}{2m_i^2}\right) \\ W_2^i = e_i^2 \delta\left(\nu - \frac{q^2}{2m_i^2}\right) \end{cases} \tag{1.21}$$

where W_1^i and W_2^i are the magnetic and electric contributions to the interaction due to quark flavor i, respectively. It is important to note that these functions are now x dependent. By summing up over the different flavors and multiplying by the flavor probability distributions, the electric structure function is obtained:

$$\nu W_2 = \sum_i e_i^2 f_i(x) = F_2(x) \tag{1.22}$$

the flavor probability distributions $f_i(x)$ are called Parton Distributions Functions (PDFs). They are given as a function of x and are plotted by fitting data to theory and different models, as with Fragmentations Functions (Section 1.3). They give no indication of spatial distribution. Several groups (CTEQ, MRST) have constructed slightly different versions of PDFs (see Fig. 1.8). By integrating over the x-range, the total partonic contribution to the proton's momentum can be calculated. The main result is that the momentum contribution from quarks (and anti-quarks) is only about 50% of the proton's total momentum [5], although this value varies as a function of the center of mass energy.

By using the strong probe and changing the scattering cross-section in Eq. (1.19) to reflect the strong force, the PDFs for gluons were established confirming that they

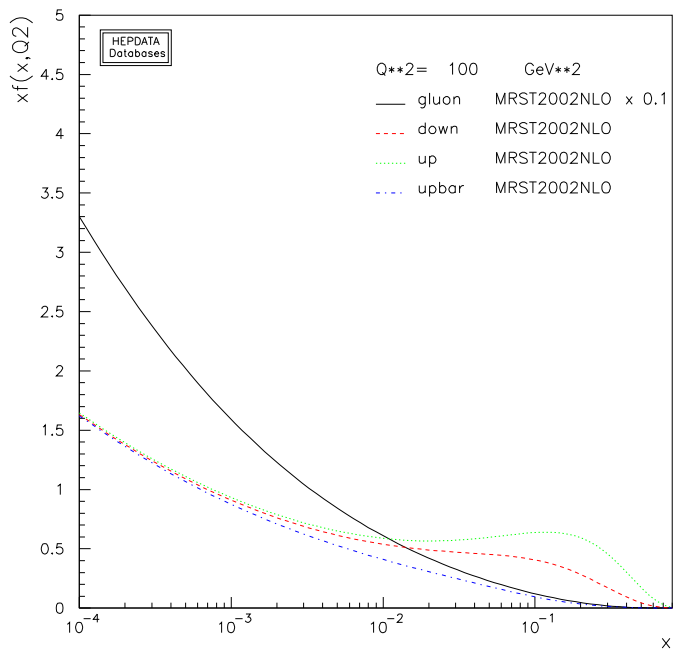

Figure 1.8: Parton Distribution Functions. The different colors are for different flavors of partons: black for gluon, green for up, red for down, blue for anti-up. The y-axis shows the product $xf_q(x)$ and these products are plotted as as a function of x on a log scale.

too carry about 50% of the proton's momentum [5]. In terms of distributions, gluons are more prominent at low x, while quarks are more prominent at higher x.

1.5.3 The EMC Result

In 1988 the European Muon Collaboration (EMC) [6, 7], spurred perhaps by the fact that the sum of the momenta from the different quark flavors only adds up to 50% of the proton's momentum, set out to measure the quarks' spin contribution to the proton's spin. The EMC experiment was an EM probe type of experiment but

with polarized muons scattering off of a polarized target. Eq. (1.19) was modified to include the spin-spin interactions from which $\Delta f_q(x)$ were obtained.

$\Delta f_q(x)$ refers to the difference in probability of finding a spin up quark from a spin down quark in a polarized proton (in the up direction) for a given quark flavor q and a certain momentum fraction x. Fig. 1.9 shows how integrating over all x the difference in the PDFs for up polarized ($f_q^+(x)$) and down polarized quarks ($f_q^-(x)$) gives the contribution of the specific quark to the spin of the proton.

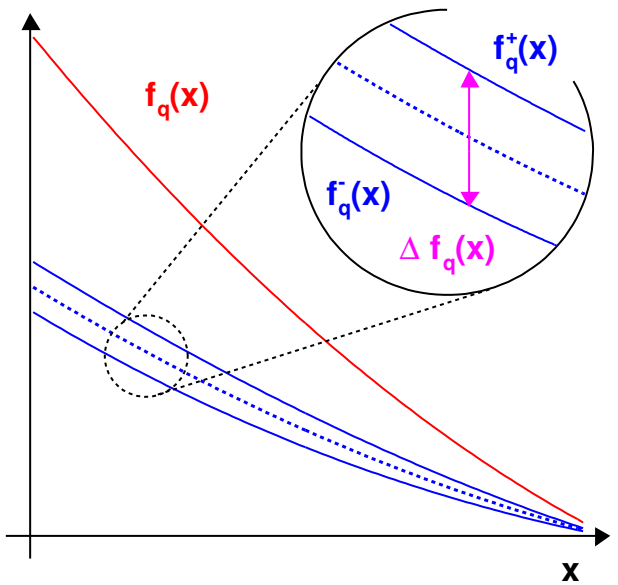

Figure 1.9: Spin-dependent Parton Distribution Functions and the contribution of the spin of a specific quark to the overall proton spin.

The startling result from this experiment was that contrary to the previously held naïve viewpoint that the proton's spin was entirely due to the valence quarks' spin, the total contribution from all quarks, both valence and sea, was only on the order of 27% of the total.

This "spin crisis" as it has been labeled has been at the center of many spin programs and experiments.

The angular momentum sum rule, Eq. (1.23), nonetheless tells us that the proton's spin is a simple sum of the quarks' spin, the gluons' spin and the orbital angular momenta of the quarks and gluons.

$$J_z = \frac{1}{2} = \frac{1}{2}\Delta\Sigma + L_q + \Delta G + L_g \tag{1.23}$$

Here $\frac{1}{2}$ is the total spin of the proton, $\Delta\Sigma$ is the quarks' spin contribution (both valence and sea, u, d and s flavors), ΔG is the gluons' spin contribution, while the L_q and L_g are the orbital angular momenta of the quarks and gluons, respectively.

Recent measurements of the quark spin ($\Delta\Sigma$) [8, 9, 10, 11, 12, 13, 14] contributions have confirmed the initial EMC results and shown them to be insufficient to account for the proton's spin. In addition, measurement of the strange quark contribution Δs has been measured to be small and negative. By assuming that all light flavors (u, d and s) are created equally from the vacuum, the result shows a small negative contribution from the sea quarks, and, by subtracting this result from the 27% total contribution measured by the EMC colaboration; a larger, though insufficient positive contribution from the valence quarks.

These Deep Inelastic Scattering (DIS) experiments can also make an indirect measurement of the gluon spin contribution [15], although with very limited precision. COMPASS and SMC [16] have recently shown results for ΔG from muon-nucleon interactions. Statistically limited, PHENIX measurements of the gluon spin (ΔG)[17] are still more restrictive and seem to indicate a small contribution to the proton's spin due to gluon spin, while at the same time the possibility that the gluon spin accounts for all the missing proton's spin is still within the upper limit of the error bars and so cannot be excluded. The COMPASS experiment at CERN has recently

publicized their measurements for ΔG which are consistent with the PHENIX measurements within all uncertainties. The current status of the spin-dependent Parton Distribution Functions has recently been summarized for convenient reference [18]. Appendix B contains a more in depth look at the measurement of ΔG in general, as well as a specific example of A_{LL} measurement from open charm decay.

Currently almost nothing is known about the quark and gluon orbital angular momenta, although asymmetries have been measured that are thought to stem from orbital angular momentum (see Section 2.4) and many groups are designing and implementing new experiments to measure L_q and/or L_g.

1.6 Dissertation Structure

This is a study of the angular correlations in jet-jet events resulting from longitudinally polarized p+p collisions in order to measure the partonic orbital angular momentum (POAM) contribution (L_q, L_g) to the proton's spin. The study will separate events according to helicity states in order to examine the possibility of a spin-related contribution to k_T, which would correlate directly to POAM, using a technique similar to a technique previously suggested by M. Ta-Chung et al. [19] in the Drell-Yan channel. The layout of the dissertation is as follows:

- Motivating the dissertation (Chapter 2). A review of theoretical studies and experimental results concerning partonic orbital angular momentum and intrinsic transverse momentum k_T.
- A brief overview of the experimental setup (Chapter 3), including the RHIC ring and the PHENIX detector, as well as polarimetry.
- Methodology (Chapter 4). The mechanics of jet-jet correlation studies are discussed.

- Analysis. (Chapter 5). The cuts and techniques used in the present analysis, including a look at the π^0 analysis.

- Analysis results (Chapter 6) from spin-sorted jet-jet angular correlations in PHENIX run3pp.

- A simple PYTHIA Monte Carlo model (Chapter 7) of orbital angular momentum in the proton in order to determine the sensitivity of our method to the existence of POAM.

- A brief conclusion (Chapter 8). What have we learned? What are the future plans for measuring orbital angular momentum? How might we improve our measurements through greater statistics and better technique?

- A more in depth look at polarimetry (Appendix A) in the AGS and RHIC and a proposal for an extracted beam CNI polarimeter in the AGS.

- An analysis (Appendix B) that attempts to calculate ΔG from run3 data using semi-leptonic decay coincidence events from open charm production through the gluon-gluon channel.

- We revisit the calculation of the π^0 A_{LL} measurement (Appendix C) for extraction of ΔG to gain insight into how spin and orbital angular momentum contributions can mutually influence each other's measurements.

Chapter 2

Motivation

2.1 Introduction

The idea that there might be partonic orbital angular momentum (POAM) is not new and there are four essential motivations:

1. According to S. Brodsky [20], the Dirac equation already shows that the ground state of the proton holds s-wave ($l = 0$) and p-wave ($l = 1$) components. Although this is not transparent in the standard form of the equation, it becomes evident when written in the Light Front (LF) formalism where a $l = 1$ Fock State appears.

2. Although the addition of Confinement to the naïve quark model invalidates the calculation of the magnetic moment due simply to quark spin, it also requires some partonic angular momentum to obtain the proton's magnetic moment. The minimal constraint and one partially favored by theorists is that there would be little or no net POAM but that positively charged quarks (u and $\bar{d}$) would rotate in one direction, and negatively charged quarks would rotate

in the other. This could still mean that $\sum_q L_q = 0$ but it does require some orbital motion.

3. The detected presence of k_T.

4. Single Spin Asymmetries (SSAs).

These last two items require a more in depth description and are discussed further in Section 2.2 and Section 2.4.

2.2 Measured Existence of k_T

The existence of orbital angular momentum would be compatible with another minor mystery in experimental physics. When colliding particles at high energies, some longitudinal momentum is converted into p_T. The p_T distribution in particle production from this conversion has been calculated to be a power law at high-p_T. The experimental results measured at CERN-ISR [21] in 1972 for π^0 production show that this power law is not respected. The reason for the deviation from the power law is k_T smearing, a modification of the π^0 p_T due to k_T that was not initially understood. In this context k_T is not necessarily intrinsic partonic transverse momentum, but some net parton transverse momentum that could have as its origin a number of causes. In this section alone we will use k_T in its broader sense and use the nomenclature "intrinsic k_T" for the more specific kind.

The amount of k_T has been measured [22, 23, 24] to be in the 2-3 GeV range for center of mass energies of the same order of magnitude as those used used in our analysis.

Fig. 2.1 illustrates the idea of k_T. In the first panel two protons collide with no k_T, yet the two jets are not back-to-back in the lab frame. This is because the

momentum fractions x_1 and x_2 of the partons are not à priori equal. However, the acoplanarity exists only in the longitudinal direction. In the transverse plane the jets are back-to-back in the lab frame. In the second panel the partons also carry k_T and are no longer back-to-back in the transverse plane. Note that we are never implying that there is net transverse momentum. Momentum conservation always applies, of course. If there is net k_T, this means an equal and opposite amount of transverse momentum is carried away by the remaining partons in the proton, also called the beam remnant.

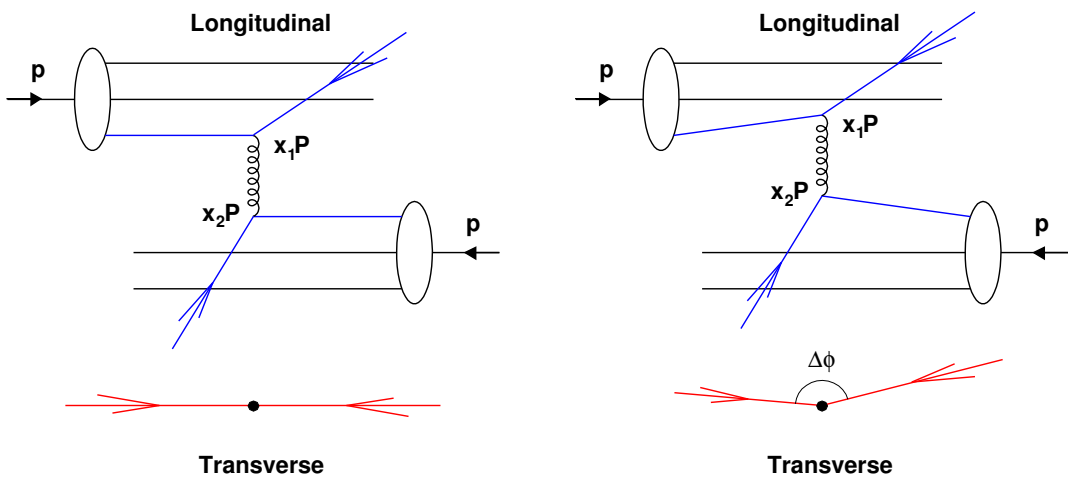

Figure 2.1: Feynman Diagram of colliding protons in the longitudinal and transverse planes. *(left)* Two protons collide with no k_T, yet the two jets are not back-to-back in the lab frame. This is because the momentum fractions x_1 and x_2 of the partons are not à priori equal. However, the acoplanarity exists only in the longitudinal direction. In the transverse plane the jets are back-to-back in the lab frame. *(right)* The partons also carry k_T and are no longer back-to-back in the transverse plane.

Several possibilities suggest themselves as the source of this k_T:

1. Heisenberg's Uncertainty principle. The parton wave functions are confined to

a region of space, namely the proton, which means that according to:

$$\Delta x \cdot \Delta p_x \geq \frac{\hbar}{2} \tag{2.1}$$

the partons must have a random k_T. However, the amount calculated due to this Heisenberg Uncertainty effect is on the order of 200-300 MeV , an order of magnitude smaller than the observed k_T.

2. Soft gluon radiation. Initial or final state radiating gluons akin to Bremsstrahlung carry momentum from the parton and give it an equal and opposite transverse momentum kick.

3. NLO radiative corrections in hard scattering processes. This possibility is illustrated in Fig. 2.2. In the upper panel two protons collide and a $c\bar{c}$ quark pair is produced from gluon fusion. In the absence of other sources of transverse momentum, the gluon pair has no net transverse momentum, as a result neither does the $c\bar{c}$ pair nor the resulting J/ψ. In the second panel a next-to leading order (NLO) process is considered in which a gluon carries momentum away from the $c\bar{c}$ pair. The net transverse momentum of the pair, and that of the resulting J/ψ is now equal and opposite to that of the gluon. The value of the J/ψ transverse momentum has been measured [25] to be:

$$\langle p_T \rangle_{J/\psi} = (1.8 \pm 0.23 \pm 0.16)\text{GeV}/c \tag{2.2}$$

Note that this measurement did not measure J/ψ and jets, merely J/ψs. To better measure the described effect, *i.e.* a gluon creating J/ψ k_T by carrying away transverse momentum, a comparison between J/ψ with and J/ψ without an accompanying jet should be made.

4. POAM. The basis of our analysis is that we consider the possibility that some of the k_T may be spin-correlated, *i.e.* due to orbital angular momentum of the partons in the proton.

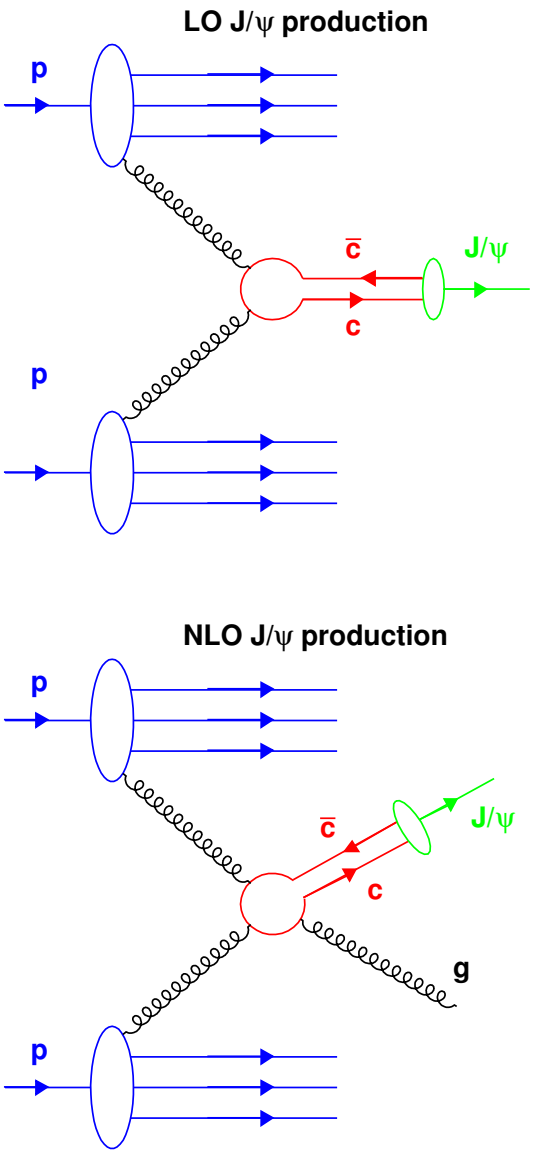

Figure 2.2: J/ψ transverse momentum from NLO diagrams. *(top)* The gluon pair has no net transverse momentum, as a result neither does the $c\bar{c}$ pair nor the resulting J/ψ. *(bottom)* A gluon carries momentum away from the $c\bar{c}$ pair. The net transverse momentum of the pair, and that of the resulting J/ψ is now equal and opposite to that of the gluon.

2.3 Measurement of POAM

In the late 1990's, Ji [26] proposed an experimental tool to measure the quark orbital angular momentum, and since that time, experiments at DESY and Jefferson Lab have pursued this course [27]. The method uses deeply virtual Compton scattering (DVCS); *i.e.* a virtual photon emitted by a lepton probe, absorbed by a quark, which is excited and which in turn emits a real photon. The detection of the real photon offers insight into off-forward parton distributions (OFPDs) a new kind of PDF akin to the generalized parton distributions (GPDs) described in Section 2.5, which in turn could lead to information on quark orbital angular momentum.

The basic picture for our analysis, developed by D.E. Fields [28], is that if the k_T of partons is correlated to the (longitudinal) spin direction, as it would be in the case of orbital angular momentum, then hard collisions involving these rotating partons may lead to jets with more (or less) average transverse momentum depending upon the relative orientation of the spin directions and the centrality of the collision (see Fig. 2.3). Since, at present, there is no good experimental tool to determine the collision centrality in p+p collisions, one must determine if a net $\sqrt{\langle k_T^2 \rangle}$ difference between parallel and anti-parallel helicity events remains even when the impact parameter is undetermined. Note that in our analysis, since we are colliding longitudinally polarized protons, we can only measure $\sqrt{\langle k_T^2 \rangle}$ and not $\vec{k}_T$, as we have no way of determining the relative orientations of the protons and distinguishing rotation direction.

In a previous work [19], with a rather simple picture of the transverse spatial and momentum distributions, it was found that by integrating over the entire range of impact parameter, a net overall difference is still found. We also present in Chapter 7 a simple Monte Carlo to model this effect and to then determine if our method of measuring the average k_T is sufficiently sensitive to detect such an effect.

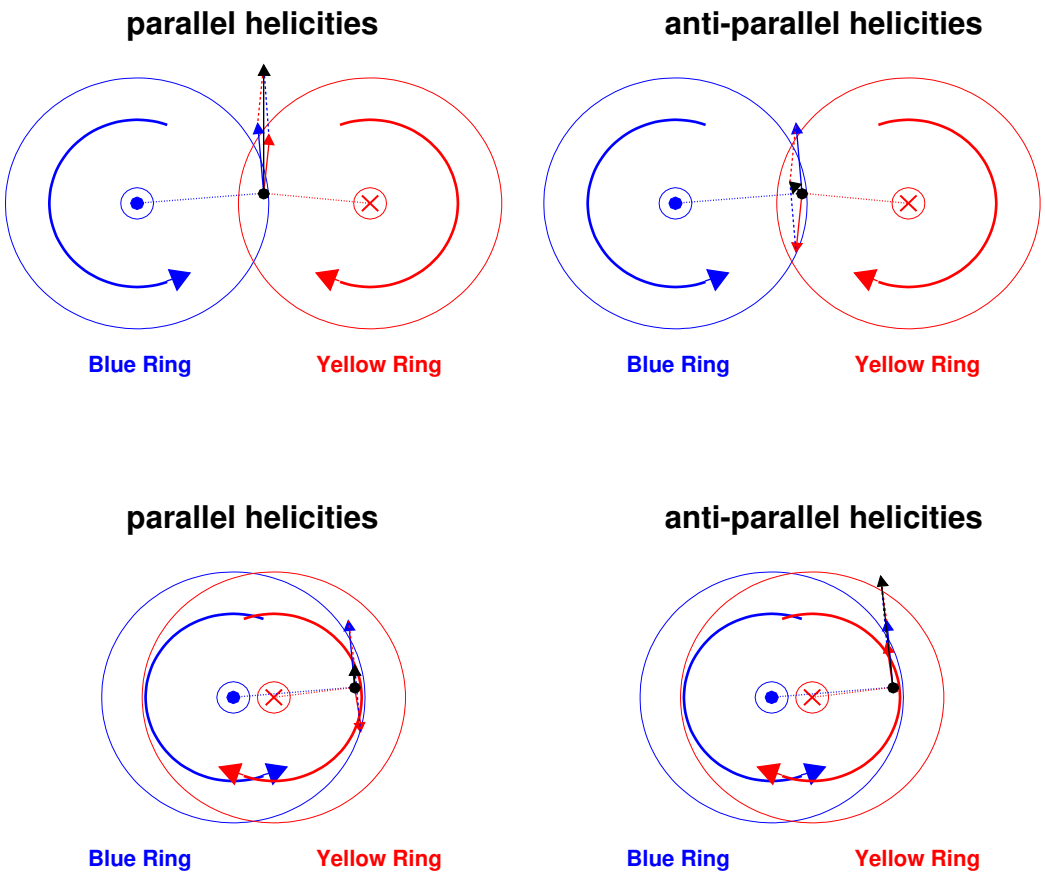

Figure 2.3: Comparing different impact parameter collisions of longitudinally polarized protons. For parallel helicities the k_T of the rotating partons (blue and red arrows) add for peripheral collisions and give a large net $\vec{k}_{T\text{pair}}$ (black arrow) to the created jet pair. For central collisions in the same helicity combination, the k_T from POAM of the partons cancel to a great degree, leaving the center of mass system with little $\vec{k}_{T\text{pair}}$. For anti-parallel helicities the opposite effect is seen, *i.e.* peripheral collisions give a small $\vec{k}_{T\text{pair}}$ due to POAM, while central collisions give a larger $\vec{k}_{T\text{pair}}$.

2.4 Single Spin Asymmetries

Collisions involving transversely polarized protons have been shown to have Single Spin Asymmetries (SSAs), meaning an imbalance between scattering to the left or right [29, 30]. By summing over both polarizations in one beam, data is obtained for an unpolarized beam colliding with transversely polarized protons. The results show left-right asymmetries (Fig. 2.4) in particle production which have been at the center of much interpretative debate, including the possibility of attributing such asymmetries to partonic orbital angular momentum.

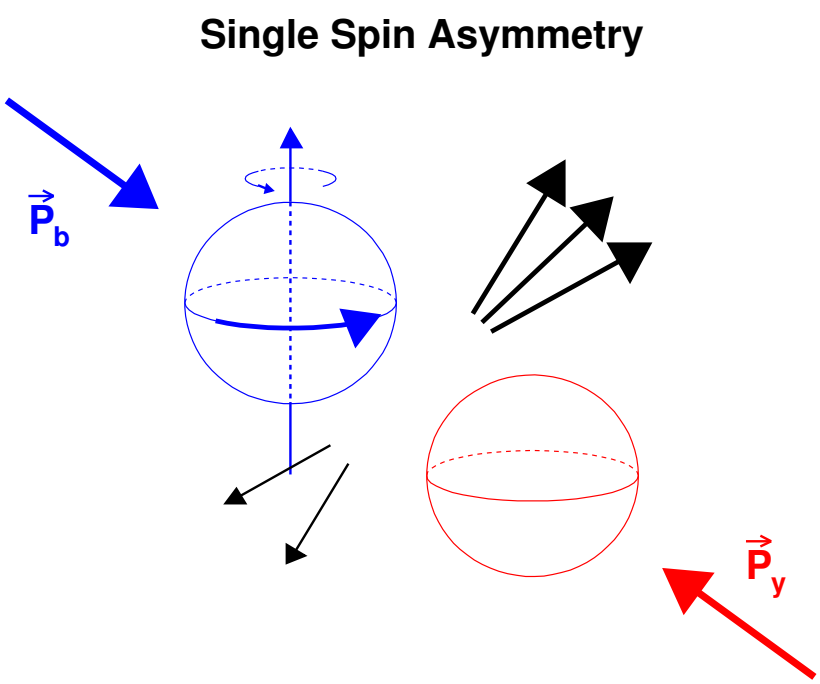

Figure 2.4: Single Spin Transverse Asymmetry. A left-right asymmetry in particle production is observed between colliding protons, one proton is unpolarized (red) and the other (blue) is transversely polarized.

2.4.1 Sivers Effect

The first suggestion and one of the most popular explanations for SSAs is the Sivers Effect [31, 32], first suggested by D. Sivers to explain large SSAs at FNAL [30] and RHIC [33]. The naïve inerpretation of the Sivers effect is shown in Fig. 2.5. A solid object colliding with another solid object has more chance of being deflected to the right than the left. At first glance this simple model is not accurate, even to explain the Sivers effect. Protons are not solid objects and a partonic collision is as likely to occur on the far side of the "rotating" proton and give a k_T boost in the left direction. However, according to D. Sivers [34] an effect is nevertheless expected, and this model does actually give a reasonable interpretation of that effect. There is a final state interaction due to the absorber (non-rotating) component of the proton, which modifies the wave function of the proton depending on which particular process is involved, "hiding" a part of the proton to a certain extent (in this case the back). The key here is process dependence. Asymmetries will be measured but will depend on the type of process encountered. In particular, an opposite asymmetry to the one measured at E704 would be measured for Drell-Yan production which has no final state interaction, as opposed to the hard scattering processes where final state interactions but no initial state interactions occur.

A lengthier discussion of the Drell-Yan Sivers Effect is given in Section 8.2.2.

The Sivers Effect requires POAM; however, measuring SSAs does not necessarily imply the existence of the Sivers Effect. Other explanations for SSAs include the Collins Effect, discussed next.

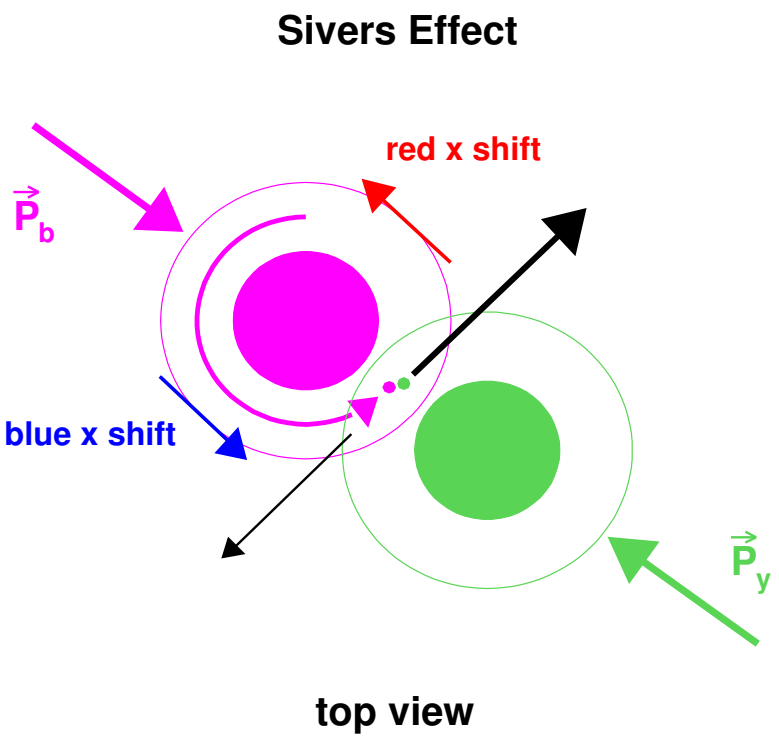

Figure 2.5: The Sivers Effect. A left-right asymmetry is expected because of spin-oriented k_T, orbital angular momentum, in processes with no initial state interaction. POAM also would create Doppler shifts in the momentum fraction of the colliding partons.

2.4.2 Collins Effect

Another possible explanation for SSAs is the Collins effect [35]. This effect says that the Fragmentation Functions depend on the spin of the partons (see Fig. 2.6), and if there is partonic spin contribution to the proton's spin, which there is (even though it does not account for all the proton spin) then an asymmetry will arise.

As previously mentioned, a Fragmentation Function (FF) is a description of the way a parton fragments into hadrons. During fragmentation a finite amount of trans-

verse momentum is imparted to the hadron, called j_T. In the absence of pre-existing conditions, on average, the angular deviation of the hadrons with respect to the original partonic momentum direction is symmetric around zero. In a spin-oriented proton, however, the partons, and in particular the valence quarks have a higher probability of having a definite spin orientation, and the resulting Fragmentation Functions are affected accordingly.

The Collins effect is believed to be important only for quark-quark interactions which occur with greater frequency at higher p_T, and in particular for valence quark interactions which generally carry a higher momentum fraction and therefore generally have decay products in high rapidity regions. Nevertheless it will be important to distinguish j_T, or fragmentation, effects from k_T effects in any experimental measurements.

2.4.3 Twist-3 Effects

Another explanation for the SSAs suggests a contribution from a higher order (Twist-3) Feynman Diagram. According to calculations by F. Yuan and W. Vogelsang [36] these contributions may exist, but would only contribute at much higher $p_T (p_T > 10\text{GeV}/c)$; the more likely effect at lower p_T being the Sivers Effect.

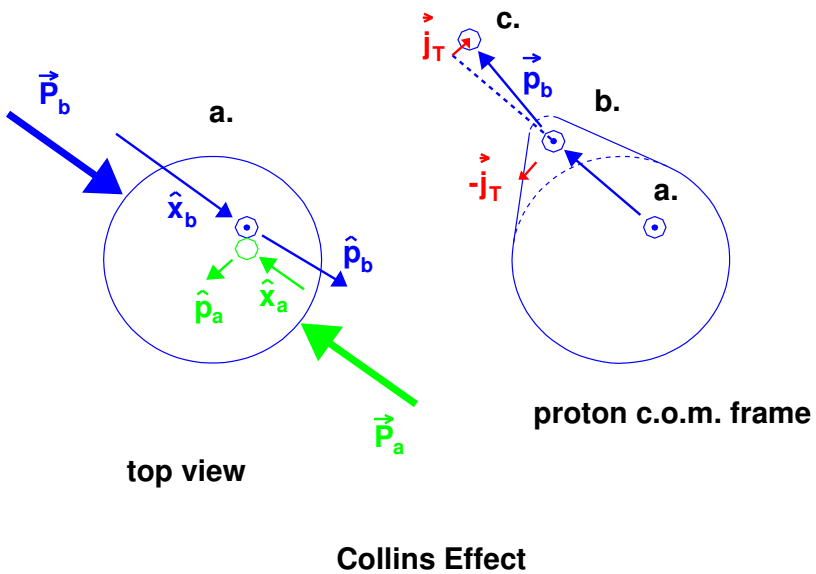

Figure 2.6: The Collins Effect. This schematic diagram shows the collision of two partons, one green, one blue transversely polarized; then follows the evolution of the blue scattered parton through hadronization in the blue polarized proton center of mass frame. For clarity, the partons are no longer point-like, and the momentum vectors do not extend into the drawn partons. *(left)* the partons collide ($\hat{x}_i$ represents $x_i\vec{P}_i$), the dotted parton represents a spin-up parton. *(right)* in the proton's center of mass frame, the polarized parton collides at *a*. At *b*. the scattered polarized proton still has mostly forward momentum but has less velocity than the rest of the moving proton. It reaches the limit of confinement and hadronizes to *c*. During hadronization, because of its spin, the parton will aquire j_T that is more likely to be oriented and will impart an equal and opposite transverse momentum to the proton remnant.

2.5 Generalized PDFs

Parton Distribution Functions (PDFs), described in Section 1.5.2, characterize the distributions of partons within the proton. Note that even though only up and down quarks exist as valence quarks in the proton, any flavor - anti-flavor $q\bar{q}$ pair may exist within the proton as sea quarks. PDFs are given as a function of x, the momentum fraction, Eq. (1.13). More recently, in order to better understand the inner workings of the proton, attempts have been made to expand the PDFs to include variables such as: b (the impact parameter), k_T, and the transfer of longitudinal and transverse momenta. These are called Generalized Parton Distributions (GPDs) and Transverse Momentum Dependant parton distributions (TMDs).

Another attempt to generalize PDFs, the Off-Forward Parton Distributions (OFPDs) [37, 38] has been mentionned in Section 2.3.

It is clear that the results from SSA studies are part of the same general study as this analysis and others which seek to extract POAM from the collisions of polarized protons, and all results will need to fit a single set of distribution functions, be they GPDs or other, as well as a unified result for orbital angular momentum. It seems that we are not there yet, and more results will need to follow before we can obtain a clear picture of the proton's structure and spin.

Further complicating matters is the emerging awareness of the interdependence of all such measurements. Appendix C is one such example, as is the illustration in Fig. 2.5 of the way the momentum fraction x is modified by Doppler-shifting due to POAM. This can only make extraction of individual components of the proton spin puzzle more difficult.

2.6 The 2-Dimensional k_T View

As opposed to the case for longitudinally polarized protons, it is possible to measure the direction of k_T in transversely polarized protons, and the results from E704 [30] seem to indicate a net measured $\vec{k}_T$ for positive charges $(u, \bar{d}, \bar{s})$ and an opposite net measured $\vec{k}_T$ for negative charges $(d, s, \bar{u})$. The calculated values are nearly equal and could meet the minimum angular momentum requirement for magnetic moment, *i.e.* no net angular momentum. As previously seen, GPDs are a function of k_T, the magnitude of $\vec{k}_T$, and much theoretical and experimental data is presented in terms of k_T. The problem is that it is not very consistent with reality. While it is certainly possible for there to be net $\sqrt{\langle k_T^2 \rangle}$, it is theoretically impossible for there to be any net $\vec{k}_T$ or any net charge $\vec{k}_T$, or any net flavor $\vec{k}_T$, indeed any kind of net $\vec{k}_T$, otherwise that charge or flavor or parton would migrate out of the proton. Therefore the measured $\vec{k}_T$ cannot be the whole picture. This is illustrated in Fig. 2.7 (a). Two points can be made concerning these results, as mentioned by D. Sivers [34] and M. Anselmino [39], respectively.

1. The measured k_T must be process dependant and is measured only because part of the proton is shielded by the particular type of interaction and process at work.

2. $\vec{k}_T^+ + \vec{k}_T^- = 0$ does not necessarily imply $\vec{L}_+ + \vec{L}_- = 0$, because $\vec{k}_T$ does not give us information on the radial distribution.

In fact these measurements make sense in the context of the Sivers Effect which results from an effective screening of the "back" half of the proton. This is illustrated in Fig. 2.7 (c).

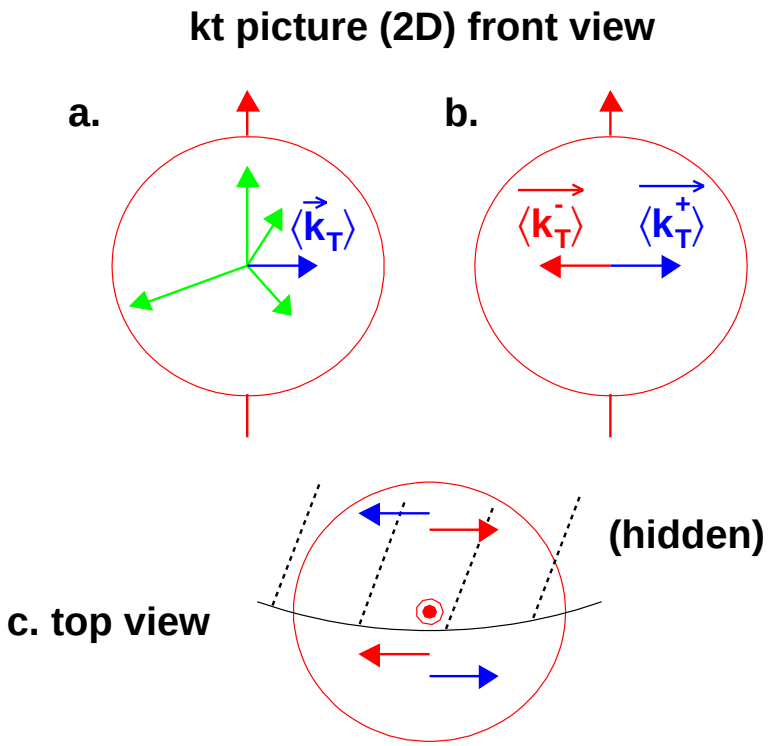

Figure 2.7: The 2-dimensional view of $\vec{k}_T$. Figure (a) shows random $\vec{k}_T$ and an overall global $\vec{k}_T$. Figure (b) shows net $\vec{k}_T$ of negative charge in one direction and net positive $\vec{k}_T$ in the other. The two are equal and opposite. Figure (c) illustrates the "hidden" $\vec{k}_T$ and the fact that no net $\vec{k}_T$ does not necessarily imply no net POAM.

2.7 Predicting POAM

The reluctance to discuss POAM comes from the difficulty of calculating analyzing powers or any asymmetries from cross-sections in pQCD taking k_T into account. The fundamental principle that allows calculations for the cross-sections, is colinear factorization. The cross-section for $p + p \rightarrow X$ is proportionnal to:

$$< \psi_{final} | M_{ij} | \psi_{initial} >^2 \tag{2.3}$$

where the matrix element M_{ij} is equal to the product of the PDFs, the cross-section for particular contributing partonic processes, and the Fragmentation Functions(FFs):

$$M_{ij} = f_q(x) \cdot \hat{\sigma}_{ab \to cY} \cdot D_X^c(z) \tag{2.4}$$

This is possible because for a colinear collision the three factors are independant of each other. Introducing k_T breaks that colinearity, introduces dependencies, and renders calculations extremely difficult.

In an attempt to provide a different explanation for a possible a azimuthal angle asymmetry from longitudinally polarized protons, as our analysis sets out to measure, W. Vogelsang postulated [40] a width difference for quarks and gluons from spin down to the spin up configuration, which resulted in such an effect. The magnitude of such an effect is small, however, $\approx 10\text{MeV}$ and highly unlikely to affect our measurement.

The point of this calculation was to show that a difference in k_T between parallel and anti-parallel helicity events in longitudinally polarized p+p would be due to POAM to first order, and that other possible sources of asymmetry would be relatively minor.

Chapter 3

Experimental Facility

In order to effectuate polarized p+p collisions, a technical difficulty must be overcome: namely, the acceleration of polarized protons. The Relativistic Heavy Ion Collider (RHIC) was built with such an operation in mind. A look at the experimental facility where we propose to measure POAM is then warranted. We will take a brief look at:

1. the RHIC facility.
2. How polarization is maintained and measured at RHIC.
3. the PHENIX detector, where the data is taken.

3.1 RHIC

The Relativistic Heavy Ion Collider (RHIC) located at Brookhaven National Laboratory (BNL) on Long Island, New York, is a versatile machine capable of accelerating a wide range of ions to an energy of 200 GeV per nucleon as well as protons up to

an energy of 250 GeV . For the 2003 polarized proton run (Run3pp), the energy per proton was 100 GeV , resulting in a center of mass energy of $\sqrt{s} = 200$ GeV . RHIC is a 2.6 mile circumference ring of two separate beam pipes, labeled as blue and yellow, each carrying heavy ions or protons, that can intersect at six different locations on the ring. Each intersection point is potentially the location of experimental apparatus. For Run3pp, only four were in use:

- STAR: located at six o'clock on the ring seen from the air, where twelve o'clock is the northern direction.
- PHOBOS: located at the ten o'clock position.
- BRAHMS and pp2pp share use at the two o'clock position
- PHENIX: at the eight o'clock intersection point.

RHIC is actually only the last and largest accelerator in the chain that exists at BNL. Both of its beam pipes, yellow (clockwise) and blue (anti-clockwise) are fed by the Alternating Gradient Synchrotron (AGS), another accelerator ring, via the AGS to RHIC (ATR) line. The AGS itself receives the ions from the Booster ring, which in turn obtains either protons from the linear accelerator (LINAC) or heavy ions from the tandem van de Graaf accelerator (Fig. 3.1).

The protons are ionized Hydrogen atoms accelerated from the optically pumped polarized ion source (OPPIS)[41, 42]. This polarized H^- source produces 500 μA in a single 300 μs pulse, which corresponds to $9 \cdot 10^{11}$ polarized H^-. This is sufficient intensity to eliminate the need for accumulation in the Booster. The polarized H^- ions are accelerated to 200 MeV with the LINAC with an efficiency of about 50%. The pulse of H^- ions is strip-injected and captured into a single bunch in the AGS Booster. The bunch in the Booster will then contain about $N_B = 4 \cdot 10^{11}$ polarized protons with a normalized emittance of about $\epsilon_N = 10\pi$ mm-mrad. The single bunch

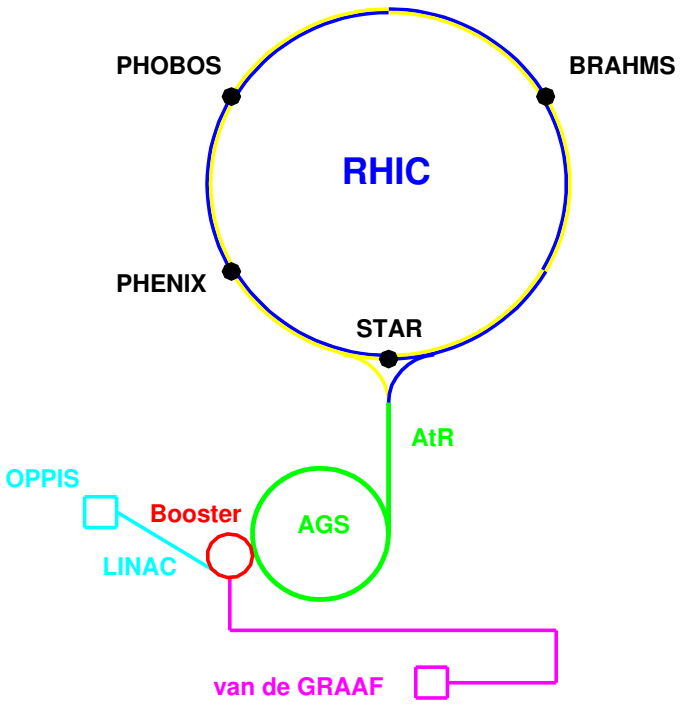

Figure 3.1: Location of experiments at RHIC

of polarized protons is accelerated in the Booster to 1.5 GeV and then transferred to the AGS, where it is accelerated to 24 GeV. From 6 to 110 bunches are injected into the RHIC, where the protons are again accelerated, this time to 100 GeV, and where each bunch can hold up to 10^9 ions, thetime between crossings for 56 bunches (the maximum used for Run3pp) being 212 ns.

The fundamental improvement in this set-up over previous accelerator facilities has been the ability to polarize, and more importantly, to maintain the polarization of the protons through the various accelerations. Without this ability there would be no spin physics program, and proton collisions at RHIC would merely serve as a baseline for heavy ion experiments. As such, a brief description of the technology

and hardware relative to polarization is merited.

3.2 Polarized Proton Acceleration and Mesurement

3.2.1 Polarized Proton Acceleration

To achieve high energy polarized proton collisions, polarized beams first have to be accelerated, which requires an understanding of the evolution of spin during acceleration and the tools to control it. Maintaining polarization during acceleration in the different rings is done with the aid of devices known as Siberian Snakes [43]. The depolarization occurs to first order because of Thomas precession and the non-homogeneity of the various magnetic fields which causes slightly different precession rates. The Snakes which are local 180° spin rotators compensate for the precessional differences.

Each Siberian Snake consists of a set of four superconducting helical dipole magnets. The magnets are capable of producing a central field of up to 4 T which spirals through 360° over a length of approximately 2.4 m. Four such magnets, each independently powered, can generate a spin rotation from vertically up (the nominal stable spin direction for the synchrotron) to vertically down, with no net excursions of the particle trajectory. By doing so every rotation, the Thomas precession from the vertically down cycle around the ring compensates the precession from a ring cycle with spin up and in so doing maintains polarization of the beam.

Technical difficulties also arise during transfer from one ring to the next, particularly when in the AtR because the plane of the AGS is not the same as the RHIC plane, so the beams must be bent and rotated to descend the slope to RHIC along

the ATR, then bent and rotated back to the horizontal plane once in RHIC.

Once in RHIC, Spin Rotators are located at the entrance and exit of each experiment. They are used when longitudinally colliding protons are desired. The Spin Rotator is similarly constructed to the Siberian Snake; by altering the "handedness" of two of the helical magnets, and using slightly different fields, the spin can be made to rotate from the vertical to the longitudinal direction through the intersection, then rotated back to the vertically polarized position when exiting the intersection region (IR).

3.2.2 Polarimetry

In order to maintain good polarization, a system of measuring polarization, known as polarimetry must be in place. Polarization is measured at each step, before the Booster, in the AGS, and in RHIC. A more in depth study of polarimetry in the AGS and RHIC for Run3pp as well as a proposal for the measure of polarization in the AGS and RHIC is discussed in Appendix A.

The essence of polarimetry is to set up fixed target experiments to sample the beam in the different rings and to measure an asymmetry (A_x) which is then compared to a known physics asymmetry, called the Analyzing Power (a_x). The asymmetry can be of several types, the most common being:

- A directional (left-right) asymmetry as mentionned in Section 2.4.
- A cross-sectional, or number, asymmetry between different helicity configurations like those used in Appendix A and Appendix B.

The comparison of Analyzing Power to measured asymmetry gives the polariza-

tion P:

$$A_x = P \cdot a_x \tag{3.1}$$

The polarization in the AGS is measured by means of a p+C Coulomb-Nuclear Interference (CNI) polarimeter. This means that the asymmetry comes from an interference term in the electromagnetic and nuclear forces. The x in Eq. (3.1) refers to the process, which in this case is p+C elastic scattering.

The polarized proton beams are delivered to the various experiments, including PHENIX, the experiment of interest. Polarization is measured locally at PHENIX and is checked versus the polarization measured at twelve o'clock in the RHIC ring. It is interesting to note that the local polarimeter in PHENIX uses an analyzing power that was previously unknown: a forward neutron asymmetry. By measuring the neutrons produced in transversely polarized p+p collisions, an asymmetry was observed, and by mapping that asymmetry, a range of Analyzing Power was obtained to use for local polarimetry. For Run3pp, since we are colliding longitudinally polarized protons, the local polarimeter analysis serves to check that the polarized beam has been properly rotated. We next take a closer look at the entire PHENIX detector including local polarimetry.

3.3 The PHENIX Detector

3.3.1 Overview of PHENIX

The PHENIX experiment [44] is one of the two (with STAR) large experiments at RHIC. It is an experiment with over 500 collaborators from 26 different countries. PHENIX is a heterogeneous experiment, put together by several different groups

having different physics motivations. As such it has a large number of sub-detectors, which can be divided into three main categories, consisting of four spectrometer arms - two around mid-rapidity (the central arms) and two at forward rapidity (the muon arms) - and a set of global detectors:

The layout of the PHENIX experiment during Run3pp is shown in Fig. 3.2.

3.3.2 Global Detectors

The global detectors are concerned with vertex resolution, minimum bias triggering and polarimetry. Three global detectors are employed [45]. They consist of:

- Zero-Degree Calorimeters (ZDC)
- Beam-Beam Counters (BBC)
- Normalization Trigger Counter (NTC)

As indicated by their name, ZDCs are located at zero degrees along the beam axis behind the intersection where the outgoing beam is diverted into the particular yellow or blue beampipe. The ZDCs are calorimeters which detect neutral particles (essentially neutrons and photons, because all forward charged particles are swept away by the bending magnets). While extremely useful for Au+Au collisions which have many spectator neutrons for purposes of determining centrality, the ZDCs provide little useful information for p+p collisions. The ZDCs have been outfitted with a shower max detector (SMD) for measuring transverse polarization (see Section 3.3.5).

A pair of BBCs detect passing charged particles which provides level 1 triggering of vertex collisions and is essential in determining the vertex position along the beam axis. The technology employed for this role is a one-inch mesh dynode photomultiplier tube mounted on a 3 cm quartz radiator. An array of 64 such channels

are located on either side of the collision point along the beam axis. They cover the full azimuth at a pseudorapidity range of 3.0 to 3.9 in both directions. The vertex position is determined by the timing difference of signals for the north and south beam-beam counters with a resolution of 50 ps. This corresponds to a vertex resolution along the beam axis of about 2 cm.

The NTC extends the coverage of the BBC for p+p and d+Au running, assisting the BBC primarily in the level 1 triggering.

3.3.3 Central Arms

The central arm detectors [46] are located in two arms: East and West in the mid-rapidity range, and are concerned primarily with electron, photon and hadron detection. Each central arm covers the pseudorapidity range $|\eta| < 0.35$ and 90 ° in azimuthal angle. The azimuthal distance between the arms is $\pi/4$ on the top, but $3\pi/4$ on the bottom. The magnetic field [47] for the central spectrometer is axially symmetric around the beam axis. Its component parallel to the beam axis has an approximately Gaussian dependence on the radial distance from the beam axis, dropping from 0.48 T at the center to 0.096 T (0.048 T) at the inner (outer) radius of the DC. The detectors used in Run3pp are:

- The electromagnetic calorimeter (EMCal) which is the outermost subsystem on the central arms and provides measurements of both photons and energetic electrons. A lead-scintillator (PbSc) calorimeter is used for good timing and a lead-glass (PbGl) calorimeter gives good energy resolution. They are located in mutually exclusive $\phi - \theta$ coverage. Most analyses use information from both types.

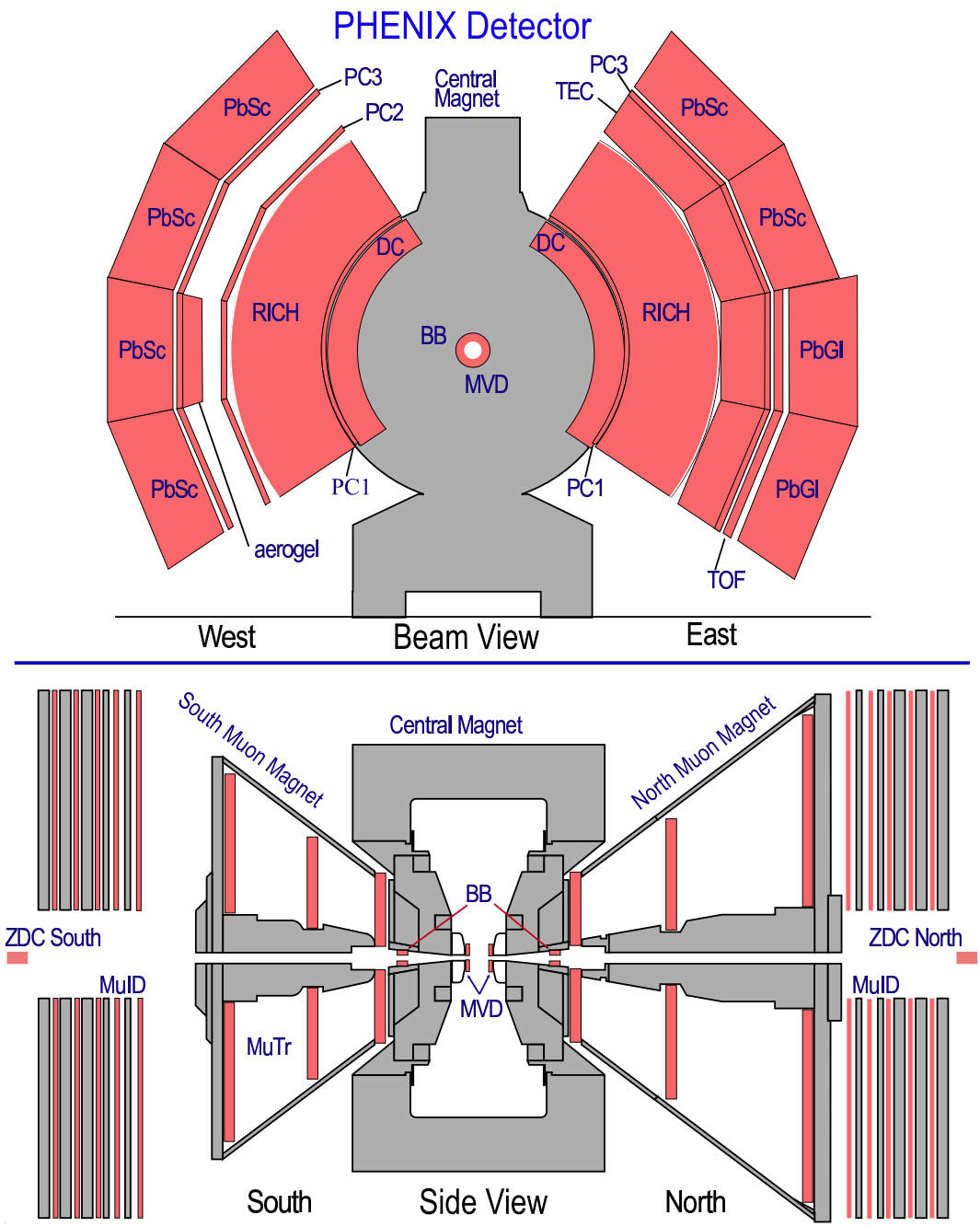

Figure 3.2: The PHENIX experimental layout for Run3pp. The top panel shows the PHENIX central arm spectrometers viewed along the beam axis. The bottom panel shows a side view of the PHENIX muon arm spectrometers and the position of the global detectors (BBC and ZDC).

- The tracking system uses two or three sets of Pad Chambers (PC), depending on the arm, to provide precise three-dimensional space points needed for pattern recognization (PC1, PC2, PC3 located at 2.4m, 4.2m, 5m in radial direction, respectively).
- The precise projective tracking of the Drift Chambers (DC) is the basis of the excellent momentum resolution.
- A Time Expansion Chamber (TEC) in the east arm provides additional tracking and particle identification.
- The Time-of-Flight (TOF) [48] provides particle identification for hadrons. The 85 ps timing resolution of the TOF allows separation of kaons from pions up to 2.5 GeV/c and proton identification out to 5 GeV/c.
- The Ring-Imaging Cherenkov (RICH) detectors detect charged particles having high momentum, which in combination with the EMCal provides electron/photon discrimination.

The central arms consist of tracking systems for charged particles as well as electromagnetic calorimetry. The calorimetry combined with an electron veto provided by the RICH counter is used for photon identification, and by extension through photon-photon invariant mass plots, for π^0 identification, one of the prime objectives of PHENIX, to be used in π^0 asymmetry measurements for extraction of ΔG.

3.3.4 The Muon Arms

The Muon Arms [49, 50, 51, 52], shown in Fig. 3.2, are located in the forward rapidity regions, $-1.1 > \eta > -2.2$ and $1.2 < \eta < 2.4$, with full azimuthal coverage. Each arm, North and South, has two main components, a muon identifier and a muon tracker.

Detector	$\Delta\eta$	$\Delta\phi$	Function
BBC	$\pm$(3.1 to 3.9)	2π	event char., vertex resolution
NTC	$\pm$(1 to 2)	2π	minbias trigger for pp
ZDC/SMD	-	2π	vertex resolution, local polarimetry
DC	$\pm$0.35	$\frac{\pi}{2} \cdot 2$	momentum and mass resolution
PC	$\pm$0.35	$\frac{\pi}{2} \cdot 2$	tracking
TEC	$\pm$0.35	$\frac{\pi}{2}$	pattern recognition, $\frac{dE}{dx}$
RICH	$\pm$0.35	$\frac{\pi}{2} \cdot 2$	electron ID
TOF	(0 - 0.35)	$\frac{\pi}{4}$	hadron ID
EMCal	$\pm$0.35	$\frac{\pi}{2} \cdot 2$	photon and electron detection
MuTr North	(1.2 to 2.4)	2π	tracking, momentum
MuTr South	-(1.2 to 2.2)	2π	tracking, momentum
MuID North	(1.2 to 2.4)	2π	muon ID
MuID South	-(1.2 to 2.2)	2π	muon ID

Table 3.1: PHENIX detector summary

- The muon identifier is composed of 5 layers of transversely-oriented plastic proportional tubes (Iarocci tubes) interleaved with steel absorbers, providing a coarse $x - y$ track position while providing excellent hadron rejection.

- The muon tracker consists of three stations of 2 or 3 tracking chambers inside a radial magnetic field. Each chamber is a gap containing ionizing gas and broken up by charged anode wires that span an approximate arc in the stations that corresponds to an eighth (a half-octant) of the circumference of the detector. The charged particles traversing the muon tracker ionize the gas which then deposits a charge on the anode wires. Each gap is bordered by a pair of readout planes, which are segmented approximately radially by cathode strips, at angles that differ by -11.5 °, +11.5 °and 0 °from the radial direction. The image charges created on the cathode strips are read out and the track location is pinpointed by stereoscopic projection. Voltage is supplied to groups of (usually) 16 wires, for a total 6 or 8 HV anode cards per octant per gap per station per arm.

Each muon spectrometer has a large geometric acceptance of about one steradian and excellent momentum resolution (2%) and muon identification. The PHENIX Muon Arms provide a means of studying vector meson production, the Drell-Yan process (via the detection of muon pairs) and heavy quark production. Z and W production will be studied at forward rapidities (via the detection of single high p_T muons) at higher center of mass energies.

The Muon Arm Tracker design specifications [49] were driven by the requirements that it be able to:

- allow a clean separation of J/ψ from ψ', Υ(1S) from Υ (2S,3S) and ρ/ω from ϕ.

- provide a large enough signal-to-background and acceptance for vector mesons to be able to do statistically significant physics measurements in less than 1 year of RHIC running.
- have low enough occupancy to be able to reconstruct tracks efficiently in central Au+Au events.
- perform well in the lower occupancy but higher event rate p+p and d+Au physics programs.

The electronics design specifications were driven by the requirement that the non-stereo cathode planes provide 100 μm resolution measurements of the particle trajectories and that the readout of the system be able to meet the global PHENIX readout requirements.

3.3.5 Local Polarimeter Analysis

The beam polarization direction at the PHENIX interaction point (PHENIX IP) is measured by using the single transverse-spin asymmetry for neutron production in pp collisions [53]. This asymmetry was discovered in 2002 (Run2) in a pilot experiment at the twelve o'clock interaction point (IP12) to search for any spin effects in the p+p collisions. In the IP12 experiment an electro-magnetic calorimeter system based on lead-tungstate crystals was employed to detect photons and neutrons. A large and negative asymmetry for neutron production (~ -0.11) [54] was measured. These results were confirmed towards the end of that run using a hadronic calorimeter system based on one Zero Degree Calorimeter (ZDC) module situated on the opposite side of the IR at IP12. At $\phi = -\pi/2$, the asymmetry was calculated as:

$$A_N(\phi) = (N(\text{left}) - N(\text{right}))/(N(\text{left}) + N(\text{right})) \tag{3.2}$$

and at $\phi = 0$:

$$A_N(\phi) = (N(\text{bottom}) - N(\text{top}))/(N(\text{bottom}) + N(\text{top})) \tag{3.3}$$

This unexpectedly discovered analyzing power was used to monitor the polarization vector at the PHENIX IP in RHIC Run3pp. In Run3pp the neutron asymmetry was measured using the ZDC (3 modules) and newly installed Shower Max Detector (SMD) between the first and the second ZDC module (counting from the PHENIX IP direction).

The analysis comprised of two parts: neutron identification and asymmetry calculation. Neutrons were identified by requiring energy deposition in the second module of the ZDC. Since one ZDC module is 50 radiation lengths long, any electro-magnetic component of the shower produced in the collisions was absorbed in the first module. In the course of the analysis, it was found that requiring the energy deposited in the second module is equivalent to requiring hits in the SMD.

Requiring hits in the SMD is actually essential in the asymmetry calculation since the hit position of neutron is required. The SMD is the two layers of the scintillation hodoscope in x and y directions. A PISA simulation showed that hadronic shower induced by high energy neutrons produces at least two hits in each direction. Therefore at least two "hits" in each hodoscope are required. The center of gravity of the shower is calculated using the ADC counts in each hit, and is then used as the hit position of the neutron.

3.4 Data Acquisistion

The general method and procedure of Data AcQuisition (DAQ), like the experimental setup, has been more than adequately described in previous dissertations

[51, 55] as well as technical papers [56]. Here we will only give a brief overview.

The acquisition of data from a large experiment such as PHENIX requires a concerted effort by a large number of people. In order not to be overwhelmed by the volume of data, and to prevent loss of desired events, a system of triggers is used. Selected detectors are used for this purpose, which must have fast information available upon which to trigger.

The information from each sub-detector is buffered by the Front End Modules (FEMs). If the event is selected by the local level 1 (LL1) trigger, the data from each sub-detector is then gathered in the corresponding sub-event builder (SEB). The event builder (EvB) reconstructs the event when all SEBs have acquired the data from that event.

Since PHENIX can record events at the maximum rate of 25 kHz, a hardware trigger system is needed to reduce event rate to within this limitation. An electron trigger is used to enrich data. In particular, the electron trigger in PHENIX is realized with the EMCal-RICH trigger system (ERT), and considered to be a sub-system in its own right. It is composed of the EMCal Level 1 trigger system and the RICH Level 1 trigger system.

The RICH Level 1 trigger system produces a trigger bit when the charge signal gained from the RICH trigger tiles exceeds over the threshold of three photo-electrons. The 256 RICH trigger tiles, each of which consists of photo-multipliers (PMTs), cover all 5120 PMTs in the RICH. The trigger threshold are determined by simulations to optimize the detection efficiency and the rejection power. The rejection power is defined by the ratio of the number of minimum bias events to the number of triggered events. They are installed into the RICH Front-End Electronics (RICH FEE) in the PHENIX.

The front end electronics of the electromagnetic calorimeter (EMCal) is capable

of detecting electrons and photons above three different programmable thresholds (4x4a, 4x4b and 4x4c) in overlapping trigger tiles and above one programmable threshold (2x2) in non-overlapping tiles. Each tile processes the signals from 2x2 PMTs and each Front End Module (FEM) collects the signals from 36 tiles. This unit of 36 tiles is called supermodule. There are 172 EMCal supermodules present; 108 for the PbSc and 64 for the PbGl. Supermodules within one sector are connected, *i.e.* the summation of the signals of overlapping tiles will also be done across supermodule borders.

Thresholds can be set at 63 different values (DAC tics) for each tile separately. Trigger information is only available at the supermodule level, *i.e.* the data only contains the information which supermodule created the trigger. This also means it is only possible to mask of whole supermodules in case a trigger tile becomes noisy and the rejection factors become too low.

The last thing that should be mentioned regarding the acquisition of data is that in Run 3 (Au+Au and p+p) quality assurance through online calibration was used for the first time. By filtering and copying a selected portion of the data before transfer to storage, quick analysis and mass reconstruction of J/ψ in the muon arms and π^0 reconstruction in the central arms was done to insure good data quality.

Chapter 4

Methodology

After looking at the experimental facility at which the data was taken for the present analysis, we will now examine the method used to obtain a measure of POAM. The two quantities that we will extract from our analysis are $\sqrt{\langle j_T^2 \rangle}$ and $\sqrt{\langle k_T^2 \rangle}$. If we measure an imbalance in $\sqrt{\langle k_T^2 \rangle}$ between parallel and anti-parallel helicity events, this could be an indication of the presence of POAM. k_T (intrinsic partonic transverse momentum) has been defined in Section 1.4; while j_T (transverse fragmentation momentum) is illustrated and explained in Fig. 4.2.

4.1 Jet-Jet Correlations

The properties of jets produced in p+p collisions at $\sqrt{s} = 200$ GeV are measured using the method of two particle correlations first used at CERN-ISR [57, 58] and developped extensively by J. Rak and others for spin-uncorrelated j_T and k_T measurements at PHENIX [59, 60, 23, 22].

In Fig. 4.1 we represent a two jet hard scattering event from a p+p collision in the transverse plane. The dashed lines represent the two jets in the partonic center-

of-mass frame. The two jets are therefore back-to-back with equal and opposite momenta in this plane. They may be acoplanar in the z-direction as the center-of-mass boost for two partons with momentum fractions x_1, x_2 is:

$$y_{cm} = \frac{1}{2} \ln \left(\frac{x_1}{x_2} \right) \tag{4.1}$$

but in the transverse plane they will be colinear.

However, because of k_T they are no longer back-to-back in the lab frame. Their momenta are now represented by the solid lines and are now acoplanar. If we could measure the final transverse momenta of the two jets directly we would have a measurement of the initial partonic transverse momenta $k_{T,1} + k_{T,2}$, which we will henceforth call $\vec{k}_{T\text{pair}}$.

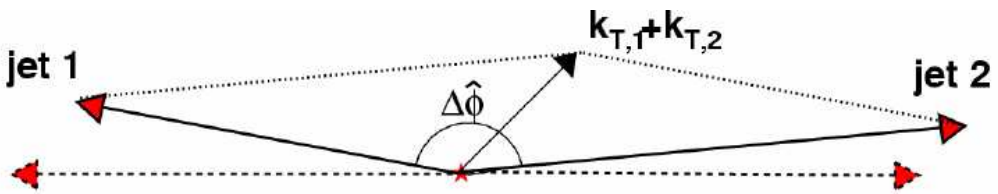

Figure 4.1: Jet-jet collision in the transverse plane. The colinearity of the two jets is broken by partonic k_T.

Unfortunately, we can only measure particles that have hadronized from the partons, which complicates matters. Fig. 4.2 shows that when the initial parton with transverse montum $\hat{p}_T$ hadronizes the resulting particle carries transverse momentum p_T which differs in direction from the initial parton by a finite angle α^*. The transverse momentum of the hadron differs from its projection on the parton transverse momentum by a quantity called j_T: transverse fragmentation momentum.

Instead of studying two-jet correlations, which is not possible at PHENIX, we will study two-particle correlations by plotting $\Delta\phi$, their angular separation in the

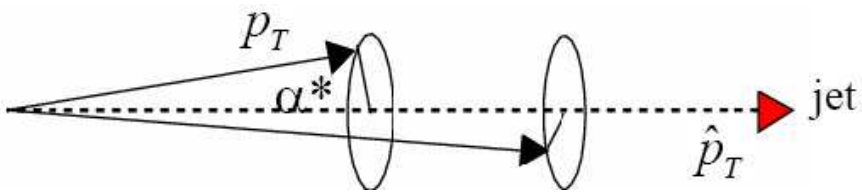

Figure 4.2: Jet fragmentation. The $\hat{p}_T$ of the initial parton is not the same as the p_T of the detected particle, nor are they even colinear. The perpendicular p_T boost due to fragmentation is called j_T.

transverse plane, to obtain a figure similar to Fig. 4.3. When the angular separation is small, *i.e.* the event is in the first, narrower peak, the two particles come from the same jet. The width (σ_N) of this first, near-side, peak gives us a measurement of j_T. The two particles may also come from the two opposite jets, *i.e.* their angular separation lands in the second, wider, far-side peak. The width (σ_F) of this far-side peak gives us a convolution of j_T with the fragmentation variable, z, and the partonic transverse momentum, k_T. z is determined through a combined analysis of the measured π^0 inclusive and associated spectra by determining the jet Fragmentation Function.

The specific particles used in this correlation study will be the π^0 for the leading, trigger particle and a charged hadron ($h^{\pm}$) for the associated particle. This choice reflects the PHENIX detector capabilities as well as trigger bias. Since a key analysis for PHENIX is the π^0 A_{LL} analysis, π^0 detection and trigger efficiency is relatively well understood.

4.2 Jet Angular Correlations

A more complete diagram of the intial and final state variables of this analysis is shown in Fig. 4.4.

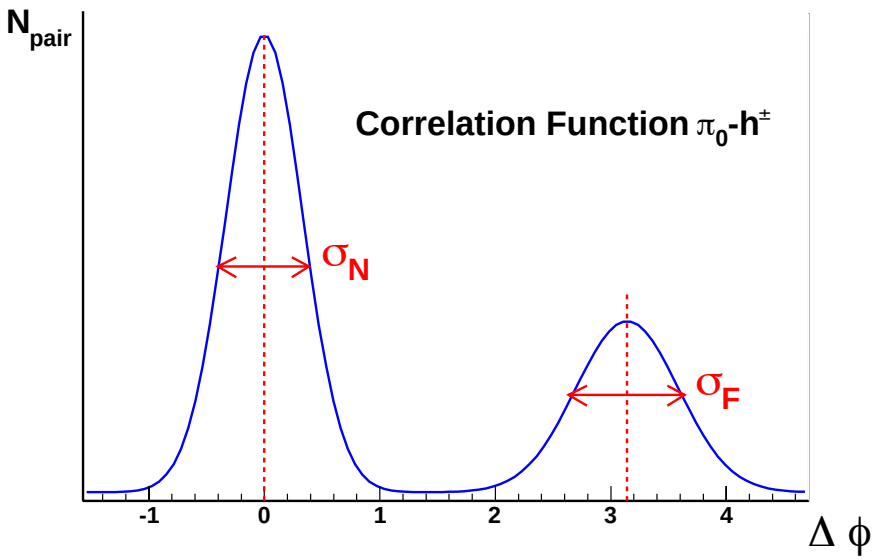

Figure 4.3: Cartoon azimuthal angle Correlation Function

The transverse plane is still a two dimensionnal plane and we can consider k_T a vector with components $k_{T\mathrm{x}}$ and $k_{T\mathrm{y}}$. We will label the jet-jet direction as the x direction, and y to be perpendicular to the jet-jet direction.

The two components of k_T then result in different experimentally measurable effects. $k_{T\mathrm{y}}$ leads to the acoplanarity of the di-jet pair while $k_{T\mathrm{x}}$ makes the momenta of the jets unequal which results in the smearing of the steeply falling p_T spectrum as mentioned in Chapter 2. This causes the measured inclusive jet or single particle cross section to be smeared by more higher-p_T particles than the expected pQCD value.

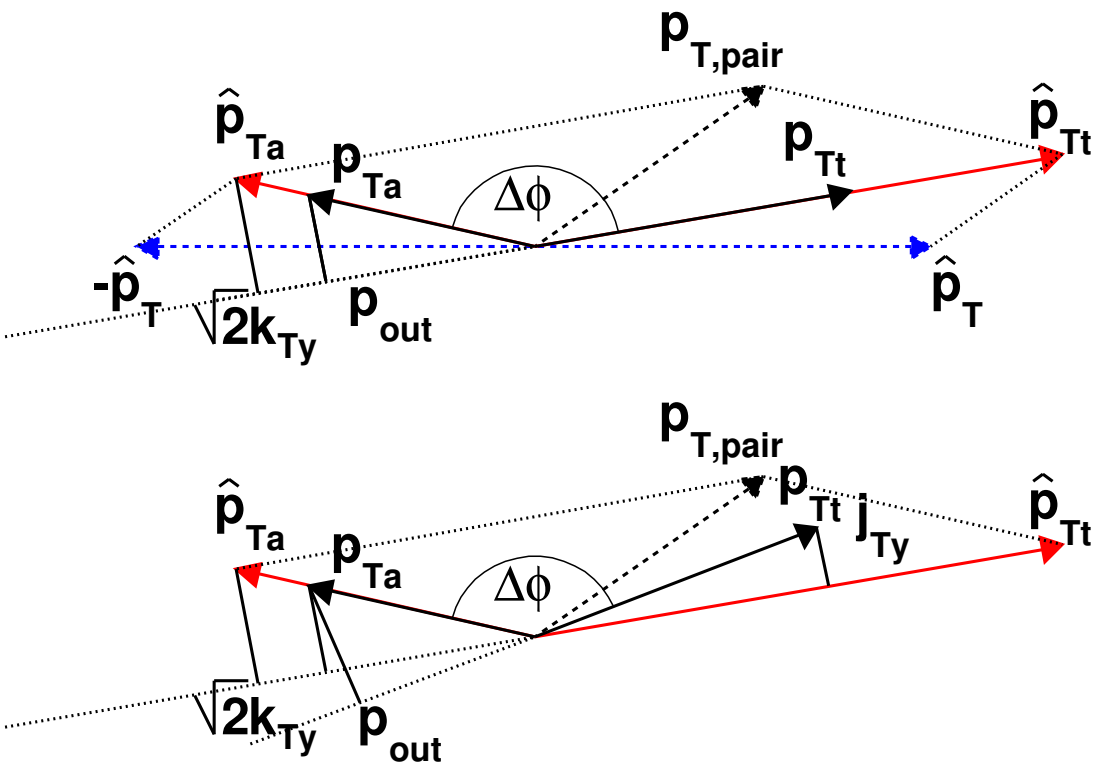

Figure 4.4: *(a)* Schematic view of a hard scattering event in the plane perpendicular to the beam. Two scattered partons with transverse momenta $\hat{p}_T$ in the partons' center of mass frame are seen in the laboratory frame to have momenta $\hat{p}_{T\mathrm{t}}$ and $\hat{p}_{T\mathrm{a}}$. The net pair transverse momentum $\hat{p}_{T\mathrm{pair}}$ corresponds to the sum of two $\vec{k}_T$-vectors of the trigger and associated jet. The trigger and associated jet fragment producing high-p_T particles labeled as $p_{T\mathrm{t}}$ and $p_{T\mathrm{a}}$. The projection of k_T perpendicular to $\hat{p}_{T\mathrm{t}}$ is labeled as $k_{T\mathrm{y}}$. The transverse momentum component of the away-side particle $\vec{p}_{T\mathrm{a}}$ perpendicular to trigger particle $\vec{p}_{T\mathrm{t}}$ is labeled as p_{out}. *(b)* The same schematics as in *(a)*, but the trigger and associated jet fragmentation transverse momentum component $j_{T\mathrm{yt}}$ and $j_{T\mathrm{ya}}$ are also shown.

4.3 Correlation Functions

As previously mentioned, this analysis uses two-particle azimuthal correlation functions between a π^0 and associated charged hadron ($h^{\pm}$) to measure the distribution of the azimuthal angle difference $\Delta\phi = \phi_t - \phi_a$ (see Fig. 4.5).

The Correlation Function is defined as:

$$C\left(\Delta\phi\right) = \mathcal{N} \cdot \frac{N_{corr}\left(\Delta\phi\right)}{N_{uncorr}\left(\Delta\phi\right)} \tag{4.2}$$

where $N_{corr}\left(\Delta\phi\right)$ is the observed $\Delta\phi$ distribution for $\pi^0 - h^{\pm}$ particle pairs in the same event, $N_{uncorr}\left(\Delta\phi\right)$ is the $\Delta\phi$ distribution for particle pairs selected from mixed events and $\mathcal{N} = \sum N_{uncorr} / \sum N_{corr}$, the normalization constant. Mixed events were obtained by randomly selecting each member of a particle pair from different events having similar vertex position. Two methods are now available for the analysis:

- We divide the Correlation Function by the mixed event distribution whic corrects effects due to the limited PHENIX azimuthal acceptance and for the detection efficiency. We then fit the measured Correlation Function by two Gaussians, one for the near-side component (around $\Delta\phi = 0$) and one for the far-side component (around $\Delta\phi = \pi$), and a constant for the uncorrelated pairs from the underlying event. This leaves a total of five free parameters to be determined - the areas and widths of the above two Gaussians: Y_N,σ_N for the near-angle component and Y_F, σ_F for the far-angle component and the constant term describing an uncorrelated distribution of particle pairs which are not associated with jets.

- The second more recently developped [22] method involves fitting the raw data to a Gaussian in the near side peak and to a modified Gaussian, Eq. (4.15), in the far side peak from which we will extract $p_{\rm out}$ and then using Eq. (4.14)

calculate $x_h^{-1} \langle z_t \rangle \sqrt{\langle k_T^2 \rangle}$. This second method is more theoretically sound and provides more accurate results, it is the method we shall use in our analysis. The $\sqrt{\langle j_T^2 \rangle}$ value is extracted directly from the near side peak width σ_N, as with the first method.

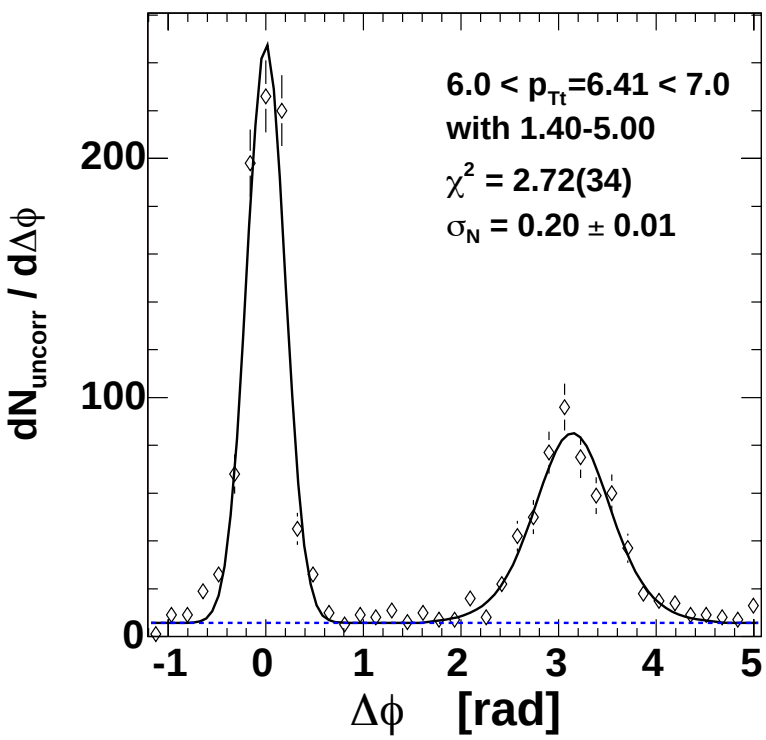

Figure 4.5: Correlation Function. The $\sqrt{\langle j_T^2 \rangle}$ value is extracted directly from the near side peak width σ_N.

For two particles with transverse momenta $p_{T\mathrm{t}}$, $p_{T\mathrm{a}}$ from the same jet, the width of near-side correlation distribution, Fig. 4.5, can be related to the RMS value of the

two-dimensional vector j_T as:

$$\sqrt{\langle j_T^2 \rangle} = \sqrt{2 \left\langle j_{Ty}^2 \right\rangle} \simeq \sqrt{2} \frac{p_{T\mathrm{t}} \cdot p_{T\mathrm{a}}}{\sqrt{p_{Tt}^2 + p_{Ta}^2}} \sigma_N \tag{4.3}$$

in the case when $\sqrt{\langle j_T^2 \rangle} \ll p_{T\mathrm{t}}$ and $p_{T\mathrm{a}}$.

In order to extract $\langle |k_{T\mathrm{y}}| \rangle$, or $\sqrt{\left\langle k_{T\mathrm{y}}^2 \right\rangle}$ we start with the relation between $\langle |p_{\mathrm{out}}| \rangle$, the average absolute transverse momentum component of the away-side particle $\vec{p}_{T\mathrm{a}}$ perpendicular to trigger particle $\vec{p}_{T\mathrm{t}}$ in the azimuthal plane (see Fig. 4.4), and $k_{T\mathrm{y}}$,

$$\langle |p_{\mathrm{out}}| \rangle^2 = x_E^2 \left[2 \langle |k_{T\mathrm{y}}| \rangle^2 + \langle |j_{T\mathrm{y}}| \rangle^2 \right] + \langle |j_{T\mathrm{y}}| \rangle^2 \tag{4.4}$$

where:

$$x_E = \frac{\vec{p}_{T\mathrm{t}} \cdot \vec{p}_{T\mathrm{a}}}{p_{T\mathrm{t}}^2} = \frac{p_{T\mathrm{a}} \cdot \cos \Delta\phi}{p_{T\mathrm{t}}} \tag{4.5}$$

represents the fragmentation variable of the away-side jet. Furthermore, as mentioned earlier, the average values of trigger and associated jet momenta are generally not the same. There is a systematic momentum imbalance due to k_T-smearing of the steeply falling parton momentum distribution. The event sample with a condition of $p_{T\mathrm{t}} > p_{T\mathrm{a}}$ is dominated by configurations where the k_T-vector is parallel to the trigger jet and antiparallel to the associated jet and $(\hat{p}_{T\mathrm{t}} - \hat{p}_{T\mathrm{a}}) \neq 0$. Here we introduce the hadronic variable x_h in analogy to the partonic variable $\hat{x}_h$:

$$x_h = \frac{p_{T\mathrm{t}}}{p_{T\mathrm{a}}} \tag{4.6}$$

and

$$\hat{x}_h \left(\left\langle {k_T}^2 \right\rangle, x_h \right) = \frac{\hat{p}_{Tt}}{\hat{p}_{Ta}} \tag{4.7}$$

In order to derive the relation between the magnitude of $p_{\rm out}$ and k_T let us first consider the simple case where we have neglected both trigger and associated j_T (see panel (a) on Fig. 4.4). In this case one can see that

$$\begin{aligned} \langle |p_{\rm out}| \rangle \,|_{j_{Tt}=j_{Ta}=0} &= \langle |p_{\rm out}| \rangle_{00} \\ &= \sqrt{2}\, \langle |k_{T\rm y}| \rangle \, \tfrac{p_{T\rm a}}{\langle \hat{p}_{Ta} \rangle} \\ &= \sqrt{2}\, \langle |k_{T\rm y}| \rangle \, \langle z_t \rangle \, \tfrac{x_h}{\hat{x}_h} \end{aligned} \tag{4.8}$$

Rewriting the formula for $p_{\rm out}$ in terms of $\sqrt{\langle k_T^2 \rangle}$, we get:

$$\sqrt{\langle p_{\rm out}^2 \rangle_{00}} = \langle z_t \rangle \sqrt{\langle k_T^2 \rangle} \frac{x_h}{\hat{x}_h} \tag{4.9}$$

where we have taken $\left\langle {k_T}^2 \right\rangle = \left\langle 2k_{T\rm y}^2 \right\rangle$.

However, the jet fragments are produced with finite jet transverse momentum j_T. The situation when the trigger particle is produced with $j_{T\rm yt} > 0$ GeV/c and the associated particle with $j_{T\rm ya} = 0$ GeV/c is shown on Fig. 4.4 part (b). The $p_{\rm out}$ vector picks up an additional component:

$$\left\langle p_{\rm out}^2 \right\rangle |_{j_{Tt}>0, j_{Ta}=0} = \left[\left\langle p_{\rm out}^2 \right\rangle_{00} + \frac{\left\langle j_{Tty}^2 \right\rangle}{p_{T\rm t}^2} \left(p_{T\rm a}^2 - \left\langle p_{\rm out}^2 \right\rangle_{00} \right) \right] \frac{p_{T\rm t}^2 - \left\langle j_{Tty}^2 \right\rangle}{p_{T\rm t}^2} \tag{4.10}$$

With an assumption of $j_{T\rm yt} << p_{T\rm t}$ we found that:

$$\left\langle p_{\rm out}^2 \right\rangle |_{j_{Tt}>0, j_{Ta}=0} = x_h^2 \left[\langle z_t \rangle^2 \left\langle {k_T}^2 \right\rangle \frac{1}{\hat{x}_h} + \left\langle j_{Tty}^2 \right\rangle \right] \tag{4.11}$$

We include j_{Ta} in the same approximation, $j_{T\rm ya} << p_{T\rm t}$, *i.e.* colinearity of j_{Ta} and $p_{\rm out}$, with the result that:

$$\left\langle p_{\rm out}^2 \right\rangle = x_h^2 \left[\langle z_t \rangle^2 \left\langle {k_T}^2 \right\rangle \frac{1}{\hat{x}_h} + \left\langle j_{Tty}^2 \right\rangle \right] + \left\langle j_{Tay}^2 \right\rangle \tag{4.12}$$

and we solve for $x_h^{-1} \langle z_t \rangle \sqrt{\langle k_T^2 \rangle}$:

$$x_h^{-1} \langle z_t \rangle \sqrt{\langle k_T^2 \rangle} = x_h^{-1} \sqrt{\langle p_{\rm out}^2 \rangle - \left\langle j_{Tay}^2 \right\rangle - x_h^2 \left\langle j_{Tty}^2 \right\rangle} \tag{4.13}$$

If we assume no difference between j_{Tt} and j_{Ta} then we have:

$$\frac{\langle z_t(k_T, x_h) \rangle \sqrt{\langle k_T^2 \rangle}}{\hat{x}_h(k_T, x_h)} = x_h^{-1} \sqrt{\langle p_{\rm out}^2 \rangle - \left\langle j_{Ty}^2 \right\rangle (1 + -x_h^2)} \tag{4.14}$$

All quantities on the right-hand side of Eq. (4.14) can be directly extracted from the Correlation Function. The Correlation Functions are measured in the variable $\Delta\phi$ in bins of $p_{T\rm t}$ and $p_{T\rm a}$, and the RMS of the near and away peaks σ_N and σ_F are extracted.

We extract $\sqrt{p_{\rm out}^2}$ directly for all values of $p_{T\rm a}$ and $p_{T\rm t}$ by fitting the correlation function in the $\pi/2 < \Delta\phi < 3\pi/2$ region by

$$\left.\frac{dN_{away}}{d\Delta\phi}\right|_{\pi/2}^{3\pi/2} = \frac{dN}{dp_{\rm out}} \frac{dp_{\rm out}}{d\Delta\phi} = \frac{-p_{T\rm a} \cos\Delta\phi}{\sqrt{2\pi < p_{\rm out}^2 >} Erf\left(\frac{\sqrt{2} p_{T\rm a}}{< p_{\rm out}^2 >}\right)} e^{\left(-\frac{p_{T\rm a}^2 \sin^2 \Delta\phi}{2\left\langle p_{\rm out}^2 \right\rangle}\right)} \tag{4.15}$$

where we assumed a Gaussian distribution in $p_{\rm out}$. We use a Gaussian function in $\Delta\phi$ in the near angle peak to extract $\sqrt{\langle j_T^2 \rangle}$.

To summarize, our results are given in terms of σ_N and $p_{\rm out}$ which we extract directly from the Correlation Functions, and the derived quantities $\sqrt{\langle j_T^2 \rangle}$ and $x_h^{-1} \langle z_t \rangle \sqrt{\langle k_T^2 \rangle}$.

We go one step closer to $\sqrt{\langle k_T^2 \rangle}$ by extracting $\langle z_t \rangle \sqrt{\langle k_T^2 \rangle}$ by assuming that within the bins used in analysis (see Chapter 6):

$$\hat{x}_h^{-1} = \frac{\bar{p}_{Ta}}{\bar{p}_{Tt}} \tag{4.16}$$

where $\bar{p}_{Ta}$ and $\bar{p}_{Tt}$ are the mean $p_{T\rm a}$ and $p_{T\rm t}$ in the bins being considered.

Chapter 5

Analysis

5.1 π^0 Analysis

5.1.1 π^0 Trigger

Since we depend so heavily on proper π^0 identification and triggering information, it is relevant to include a short discussion on the π^0 analysis. For such an analysis we used mainly statistics from the trigger selection known as ERT_Gamma3&BBCLL1 (below we'll call it Gamma3). This selection is a trigger combination of BBC and EMCal trigger combined with a lack of trigger from the RICH, effectively triggering on high p_T photons.

The π^0 cross section analysis is done following the same approach as described in PHENIX publications [61, 62, 63, 64]. Minimum bias trigger is formed by two beam-beam counters (BBC) requiring at least one PMT fired in each BBCs. An online collision z-vertex cut of ± 30 cm was imposed.

The asymmetry analysis is based on π^0 counting in each bunch crossing in each

run, luminosity measurements [65] and beam polarization measurements [53].

5.1.2 Particle Reconstruction

A p+p data sample corresponding to a PHENIX-sampled integrated luminosity of 0.35 pb^{-1} at $\sqrt{s} = 200$ GeV was used for the π^0 analysis.

The minimum bias (MB) trigger is obtained from the charge multiplicity in the two BBCs situated at large pseudo-rapidity ($\eta \approx \pm(3.0 - 3.9)$). The BBCs were also used to determine the collision vertex, which is limited to a $\pm$ 30 cm range in this analysis. The high-p_T trigger requires an additional discrimination on sums of the analog signals from non-overlapping, 2x2 groups of adjacent EMCal towers situated at mid-rapidity ($|\eta| < 0.35$) equivalent to an energy deposition of 750 MeV .

Neutral pions, which are used as trigger particles, are detected by the reconstruction of their $\gamma\gamma$ decay channel. Photons are detected in the EMCal, which has a timing resolution of $\approx$ 100 ps (PbSc) and $\approx$ 300 ps (PbGl) and energy resolution of $\sigma_E/E = 1.9\% \oplus 8.2\%/\sqrt{E(GeV)}$ (PbSc) and σ_E/E =$0.8\% \oplus 8.4\%/\sqrt{E(GeV)}$ (PbGl). In order to improve the signal/background ratio we require the minimum hit energy > 0.3 GeV , a shower profile cut as described in other analyses, and no accompanying hit in the RICH detector, which serves as a veto for conversion electrons. A sample of the invariant mass distribution of photon pairs detected in the EMCal is shown in Fig. 5.1.

5.1.3 Pion Selection

To reject the photon conversion backgrounds in the charged pion candidates, the shower information in the EMCal is used. Since most of the background electrons are genuine low p_T particles that were mis-reconstructed as high p_T particles, simply

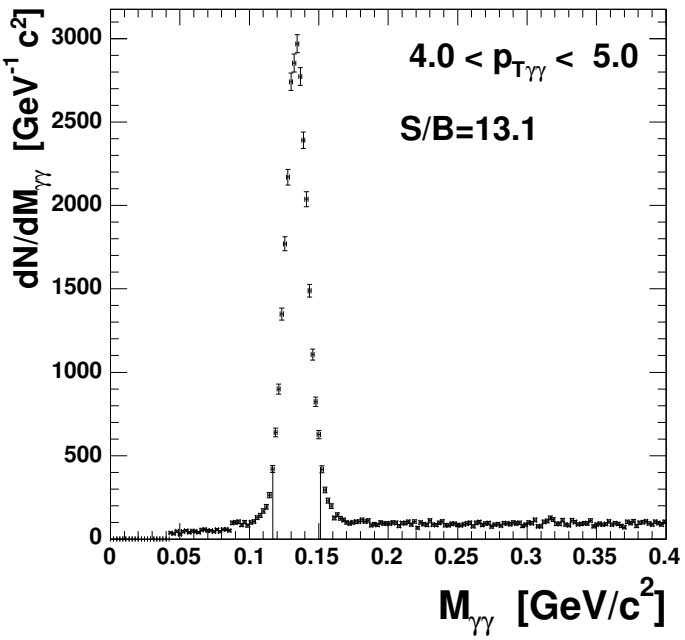

Figure 5.1: The measured $\gamma\gamma$ invariant mass distribution for pair p_T in $4 < p_{T\gamma\gamma} < 5$ GeV/c. The peak is fitted with a Gaussian to measure width and estimate error. The signal/background ratio within 2σ of the mean ranges from $\approx$6 at 3 GeV/c up to $\approx$ 15 at 8 GeV/c.

requiring a large deposition of shower energy in the EMCal is effective in suppressing the electron background. In this analysis a momentum dependent energy cut at EMCal is applied:

$$E > 0.3 + 0.15 p_T \tag{5.1}$$

In addition to this energy cut, the shower shape information is used to further separate the broad hadronic showers from the narrow electromagnetic showers and hence reduce conversion backgrounds. The difference of the EM shower and hadronic

shower is typically characterized by a χ^2 variable,

$$\chi^2 = \sum_i \frac{\left(E_i^{meas} - E_i^{pred}\right)^2}{\sigma_i^2} \tag{5.2}$$

where E_i^{meas} is the energy measured at tower i and E_i^{pred} is the predicted energy for an electromagnetic particle of total energy $\sum_i E_i^{meas}$. We use the probability calculated from this χ^2 value for an EM shower, ranging from 0 to 1 with a flat distribution expected for an EM shower, and a peak around 0 for an hadronic shower.

5.2 Spin-Sorted Analysis

This analysis uses the code and principles developed in previous jet-jet correlations analyses on *Au+Au* and *p+p* k_T studies[59, 60, 23, 22], takes the spin information provided by the Relative Luminosity Working Group (RLWG) [65] combined with polarization information from the local polarimeter (see Chapter 3) and looks at the asymmetry in the results for parallel and anti-parallel helicity configurations. The run selection for this analysis is the same as for the non-spin analysis, amputated of the runs that did not have polarization information provided by the local polarimetry group. Even when the spin information is provided, some of the runs have very little good polarization information, and consequently do not contribute much statistics, as we only consider events from bunch crossings that have well measured polarizations. A total of 197 runs were used (Table 5.1) for a total of 18.8M events.

The cuts for the π^0 are the same as for the π^0 analysis [60], and described in Section 5.1, namely:

- Events
  - abs(z vertex) $<$ 30 cm

87621	87623	87625	87689	87691	87693	87703	87705	87791
87793	87829	87832	87835	87839	87841	87843	87845	87899
87901	87904	87906	87908	87910	87912	87923	87925	87927
87929	87932	87997	87999	88115	88125	88127	88129	88131
88243	88258	88260	88351	88396	88460	88462	88466	88471
88475	88578	88580	88582	88584	88586	88825	88827	88829
88846	88869	88873	88877	88879	88944	88946	88962	88964
88993	88995	88999	89001	89003	89080	89092	89096	89098
89100	89103	89105	89117	89119	89121	89128	89130	89135
89211	89297	89299	89303	89316	89318	89321	89323	89325
89345	89451	89453	89463	89520	89527	89529	89541	89618
89624	89626	89629	89634	89642	89644	89646	89648	89683
89685	89693	89695	89697	89707	89709	89711	89713	89715
90202	90209	90211	90213	90215	90217	90219	90226	90228
90302	90303	90306	91262	91268	91270	91273	91275	91314
91316	91318	91321	91375	91443	91447	91449	91452	91455
91457	91460	91462	91464	91472	91474	91476	91478	91596
91599	91601	91679	91681	91716	91718	91720	91726	91729
91731	91840	91842	91844	91846	91848	91851	91853	91855
91977	91979	91983	91985	91987	92002	92018	92030	92034
92047	92192	92194	92228	92230	92232	92234	92238	92242
92244	92432	92434	92436	92438	92440	92444	92446	

Table 5.1: Run selection

  - mixed event abs (Δ z vertex) < 3 cm

- Trigger π^0
  - Asymmetry < 0.9
  - probPhot 0.1
  - $\chi^2 < 3.0$
  - $E_{min} < 0.3$

In addition to the cuts mentioned above, a photon time-of-flight (TOF) cut is made. The photon times are plotted for events in both the PbSc and PbGl. A

gaussian is fitted to the graph and then the width of gaussian is used as a parameter, σ. In Fig. 5.2, which shows photon candidates in the PbSc for a particular tower in run 88243, the red lines represent the 2 σ deviation region.

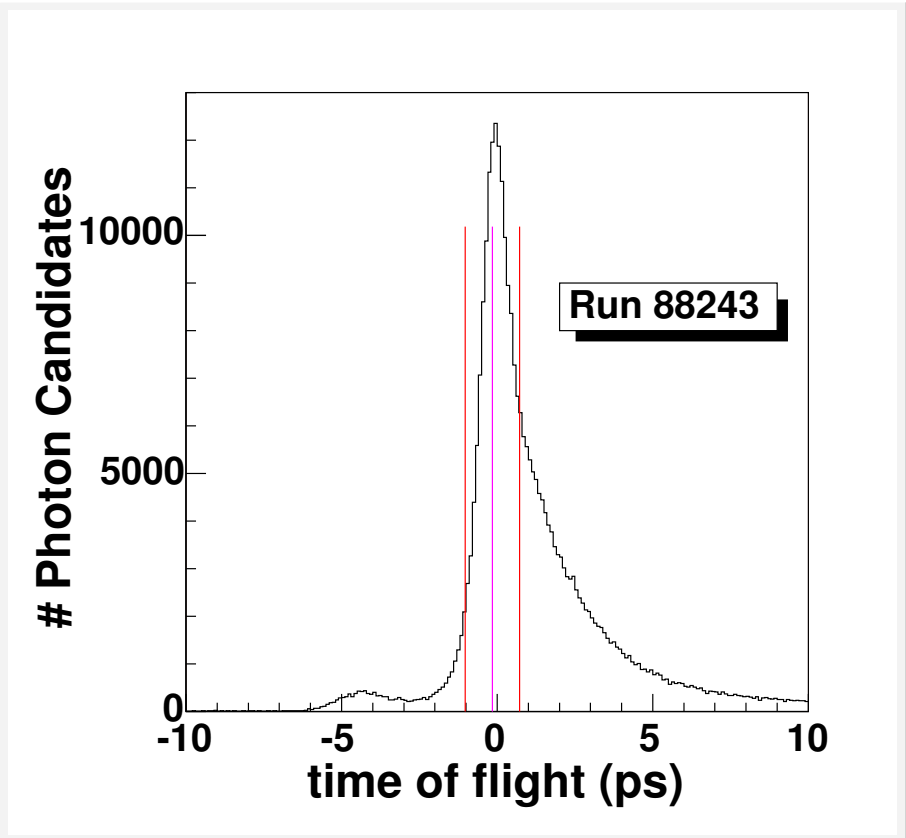

Figure 5.2: Time of flight of photon candidates in the lead scintillator EM Calorimeter for run 88243. The red lines represent the 2 σ deviation region.

Charged particles are reconstructed in each PHENIX central arm using a drift chamber, followed by two layers of multiwire proportional chambers with pad readout. Particle momenta are measured with a resolution $\delta p/p = 0.7\% + 1.1\%$ GeV/c. A confirmation hit is required in PC2. We also require that no signal in the RICH detector is associated with these tracks. These requirements eliminate charged particles which do not originate from the event vertex, such as beam albedo and weak

decays, as well as conversion electrons. The more important cuts include:

- 2 σ match between PC2 and PC3
- 2 σ EmCal match
- $\pm$ 75 cm DC track

5.3 Systematic Errors

The systematic errors explored extensively in previous works on jet-jet azimuthal correlations [59, 60, 23, 22] are not considered to first order. Since the object is to compare, *i.e.* take the difference between, parallel and anti-parallel helicity event sub-sets, systematic errors should cancel to a very large degree, as is the assumption for all asymmetry measurements. A check was made on the z-vertex distribution to confirm this impression (see Fig. 5.3).

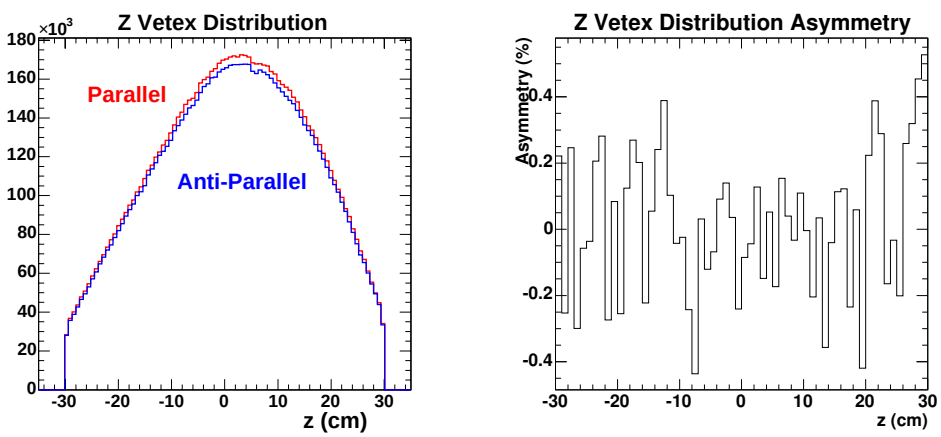

Figure 5.3: *(left)* Vertex distribution for parallel and anti-parallel helicity events. *(right)* Vertex distribution asymmetry.

The Bunch Shuffling technique was also used (see Section 6.5) to confirm that the errors are essentially statistical in nature, or at the very least accounted for in our error bars. The error bars on σ_N and p_{out} are taken from the CF fitting routine, and the errors on the extracted values j_T, $x_h^{-1}\langle z_t\rangle\sqrt{\langle k_T^2\rangle}$, and $\langle z_t\rangle\sqrt{\langle k_T^2\rangle}$ are given by the following formulae:

$$\begin{aligned}
\delta j_T &= \delta\sigma_N \cdot \tfrac{\bar{p}_{Ta}\bar{p}_{Tt}}{\sqrt{\bar{p}_{Ta}^2+\bar{p}_{Tt}^2}}\sqrt{2} \\
\delta\left(x_h^{-1}\langle z_t\rangle\sqrt{\langle k_T^2\rangle}\right) &= \sqrt{\tfrac{(\delta p_{\text{out}})^2\cdot p_{\text{out}}^2+\left(j_{T\text{y}}\cdot\delta j_{T\text{y}}\cdot(1+x_h^2)\right)^2}{x_h^2\cdot\left(p_{\text{out}}^2-j_{T\text{y}}^2\cdot(1+x_h^2)\right)}} \\
\delta\left(\langle z_t\rangle\sqrt{\langle k_T^2\rangle}\right) &= \tfrac{\delta\left(x_h^{-1}\langle z_t\rangle\sqrt{\langle k_T^2\rangle}\right)}{x_h^{-1}\langle z_t\rangle\sqrt{\langle k_T^2\rangle}}\langle z_t\rangle\sqrt{\langle k_T^2\rangle}
\end{aligned} \tag{5.3}$$

where we use the notation δ for the error, so as not to confuse with Δ used for the difference in results between two data sets. $j_{T\text{y}}$ is related to j_T by a factor of $\sqrt{2}$ and x_h is given by Eq. (4.16).

We see that δj_T depends on $\delta\sigma_N$, and the errors for the two other derived quantities depend on both $\delta\sigma_N$ and δp_{out}. Finally we note that the third equation of Eq. (5.3) shows that the relative error for the last two quantities are the same.

Chapter 6

Results

6.1 Correlation Functions

The basis of the analysis is the extraction of the quantity $\langle z_t \rangle \sqrt{\langle k_T^2 \rangle}$ from the Correlation Function. The Correlation Function is the azimuthal angle distribution for $\pi^0 - h^\pm$ particle pairs (see Section 4.3). Run3pp is relatively poor in statistics, so to get a result with reasonable statistical error bars we have split the statistics into only two bins, given in Table 6.1.

	Bin 1	Bin 2
$p_{T\mathrm{t}}$	$1 < p_{T\mathrm{t}} \leq 3\mathrm{GeV}/c$	$3 < p_{T\mathrm{t}} \leq 7\mathrm{GeV}/c$
$p_{T\mathrm{a}}$	$1 < p_{T\mathrm{a}} \leq 4\mathrm{GeV}/c$	$1 < p_{T\mathrm{t}} \leq 4\mathrm{GeV}/c$

Table 6.1: $p_{T\mathrm{t}}$ and $p_{T\mathrm{a}}$ values for 2-bin analysis

The Correlation Functions (CFs) for the two bins are shown in Fig. 6.1 and Fig. 6.2. Fig. 6.1 shows the uncorrected $\Delta\Phi$ distributions and the mixed event PHENIX detector acceptance and efficiency background. Fig. 6.2 shows the functions normalized and corrected for backgrounds. These functions are fit to a constant plus two Gaussians, one for the near side peak and one for the away side peak (the far side peak is fitted to a modified Gaussian, see Section 4.3). The χ^2/DOF values for the fits to the different uncorrected CFs are given in Table 6.2.

χ^2/DOF	$1 < p_{T\mathrm{t}} < 3$	$3 < p_{T\mathrm{t}} < 7$
parallel helicity	4.63(34)	2.33(34)
anti-parallel helicity	3.07(34)	2.13(34)

Table 6.2: Correlation Function χ^2/DOF values. The number of degrees of freedom (NDF) are given in parentheses.

Two things need to be noted:

1. We are using the second method described in Section 4.3 which fits a Gaussian and a modified Gaussian to the uncorrected CFs.

2. The χ^2/DOF values are not outstanding but they are significantly better than the values obtained from the first method which fits two Gaussians to the corrected CFs. These bad fits stem from the fact that we still do not fully understand the origin of the extra "bumps" present at $\pi/2$ and $3\pi/2$ in the corrected CFs. Study and simulation are ongoing in order to determine whether they come from background or perhaps our mixed event pool is inaccurate, or perhaps some physics phenomenon has not been properly acccunted for.

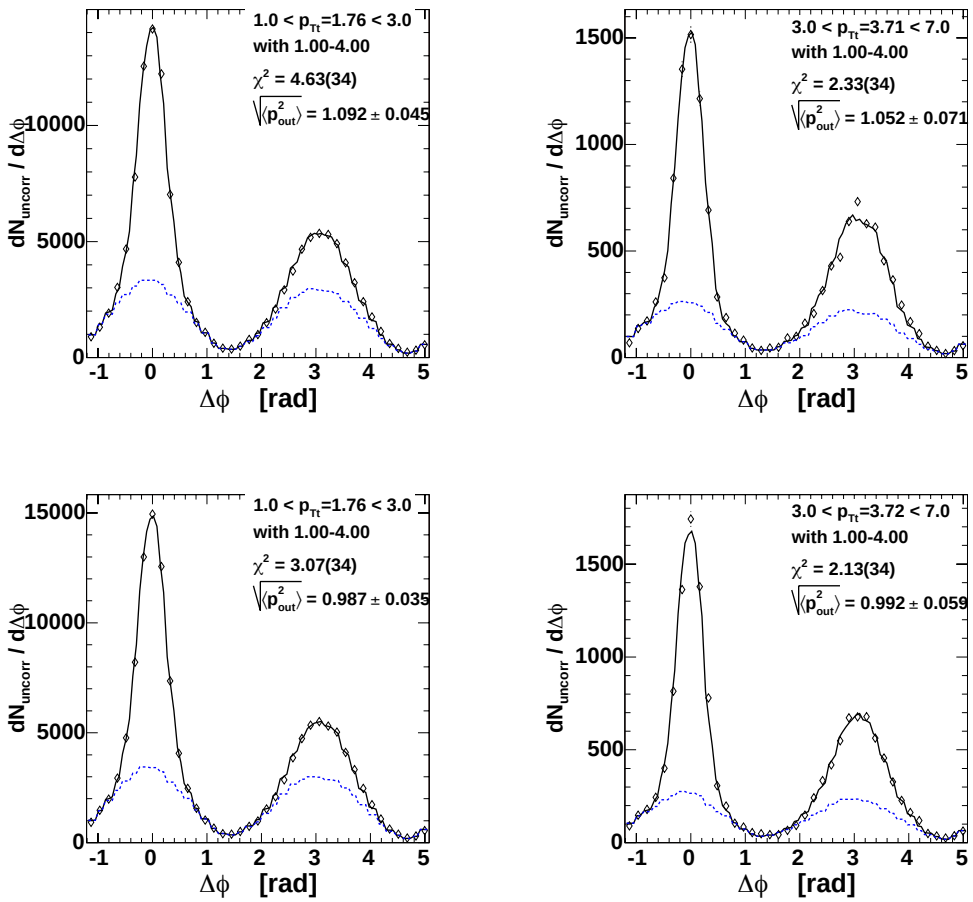

Figure 6.1: Uncorrected Correlation Functions. These functions are the simple π^0-$h^{\pm}$ particle azimuthal correlations (data points). The black lines are the fits to the data given by the formulas derived in Section 4.3. Also shown are the mixed event background (blue lines). In the top row are the parallel event CFs, in the bottom row the anti-parallel event CFs. The left column corresponds to Bin 1 events and the right row to Bin 2 events.

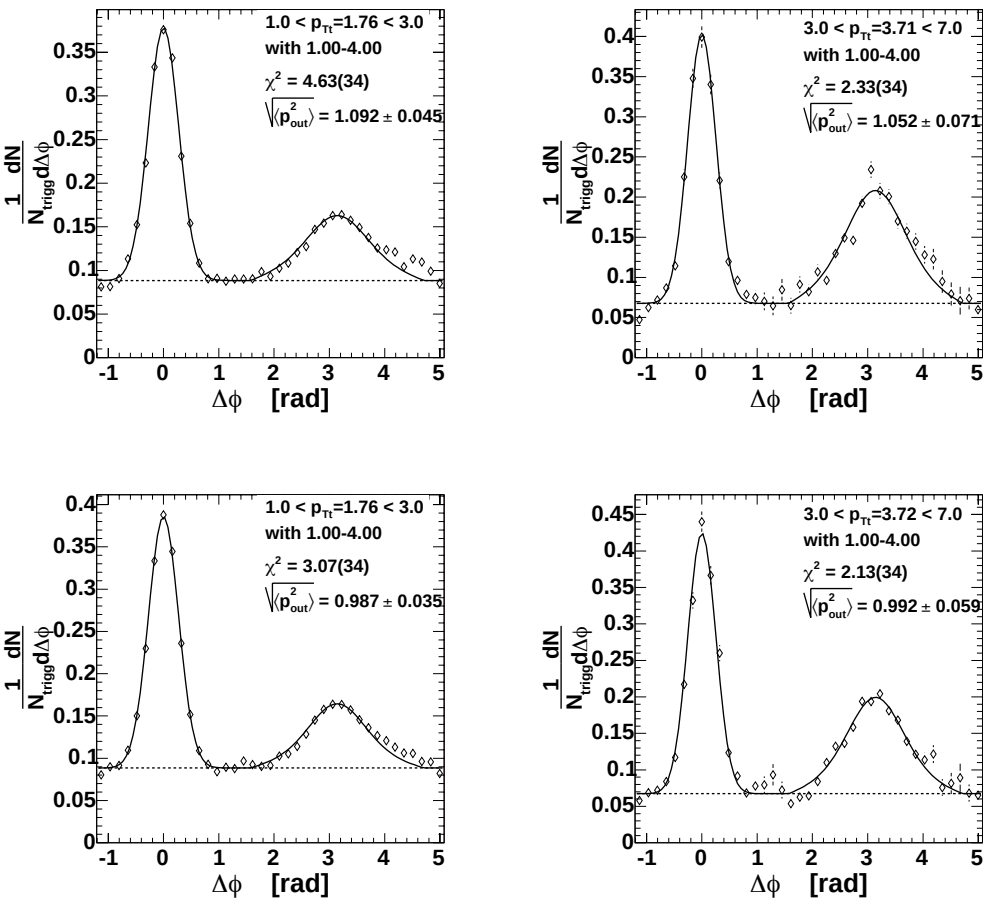

Figure 6.2: Corrected Correlation Functions. The graphs are in the same order as in Fig. 6.1. Here the background has been divided out and the remaining functions are fit to a constant plus two Gaussians, one for the near side peak and one for the away side peak.

6.2 Extracted Results

Using the CFs, j_T is extracted from the width of the near side peak (σ_N), and p_{out} is taken from the fit to the far side peak, from which we deduce $x_h^{-1} \langle z_t \rangle \sqrt{\langle k_T^2 \rangle}$ and $\langle z_t \rangle \sqrt{\langle k_T^2 \rangle}$. The results for the 2-bin analysis are shown in Fig. 6.3 and Fig. 6.4.

Red square points are results for parallel helicity events, blue triangles are results for anti-parallel helicity events. The figures where only black points are given (Fig. 6.4) represent the difference in the values for the two different helicity configurations. The top row of Fig. 6.3 shows σ_N and the extracted value j_T. The bottom row shows p_{out} and the derived quantity $x_h^{-1} \langle z_t \rangle \sqrt{\langle k_T^2 \rangle}$. Fig. 6.4 shows the difference for $x_h^{-1} \langle z_t \rangle \sqrt{\langle k_T^2 \rangle}$and $\sqrt{\langle k_T^2 \rangle \langle z_t \rangle^2}$. The dashed vertical line in these plots represents the error-weighted average difference value. The values obtained in Fig. 6.4 are given in Table 6.3.

difference	Bin 1	Bin 2	weighted average
$x_h^{-1} \langle z_t \rangle \sqrt{\langle k_T^2 \rangle}$	(130 ± 69) MeV/c	(153 ± 230) MeV/c	(132 ± 66) MeV/c
$\langle z_t \rangle \sqrt{\langle k_T^2 \rangle}$	(114 ± 62) MeV/c	(64 ± 101) MeV/c	(100 ± 53) MeV/c

Table 6.3: Results of the $x_h^{-1} \langle z_t \rangle \sqrt{\langle k_T^2 \rangle}$ and $\langle z_t \rangle \sqrt{\langle k_T^2 \rangle}$ differences for the two-bin analysis.

The formula used for calculating the error-weighted average $\bar{x}$ is:

$$\bar{x} = \frac{\sum_i \frac{x_i}{(\delta x_i)^2}}{\sum_i \frac{1}{(\delta x_i)^2}} \tag{6.1}$$

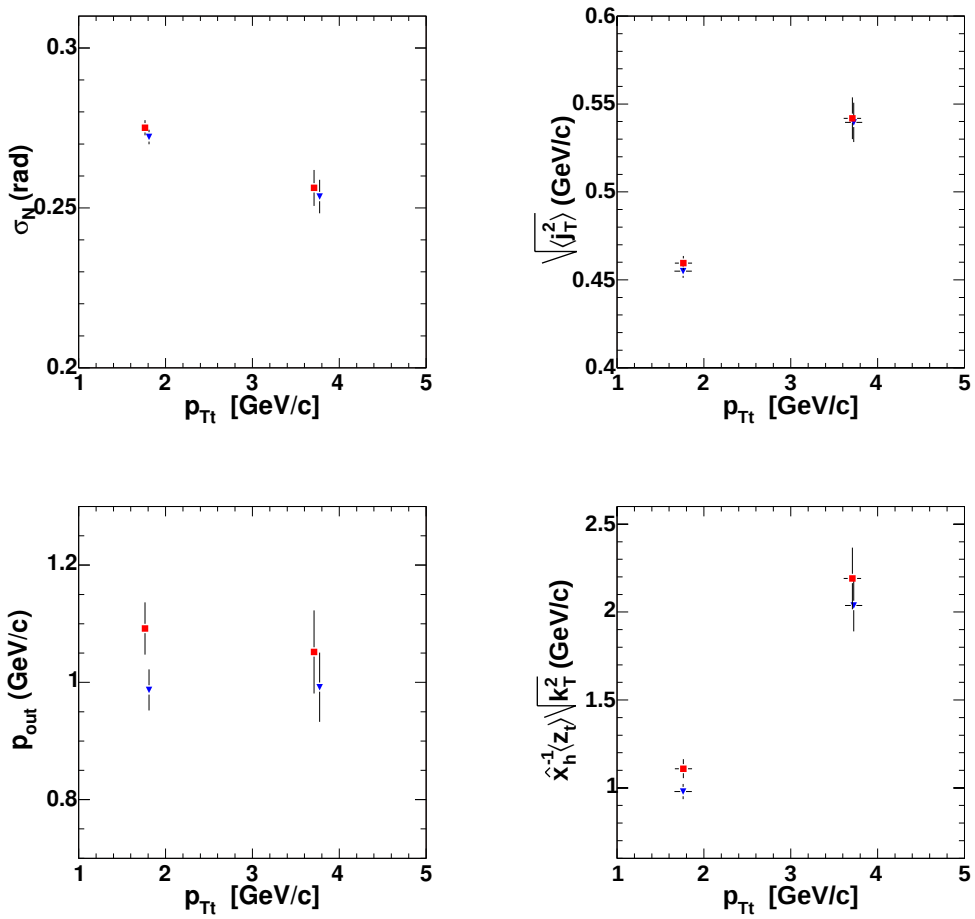

Figure 6.3: 2-Bin analysis results. *(top)* shows σ_N and the extracted value j_T. *(bottom)* shows p_{out} and the derived quantity $x_h^{-1} \langle z_t \rangle \sqrt{\langle k_T^2 \rangle}$. In all four graphs red square points are results for parallel helicity events and blue triangles are results for anti-parallel helicity events.

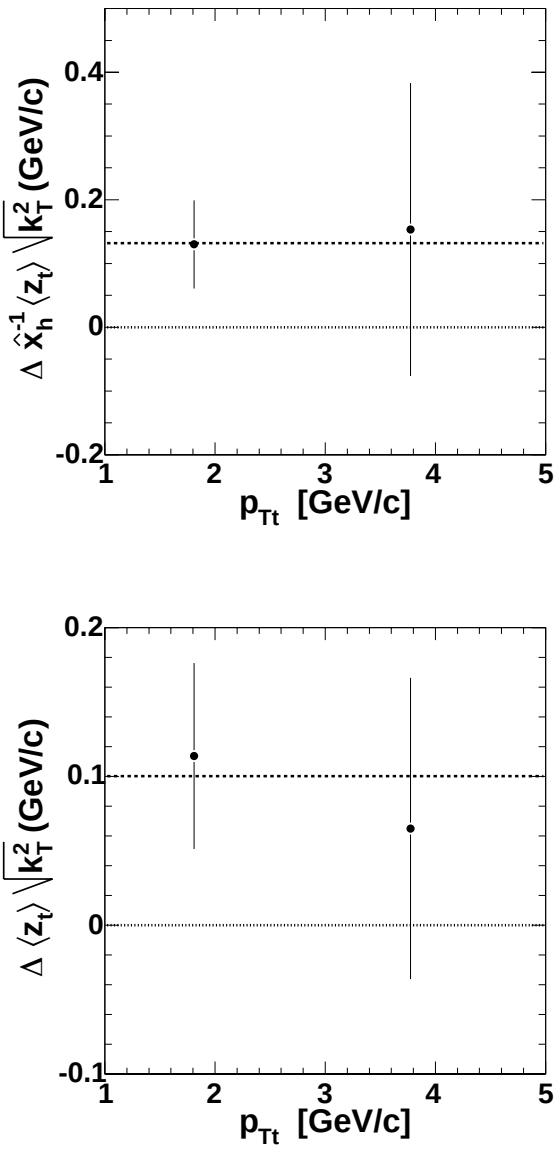

Figure 6.4: 2-Bin analysis difference results. *(top)* shows the $x_h^{-1}\,\langle z_t\rangle\,\sqrt{\langle k_T^2\rangle}$ difference between parallel and anti-parallel helicity events. *(bottom)* shows the $\langle z_t\rangle\,\sqrt{\langle k_T^2\rangle}$ difference between parallel and anti-parallel helicity events. The dashed non-zero horizontal lines represent the error-weighted average value for the two bins given by Eq. (6.1).

The error $\delta\bar{x}$ associated with this weighted average is given by:

$$\frac{1}{\delta\bar{x}} = \frac{1}{(\delta x_i)^2} \tag{6.2}$$

The error bars are mostly statistical in nature, but they do also stem from the accuracy of the fit, as the χ^2 of the Correlation Function fits are taken into account.

6.3 Binning

Another analysis using smaller bins was made, and the results are shown in Fig. 6.5, Fig. 6.6 and Table 6.4 with the same conventions regarding color, graph placement and the significance of the dashed vertical lines as in Section 6.2. The $p_{T\mathrm{a}}$ range is the same as previously, but the $p_{T\mathrm{t}}$ bins are now narrower (0.5 GeV/c wide for $p_{T\mathrm{t}}$ less than 3 GeV/c, and 1 GeV/c wide for $p_{T\mathrm{t}}$ greater than 3 GeV/c.)

difference	weighted average
$x_h^{-1}\langle z_t\rangle\sqrt{\langle k_T^2\rangle}$	(102 ± 59) MeV/c
$\langle z_t\rangle\sqrt{\langle k_T^2\rangle}$	(96 ± 50) MeV/c

Table 6.4: Results of the $x_h^{-1}\langle z_t\rangle\sqrt{\langle k_T^2\rangle}$ and $\langle z_t\rangle\sqrt{\langle k_T^2\rangle}$ differences for the multi-bin analysis.

The error-weighted averages for the two different binning analyses are compatible and non-zero.

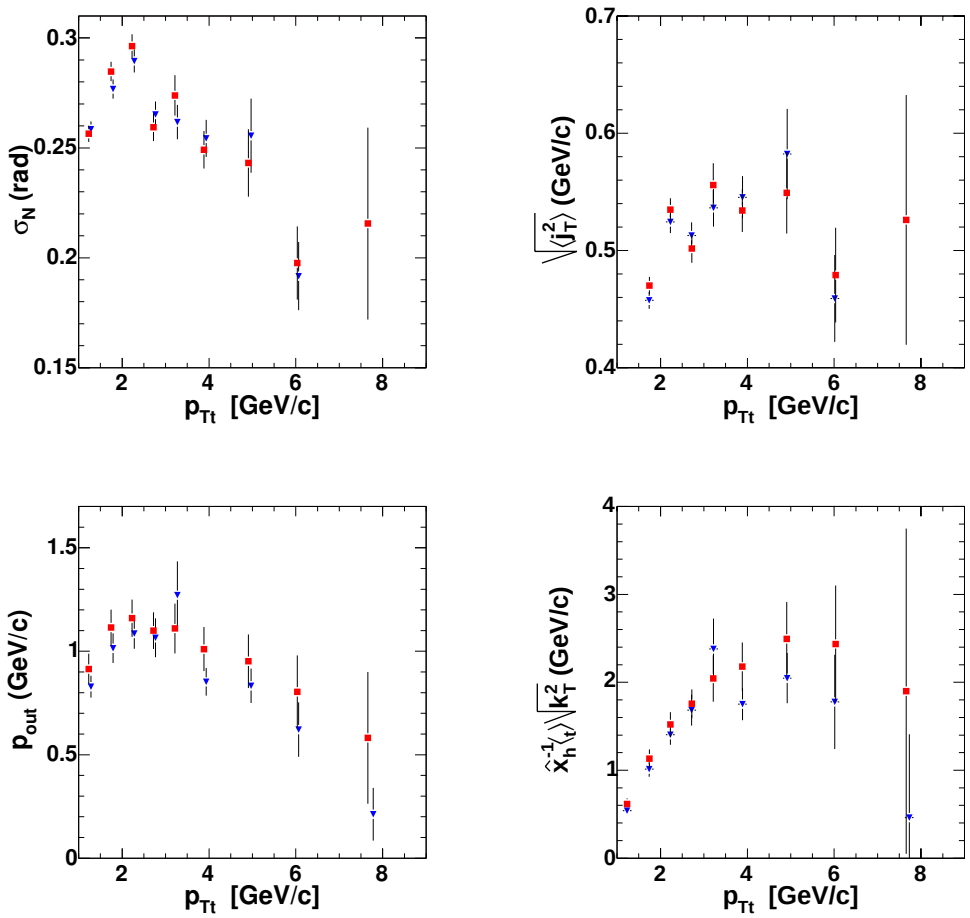

Figure 6.5: Multi-bin analysis results. *(top)* shows σ_N and the extracted value j_T. *(bottom)* shows p_{out} and the derived quantity $x_h^{-1} \langle z_t \rangle \sqrt{\langle k_T^2 \rangle}$. In all four graphs red square points are results for parallel helicity events and blue triangles are results for anti-parallel helicity events.

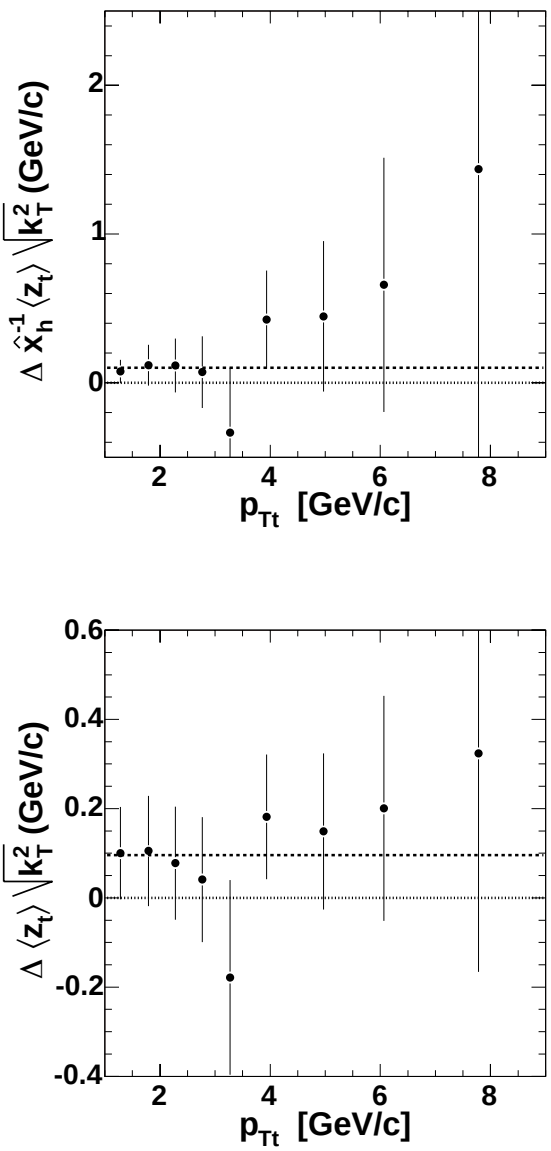

Figure 6.6: Multi-bin analysis difference results. *(top)* shows the $x_h^{-1}\,\langle z_t\rangle\,\sqrt{\langle k_T^2\rangle}$ difference between parallel and anti-parallel helicity events. *(bottom)* shows the $\langle z_t\rangle\,\sqrt{\langle k_T^2\rangle}$ difference between parallel and anti-parallel helicity events. The dashed non-zero vertical lines represent the error-weighted average value for all the bins.

6.4 Combined Event Comparison

A first check of our results is to look at the σ_N, j_T, p_{out}, and $x_h^{-1} \langle z_t \rangle \sqrt{\langle k_T^2 \rangle}$ values for all events, both parallel and anti-parallel helicity event and compare them with the spin-sorted data. We should find values for this data set situated between the parallel and anti-parallel helicity data sets. Fig. 6.7 shows these results, where:

- red squares: same helicity
- blue triangles: opposite helicity
- black dots: both helicity sets

We see that the combined event value is almost always located between the parallel helicity event and the anti-parallel helicity event results. Taking error bars into consideration, the combined event results are always consistent with an intermediate value between the two event sets.

6.5 Bunch Shuffling

In order to understand the nature of our errors, Bunch Shuffling was done. The method of bunch shuffling consists of assigning a random spin orientation to each bunch crossing for each run analyzed and then conducting the analysis using the fake parallel, anti-parallel helicity configurations. The difference in $x_h^{-1} \langle z_t \rangle \sqrt{\langle k_T^2 \rangle}$ and $\langle z_t \rangle \sqrt{\langle k_T^2 \rangle}$ values for the two randomly determined data sets are calculated. This is done a number of times in order to determine the stability of the fit results for the real different helicity data sets. A relatively large number of iterations is necessary, because the randomization is not done on an event-per-event basis but only on a total of good spin configuration bunch crossings ~ 50 per run.

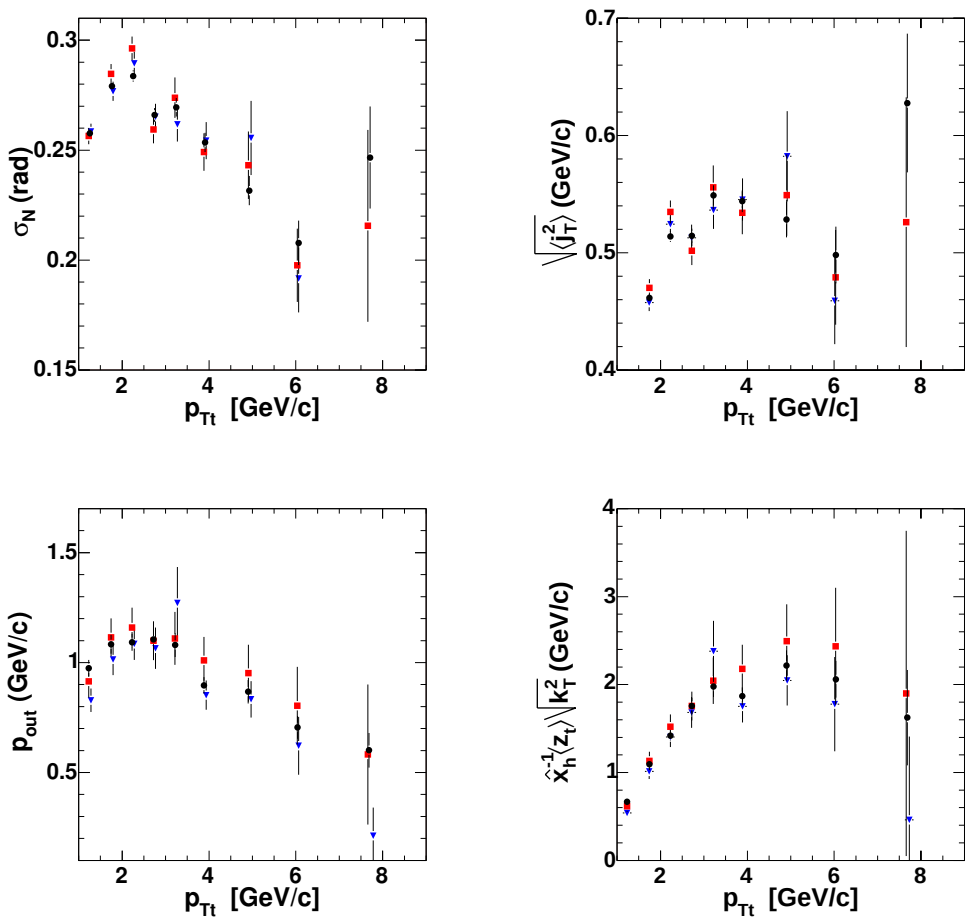

Figure 6.7: Combined helicity analysis results. *(top)* shows σ_N and the extracted value j_T. *(bottom)* shows p_{out} and the derived quantity $x_h^{-1} \langle z_t \rangle \sqrt{\langle k_T^2 \rangle}$. The black dots reresent the quantities calculated or derived for events from both helicity states.

A total of 250 bunch shuffles were run using the same $p_{T\mathrm{t}}$ and $p_{T\mathrm{a}}$ bins as in the 2-Bin analysis. The results are given in Fig. 6.8, which shows the spread for the $x_h^{-1}\langle z_t\rangle\sqrt{\langle k_T^2\rangle}$ difference in the first row and for the $\langle z_t\rangle\sqrt{\langle k_T^2\rangle}$ difference in the second row. The columns correspond to the bins used in Table 6.1. The x-axis is in units of GeV/c. The averages for all graphs are ~ 0, and the RMS values are given in the Table 6.5.

difference	Bin 1	Bin 2
$\Delta\left(x_h^{-1}\langle z_t\rangle\sqrt{\langle k_T^2\rangle}\right)$	(0.0 ± 73) MeV/c	(-1.2 ± 197) MeV/c
$\Delta\left(\langle z_t\rangle\sqrt{\langle k_T^2\rangle}\right)$	(0.4 ± 62) MeV/c	(4 ± 81) MeV/c

Table 6.5: Bunch Shuffling results. Two bins were used, with the same $p_{T\mathrm{t}}$ and $p_{T\mathrm{a}}$ values as for the 2-Bin analysis.

The results of interest, the RMS value of $\Delta\left(x_h^{-1}\langle z_t\rangle\sqrt{\langle k_T^2\rangle}\right)$ and $\Delta\left(\langle z_t\rangle\sqrt{\langle k_T^2\rangle}\right)$ give an indication of statistical uncertainty and compares favorably with the error bars in Fig. 6.4, and the difference should give an order of the residual systematic uncertainty. The values are compared in Table 6.6, which show that the systematic errors appear to be negligeable. If anything, we have overestimated the values of our error bars. Moreover, the fact that the mean is ≈ 0 for all cases reflects well on the method used.

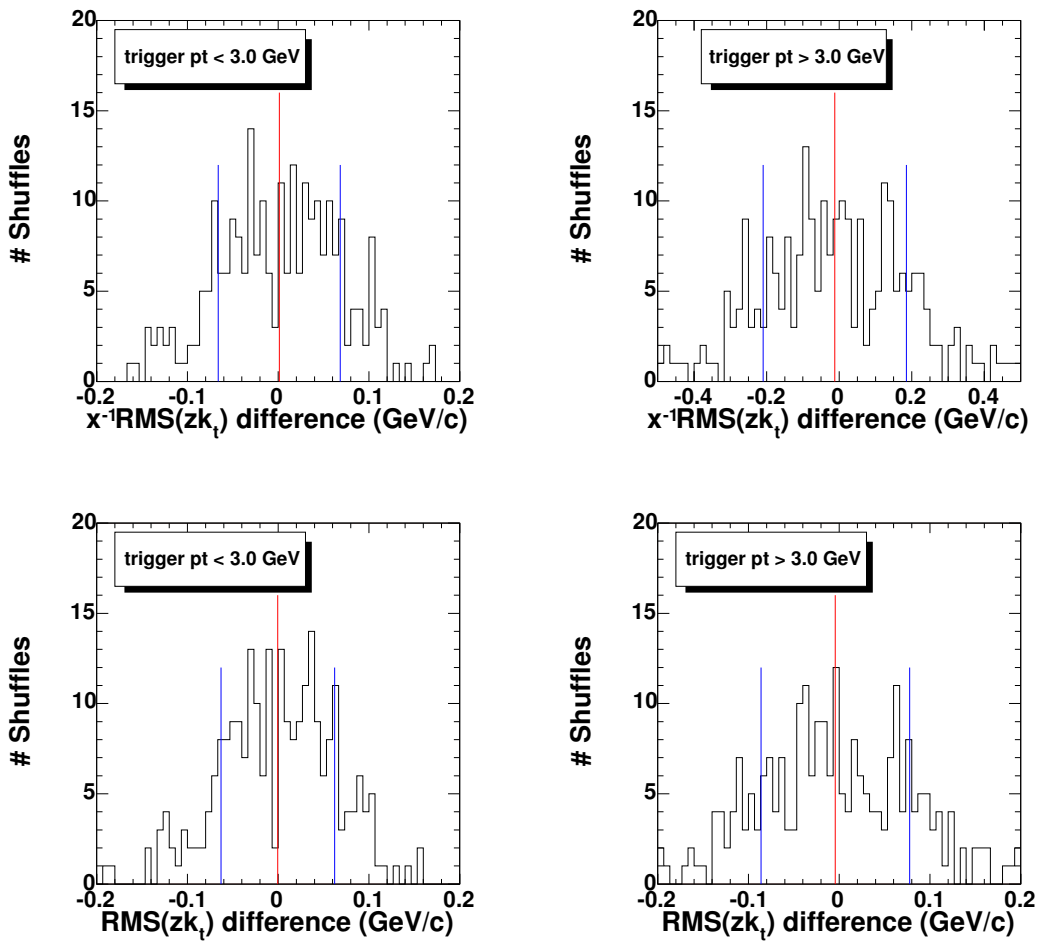

Figure 6.8: Bunch Shuffling.*(top)* shows the $\Delta\left(x_h^{-1}\left\langle z_t\right\rangle\sqrt{\left\langle k_T^2\right\rangle}\right)$ spread for the different randomly assigned helicity sets and *(bottom)* shows the $\Delta\left(\left\langle z_t\right\rangle\sqrt{\left\langle k_T^2\right\rangle}\right)$ distribution for the different randomly assigned helicity set shuffles. The red line represents the average, and the blue lines show the RMS values of the distributions.

$\Delta\left(\langle z_t\rangle\sqrt{\langle k_T^2\rangle}\right)$ comparison	Bunch Shuffling RMS	data error	difference
bin 1	62 MeV	62 MeV	0 MeV
bin 2	81 MeV	101 MeV	- MeV

Table 6.6: Error comparison. The $\Delta\left(\langle z_t\rangle\sqrt{\langle k_T^2\rangle}\right)$ errors are shown from the results and compared to the variance of the bunch shuffling distribution.

6.6 Pseudo-Centrality Sorted Results

The question of centrality of the events should not be neglected. Even if in theory a non-zero result arises from the integrated cross-section, we should not asume in the absence of any centrality binning that we collect events from all centrality ranges. It may well be that the conditions of our analysis place us in a specific centrality range.

As a very fist attempt to explore the possibility of centrality dependence, we have looked at results as a function of BBC multiplicity. BBC multiplicity is defined as the number of hits in the North BBC plus the number of hits in the South BBC. We remind the reader that the BBCs are detectors located in the forward rapidity regions ($3.1 < |\eta| < 3.9$), both North and South, and have full azimuthal coverage. They are a natural candidate for centrality studies as they are used to determine centrality for *Au+Au* collisions in conjunction with the ZDCs. The ZDCs show little, if any, hits on an event-per-event basis and thus are of little use here. A look at the BBC multiplicity distribution in Fig. 6.9 shows the cuts on the different BBC bins. The results for $\Delta x_h^{-1}\langle z_t\rangle\sqrt{\langle k_T^2\rangle}$ calculated for the different bins are given in Table 6.7 and shown in Fig. 6.10. The same $p_{T\mathrm{t}}$ and $p_{T\mathrm{a}}$ bins are used as in the multi-bin analysis,

but with a lower cut-off dictated by fewer statistics.

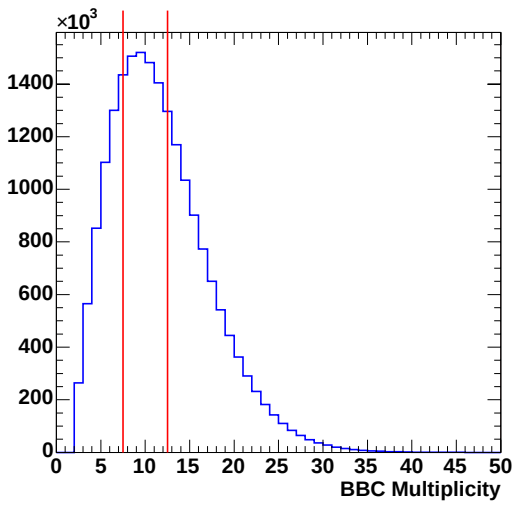

Figure 6.9: BBC multiplicity. The red lines show the delineation for the different bins. The bins have been chosen so as to contain an approximately equal number of events.

	$\Delta\left(x_h^{-1}\langle z_t\rangle\sqrt{\langle k_T^2\rangle}\right)$	$\Delta\left(\langle z_t\rangle\sqrt{\langle k_T^2\rangle}\right)$
low bbc	(136 ± 105) MeV/c	(100 ± 86) MeV/c
mid bbc	(133 ± 91) MeV/c	(125 ± 78) MeV/c
high bbc	(-44 ± 102) MeV/c	(-45 ± 77) MeV/c

Table 6.7: Centrality sorting. The values given are the error-weighted average over the bins shown in Fig. 6.9.

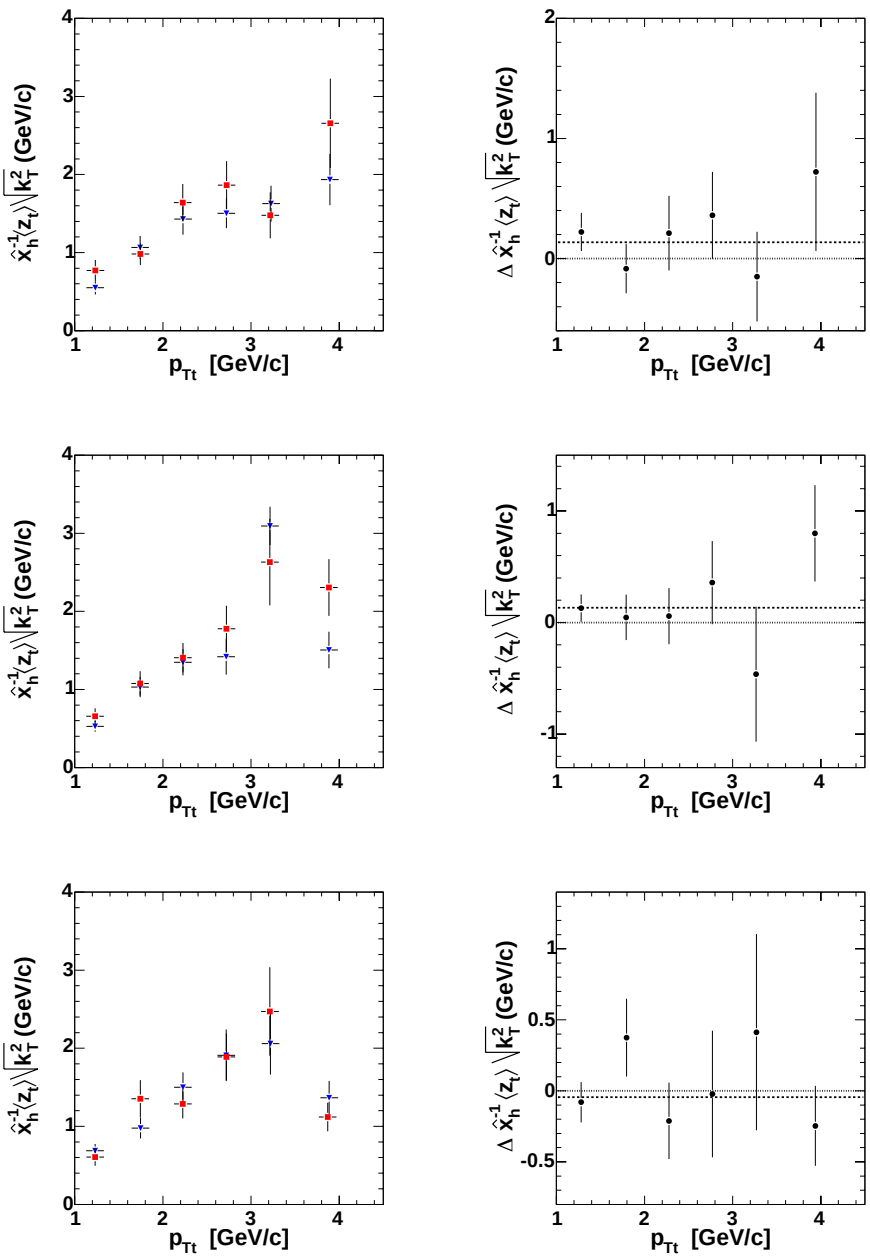

Figure 6.10: BBC multiplicity results. The extracted value $x_h^{-1}\,\langle z_t\rangle\,\sqrt{\langle k_T^2\rangle}$ for parallel and anti-parallel helicity events is given in the left column. In the right column the difference in those values is given. *(top)* BBC mult < 8. *(middle)* $8 \leq$ BBC mult ≤ 12. *(bottom)* mult > 12.

The results from BBC multiplicity binning are promising in that the high bbc bin shows a result distinctive from the other two bins; a result that corresponds to the naïve expectation of greater particle production associated with a higher centrality and a negative $\Delta\sqrt{\langle k_T^2 \rangle}$. Unfortunately, the error bars are still too large to exclude statistical fluctuations.

Chapter 7

Monte Carlo

7.1 Introduction

In this section we describe a simple Monte Carlo to determine the sensitivity of our method described in Chapter 4 to POAM. With a few simple models, we would like to test the robustness of the assumption of a net k_T effect with orbital motion and no impact parameter determination.

The Monte Carlo will make use of the event generator PYTHIA, which simulates p+p collisions by using measured cross-sections to calculate probable interactions and fragmentation into hadrons. One of the parameters PYTHIA takes is the amount of k_T for the interacting partons. We will use simple models to determine the amount of k_T to enter into PYTHIA to simulate parallel and anti-parallel $\vec{k}_{T\text{pair}}$ effects, then compare the extracted values $\sqrt{\langle j_T^2 \rangle}$ and $\langle z_t \rangle \sqrt{\langle k_T^2 \rangle}$ for each simulation.

Since little is known about the parton transverse position or momentum distribution, several rather naïve assumptions are made in order to model the collisions. We first assume constant angular velocity of partons, p_θ, regardless of distance to

the proton center. We set (arbitrarily) the maximum transverse momentum of the partons to be 300 MeV/c at the radius of the proton we consider to be to 1.3 fm.

Here we are only considering the motion associated with orbital angular momentum. Real motion of course includes random motion in the transverse plane by the partons, due at the minimum to the Heisenberg Uncertainty principle (see Section 2.2). Also, this model is very much a classical rather than a quantum model. In a second phase of MC we will need to consider that the partons will have integer angular momenta $l = 0, 1, ...$ and make models on the radial distribution as a function of l. Indeed, the only object of this first Monte Carlo is to calculate the p_T kick (equivalent to the $\vec{k}_{T\text{pair}}$ from Chapter 4 and shown in Fig. 7.1) due to orbital angular momentum, and see if different helicity events will produce measurably different results.

Fig. 2.3 demonstrates the mechanism of "amplification" (peripheral & parallel helicities, or central & anti-parallel helicities) or "attenuation" (peripheral & anti-parallel or central & parallel) of the coherent k_T components, and Fig. 7.1 provides a description of the relevant geometric parameters used in the calculation of the pair transverse momentum $\vec{k}_{T\text{pair}}$, given an impact parameter b, and a parton collision point $\vec{r}_0(x_0, y_0)$.

At large impact parameter, the parallel helicity configuration gives the greater $\vec{k}_{T\text{pair}}$, at small impact parameter it is the anti-parallel helicity collisions. At mid-impact parameter, it depends on where in the interaction area, or "almond" the interaction takes place. It is therefore important to use a model that determines impact parameter and interaction point within the almond.

The probability for a particular collision with a given impact parameter is parametrized, then we integrate over the impact parameter in order to determine the impact parameter averaged parton pair transverse momentum, $\vec{k}_{T\text{pair}}$. For simplicity,

we ignore all incoherent (non-angular momentum correlated) contributions to the parton k_T.

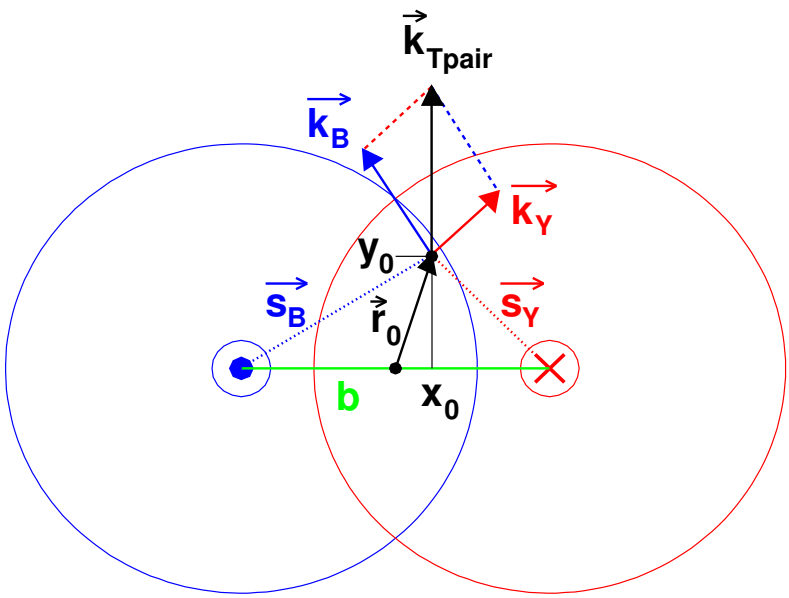

Figure 7.1: $\vec{k}_{T\text{pair}}$ parameters. $\vec{k}_{T\text{pair}}$ is the sum of the $\vec{k}_B$ and $\vec{k}_Y$ vectors. The interaction point has coordinates x_0 and y_0 as measured from the center of the interaction almond. Together they form the vector $\vec{r}_0$.

In theory, if we had a function $P(b)$, the probability of having a collision at impact parameter b, we could randomly determine a value from 0 to 1, extract the impact parameter b, and then calculate the probability of a parton-parton interaction as a function of our impact parameter. In PYTHIA however, we cannot use the impact parameter because physics cross-sections are not calculated as a function of impact parameter. This lies at the heart of a deeper problem, previously mentioned in

Section 1.5.2; namely, that the Parton Distribution Functions are a function of x, not radial distance. Spatial distribution of partons within the proton remains largely conjectural (see Section 2.5), and the resolution of this unknown quantity may in fact be correlated with our study.

We must then use our model to artificially determine an impact parameter and collision point, which will serve only to calculate a distribution of one input parameter: the p_T kick due to orbital angular momentum ($|\vec{k}_{T\text{pair}}|$). The weighting of probabilities is merely used to confirm that with a simple model and reasonable assumptions on orbital angular momentum, this input parameter has a different distribution based on whether the helicities of the colliding protons are parallel or anti-parallel.

7.2 Different Models

7.2.1 Colliding Disks

The first step is to consider that the cross section of two colliding disks of radius R for an impact parameter b is:

$$\sigma = \pi \cdot b^2 \ , \quad \text{for: } b < 2R \tag{7.1}$$

Eq. (7.1) is f_1 of Fig. 7.2. The probability of colliding at impact parameter b is then:

$$P(b) = \frac{\int_0^b \pi r^2 \, dr}{\int_0^{2R} \pi r^2 \, dr} = \left(\frac{b}{2R}\right)^3 \tag{7.2}$$

We only take jet-jet events from PYTHIA, in order to determine whether our analysis is effective in measuring the extra p_T kick we give as input. Every PYTHIA

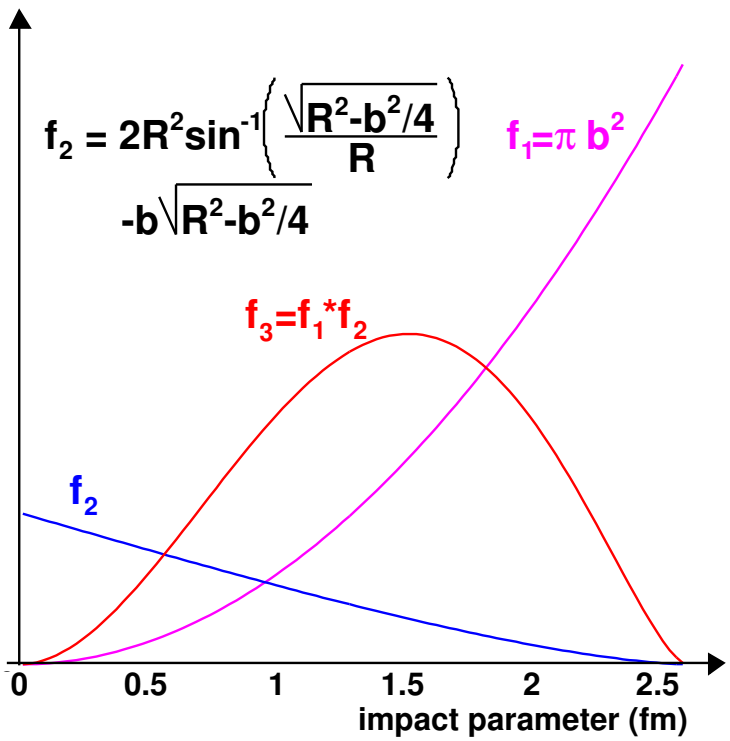

Figure 7.2: Impact parameter probability functions

event is a collision and so our impact parameter probability must be weighted accordingly:

$$P(b) = \frac{\int_0^b \pi r^2 f(r)\, dr}{\int_0^{2R} \pi r^2 f(r)\, dr} \tag{7.3}$$

where $f(r)$ depends on the model used.

For a simple solid disc model $f(r)$ is the surface area of the overlap region, called the "Almond", seen in Fig. 7.3 (top) and Fig. 7.1. The area of the Almond is calculated to be:

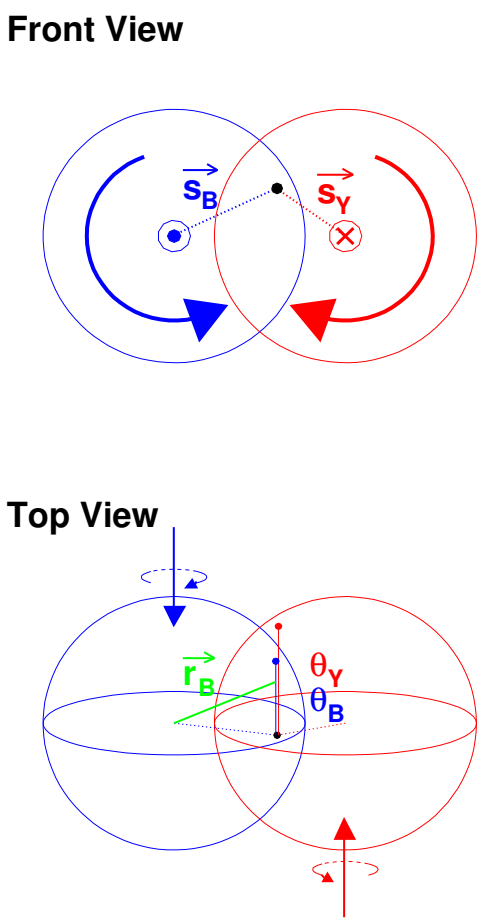

Figure 7.3: Variables and parameters in p+p collisions. *(top)* shows the radial position vectors $\vec{s}_B$ and $\vec{s}_Y$ in the collision plane. *(bottom)* shows the thickness parameters θ_B and θ_Y, which can be either the volume thickness or the Woods-Saxon density distribution. Note in the 3-dimensional case of the Woods-Saxon density depends on $\vec{r}_{B,Y}$ and not $\vec{s}_{B,Y}$.

$$A(b) = 2R^2 \sin^{-1}\left(\frac{\sqrt{R^2 - b^2/4}}{R}\right) - b\sqrt{R^2 - b^2/4} \tag{7.4}$$

Eq. (7.4) is f_2 of Fig. 7.2.

The product of the area and the cross-section gives a reasonable first order probability distribution for the impact parameter. Eq. (7.2) now becomes:

$$P(b) = \frac{\int_0^b A(r) \cdot \pi r^2 \, dr}{\int_0^{2R} A(r) \cdot \pi r^2 \, dr} \tag{7.5}$$

Unlike Eq. (7.2), extracting b from this equation, having randomly determined $P(b)$ becomes problematic, so the denominator in Eq. (7.5) is approximated numerically and we determine the impact parameter by binning. The interaction point is then randomly determined within the almond area. Fig. 7.4 shows the spacial distribution of randomly determined interaction points for a) fixed impact parameter $b = 1fm$, and b) probability-determined distribution.

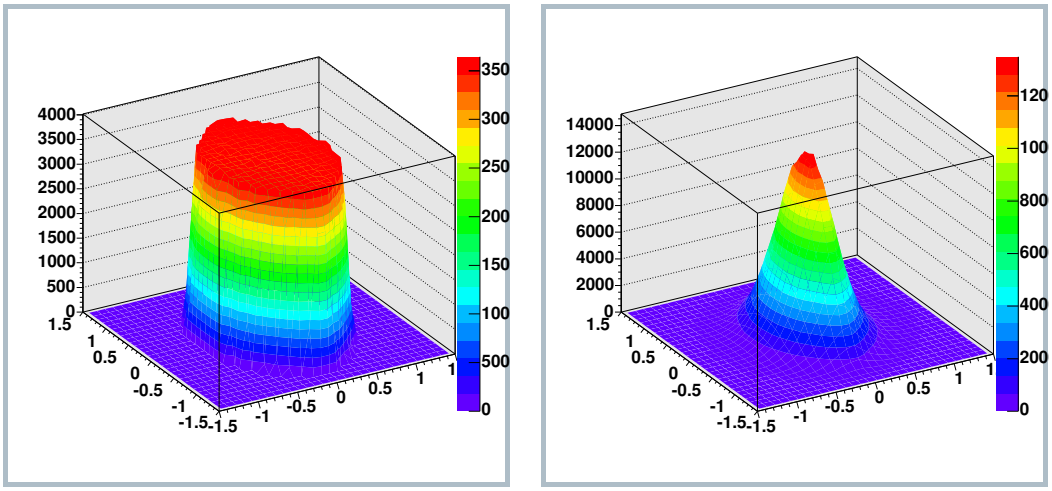

Figure 7.4: Monte Carlo interaction point distributions. In both graphs, the x and y axes correspond to the x_0 and y_0 coordinates of the interaction. *(left)* shows the interaction point distribution for a fixed impact parameter in the solid disk model. All locations within the interaction Almond are equally probable. *(right)* The impact parameter for each collision is weighted. The most likely collision point is centered at (0,0) because it is the region available to all impact parameters. The smaller the impact parameter, the larger the interaction Almond, and the greater the interaction point possibilities.

7.2.2 3D Model

A better model incorporates the thickness of the two protons as shown in (bottom) of Fig. 7.3. The thickness of the proton at a distance s from the center is given by:

$$\theta(s) = 2\sqrt{R^2 - s^2} \tag{7.6}$$

Fig. 7.5 shows the overlap of two protons for impact parameters $b = 1fm$ and $b = 2fm$.

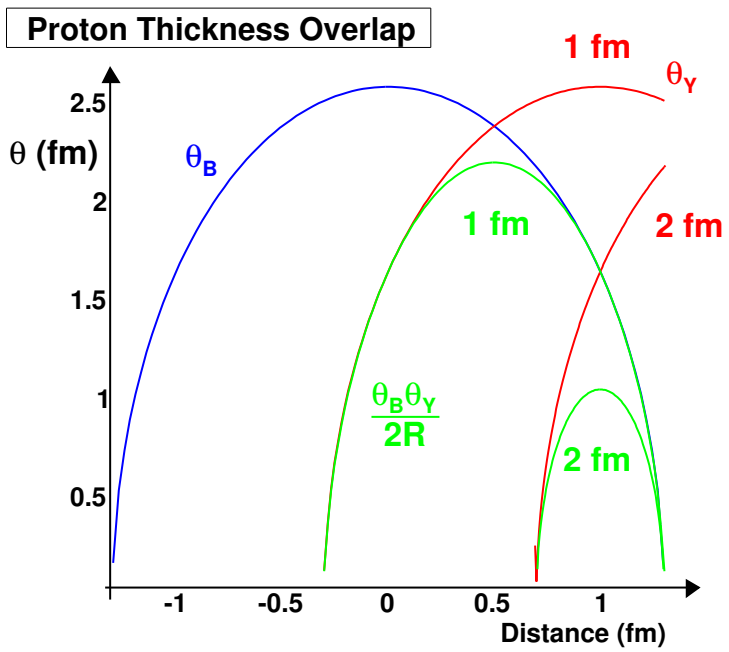

Figure 7.5: Proton thickness overlap. The blue line shows the thickness of the blue beam proton. The red lines show the thickness of the yellow beam proton for different impact parameters ($b = 1fm$ and $b = 2fm$). Both of these are given as a function of distance from the blue proton center of mass. The green lines show the product of the blue and yellow thickness functions (divided by twice the proton radius)

By integrating the thickness of both the blue and yellow protons over all x and y within the Almond surface, we obtain a impact parameter probablility distribution for a solid sphere:

$$f(r) = \int\int \theta_B \cdot \theta_Y \, dx \, dy \mid x, y \in A(r) \tag{7.7}$$

where θ_B and θ_Y are given by Eq. (7.6) and are shown in Fig. 7.5.

7.2.3 Woods-Saxon Potential

To make the model more realistic we add the Woods-Saxon density distribution calculated at each point along the z direction (θ_B, θ_Y) shown in Fig. 7.3 (bottom). The Woods-Saxon potential depends on certain parameters, and two examples of density distributions are shown in Fig. 7.6, and are given by:

$$\rho(r) = \frac{\rho_0}{1 + e^{\frac{r-R}{a}}} \tag{7.8}$$

where ρ_0 is the maximum parton density 0.17 fm^{-1}, R is the proton radius 1.3 fm, and a is the thickness parameter.

The choice of the Woods-Saxon potential is somewhat arbitrary, as the real density distribution is unknown. The particular choice of the skin thickness values a reflects a desire to approximate the partonic radial distribution, considering the lack of quantitative measurements. The two choices made were:

1. $a = 0.2fm$: As seen in the left figure in Fig. 7.6, the thin skin thickness parameter choice gives a density function similar to the ones used for heavy ions. The proton is saturated in partons at the center, and is a scaled version of the heavier ion.

2. $a = 0.5fm$: In the right figure, the thicker skin thickness parameter shows a more rapidly decreasing density as a function of radius more akin to the charge density of the proton, known to be exponential.

Our $f(r)$ now becomes:

$$f(r) = f(r_B) \cdot f(r_Y) \mid x, y \in A(r) \tag{7.9}$$

$$f(r_B) = \int \theta_B(s_B) \left(\int_0^{\sqrt{R^2 - s_B^2}} \left(1 + e^{\frac{\sqrt{x^2 - r_B^2} - R}{a}} \right)^{-1} dr_B \right) ds_B \tag{7.10}$$

Eq. (7.9) can be written as a product of integrals rather than the integral of a product because the two variables are independent. Since the function is the same for both variables this simplifies the implementation of calculating the impact parameter which is done by binning in b, x and y, and s_B and s_Y. The values for s are calculated and stored by binning in z and obtaining the density from the Woods-Saxon formula.

The full model bins the impact parameter from 0 to $2R_{Gl}$, where R_{Gl} is an arbitrary cut-off determined from Fig. 7.6, considering at what distance r the density is negligeable. The cut-off values used are $2.1fm$ for $a = 0.2fm$ and $3.45fm$ for $a = 0.5fm$.

In addition we can consider the 2-Dimensional model with Woods-Saxon potential. Although this model is probably not realistic because it uses only a partonic density imposed on a two dimensional surface, it enables us to check that the density functions are correctly implemented. Moreover it might be considered the limit of a saturation effect normally only associated with larger objects, such as heavy ions. At high momenta, due to the Lorentz contraction, an effect known as the "color glass condensate" appears, which is simply the saturation in the beam direction of the partonic density, which results in a uniform thickness density in the beam direction

at the limit of saturation. The formula is the same as Eq. (7.7) exept instead of the thickness functions $\theta(r)$ we substitute the Woods-Saxon potential Eq. (7.8).

Fig. 7.6 shows the overlap of two proton discs with Woods-Saxon potential density distributions for impact parameters $b = 1$, $b = 2$ and $b = 3$ for two different thickness values.

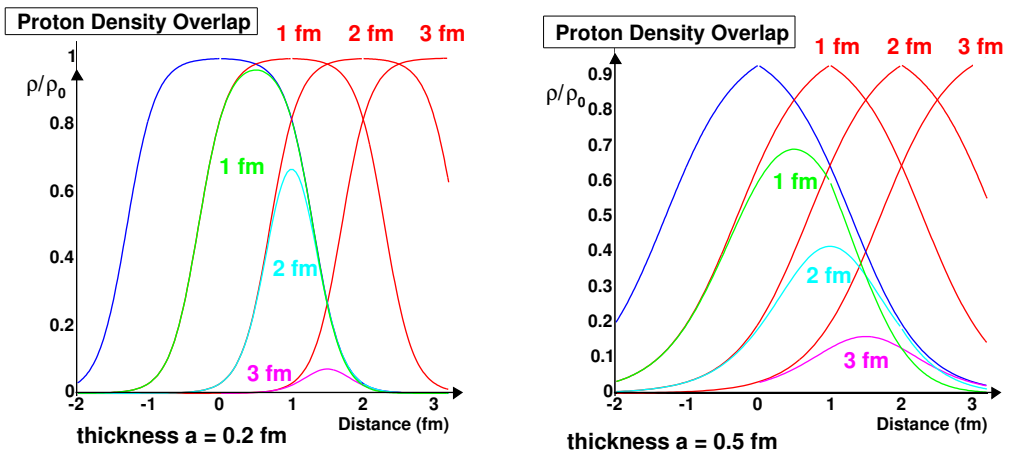

Figure 7.6: Proton Woods-Saxon density overlap. The blue line shows the Woods-Saxon density of the blue beam proton. The red lines show the Woods-Saxon density of the yellow beam proton for different impact parameters ($b = 1fm$, $b = 2fm$ and $b = 3fm$). The green, pink and blue lines show the product of the blue and yellow density functions for *(left)* thickness parameter $a = 0.2fm$ and *(right)* thickness parameter $a = 0.5fm$.

7.3 $\vec{k}_{T\text{pair}}$ Dependencies

Because of the particular assumptions we have made, in particular that the quantity p_θ is constant, some interesting relationships for the parallel and anti-parallel helicity Monte Carlo modeling can be deduced.

From Fig. 7.1 we can calculate the values of the k_T kick ($|\vec{k}_{T\text{pair}}|$) for parallel and anti-paralel helicity collisions.

$$\|\vec{k_T}\| = \sqrt{k_{Tx}^2 + k_{Ty}^2} = \sqrt{(k_{Bx} + k_{Yx})^2 + (k_{By} + k_{Yy})^2} \tag{7.11}$$

The $\vec{k}_{B,Y}$ vectors are related to the $\vec{s}_{B,Y}$ vectors by:

$$\vec{k} = \alpha \begin{pmatrix} \cos\theta & -\sin\theta \\ \sin\theta & \cos\theta \end{pmatrix} \vec{s} \tag{7.12}$$

For an anti-parallel helicity collision θ is 90° for both $\vec{k}_Y$ and $\vec{k}_B$ (the protons are moving in opposite directions); for a parallel helicity collision θ for $\vec{k}_Y$ is -90°. Thus:

$$\begin{cases} \text{parallel:} & \vec{k}_B = \alpha(-s_{By}, s_{Bx}) \quad \vec{k}_Y = \alpha(s_{Yy}, -s_{Yx}) \\ \text{anti-parallel:} & \vec{k}_B = \alpha(-s_{By}, s_{Bx}) \quad \vec{k}_Y = \alpha(-s_{Yy}, s_{Yx}) \end{cases} \tag{7.13}$$

The components of $\vec{s}_B$ and $\vec{s}_Y$ can easily be broken down, using the notations in Fig. 7.1:

$$\vec{s}_B = (\tfrac{b}{2} + x_0, y_0) \quad \vec{s}_Y = (-\tfrac{b}{2} + x_0, y_0) \tag{7.14}$$

Thus Eq. (7.11) becomes:

$$\begin{cases} \text{par:} & \|\vec{k_T}\| = \alpha\sqrt{(-y_0 + y_0)^2 + (\frac{b}{2} + x_0 + \frac{b}{2} - x_0)^2} = \alpha b \\ \\ \text{anti:} & \|\vec{k_T}\| = \alpha\sqrt{(-y_0 - y_0)^2 + (b/2 + x_0 - b/2 + x_)^2} = 2\alpha\|\vec{r_0}\| \end{cases} \tag{7.15}$$

As long as we consider uniform angular rotation, no matter the model, the orbital p_T kick for parallel helicity events will be proportional to the impact parameter, regardless of where the interaction point lies within the interaction almond. For anti-parallel helicity events the orbital p_T kick only depends on the distance of the interaction point from the center of the almond.

7.4 Monte Carlo Results

7.4.1 Modeling Results

The results from the Monte Carlo $|\vec{k}_{T\text{pair}}|$ calculations for the different models are given in Fig. 7.7.

The different $\langle \Delta k_T \rangle$ values for the different models are given in Table 7.1:

Model	$\langle \Delta k_T \rangle$
Solid Disk	96 MeV
Solid Sphere	135 MeV
2D Woods-Saxon, a=0.2	168 MeV
2D Woods-Saxon, a=0.5	196 MeV
3D Woods-Saxon, a=0.2	154 MeV
3D Woods-Saxon, a=0.5	198 MeV

Table 7.1: $\left\langle \vec{k}_{T\text{pair}} \right\rangle$ values for different models

Several things should be noted:

- All models used (including the 2-Dimensional) give an appreciable $\langle \Delta k_T \rangle$, approximately 50% of the maximum k_T value of 300 MeV/c.

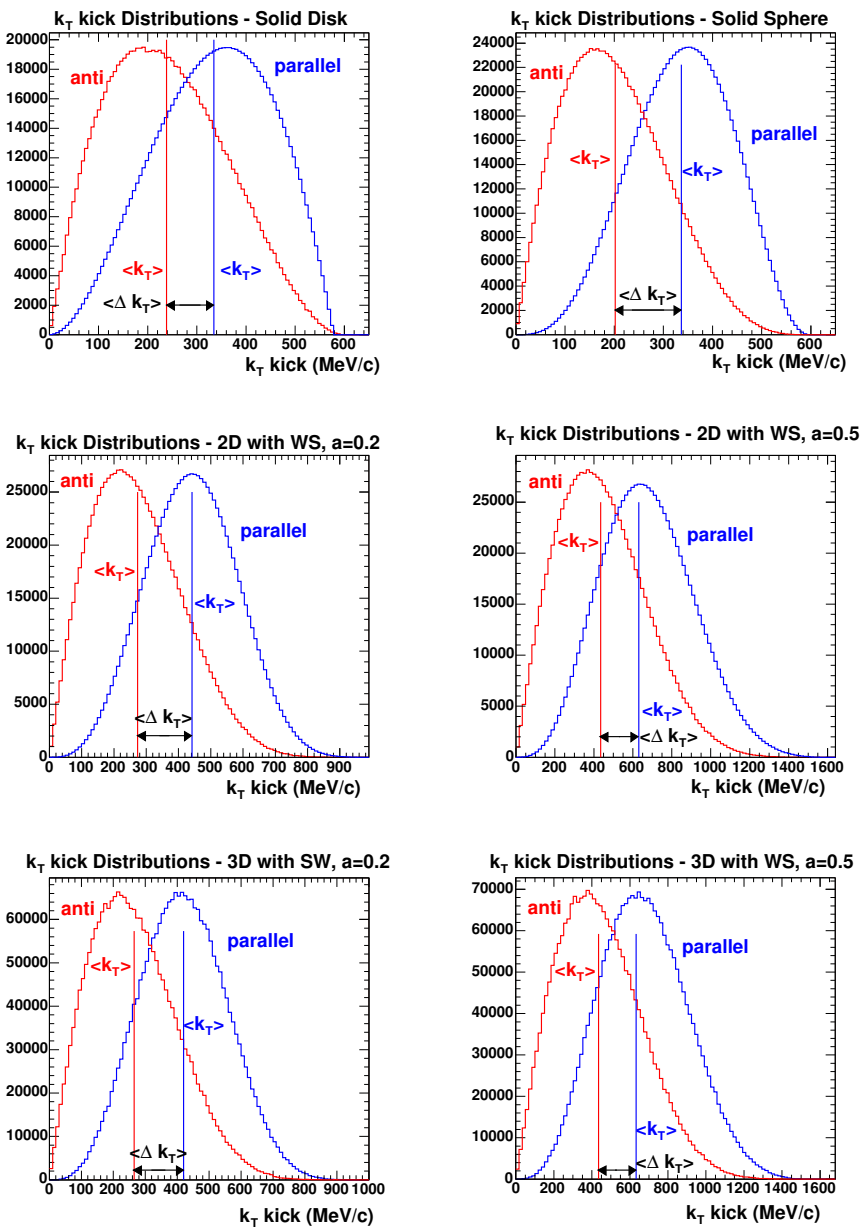

Figure 7.7: Mean $\vec{k}_{T\text{pair}}$ kick calculated for different Monte Carlo models. The blue graphs represent the $|\vec{k}_{T\text{pair}}|$ distributions for the parallel helicity configurations, and the red graphs represent the $|\vec{k}_{T\text{pair}}|$ distributions for the anti-parallel helicity configurations. The vertical lines represent the means of the two distributions and $\langle \Delta k_T \rangle$ the difference in the $\vec{k}_{T\text{pair}}$ means.

- The scale set of 300 MeV/c at $r = 1.3fm$ with constant p_θ is arbitrary.
- It is non-trivial in the extreme to make any extrapolation from result to any particular model used in this simulation study. In no way would any positive result from data confirm or infirm any model used.

Nevertheless, we may conclude that in the framework of a classical model, the hypothesis[19] that if POAM exists, a mean $\sqrt{\langle k_T^2 \rangle}$ difference due to POAM should exist between parallel and anti-parallel helicity events.

7.4.2 Eccentricity

To check that the models used conform to similar experiments, we compare the eccentricity of the models as a function of impact parameter to previous studies done on nucleus-nucleus collisions. We will use the radius of the gold nucleus. The formula for eccentricity is given by:

$$e = \frac{< x^2 - y^2 >}{< x^2 + y^2 >} \tag{7.16}$$

The values for the eccentricity for three models, the simple sphere, and the Woods-Saxon weighted disk and sphere are plotted in Fig. 7.8. The graphs compare favorably to values used in different analyses, exept at large b. The reason for the discrepency is that we use a cut-off limit $R_{Gl} = 8.8fm$ instead of integrating over all space.

Near that cut-off limit we have for $\epsilon = R - b/2$:

$$\lim_{\epsilon \to 0} e = \frac{< \epsilon^2 - \epsilon 2R >}{< \epsilon^2 + \epsilon 2R >} = \frac{2R - \epsilon}{2R + \epsilon} = 1 \tag{7.17}$$

which is the result we see in Fig. 7.8.

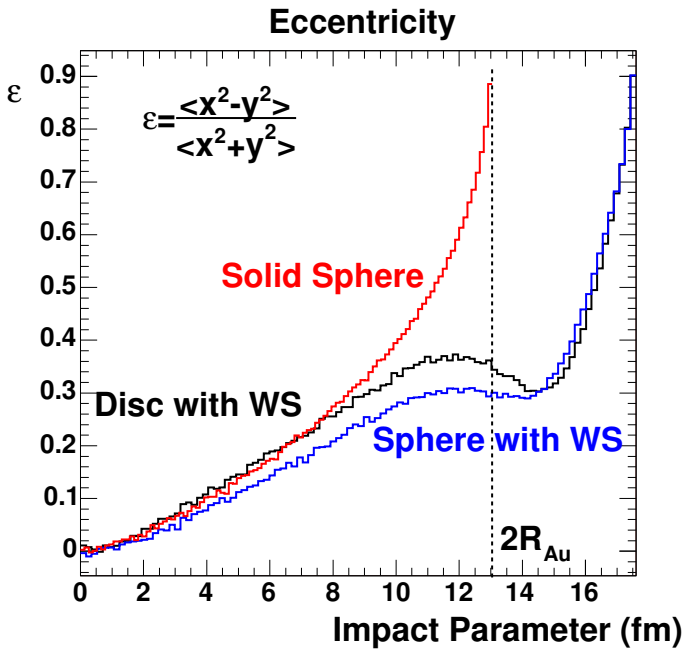

Figure 7.8: *Au+Au* eccentricity

7.4.3 PYTHIA Results

Beyond calculating an eventual effect from modeling, we wish to test our analysis for its sensitivity to such an effect. The analysis code was run on two PYTHIA generated event sets. The first, simulating an anti-parallel helicity event set, had $k_T = 2.5\text{GeV}/c$ as a mean k_T input. The parallel helicity simulated set has $k_T = 2.75\text{GeV}/c$ as a mean k_T input. PYTHIA can only take a mean k_T value and then determines a random k_T on an event-per-event from a Gaussian distribution centered on the mean input value. Giving two different mean values could simulated parallel and anti-parallel data sets fairly well. The distributions shown in Fig. 7.7 are not Gaussian, but they are themselves only guesses based only different models. The results are shown in Fig. 7.9, Fig. 7.10, and Table 7.2.

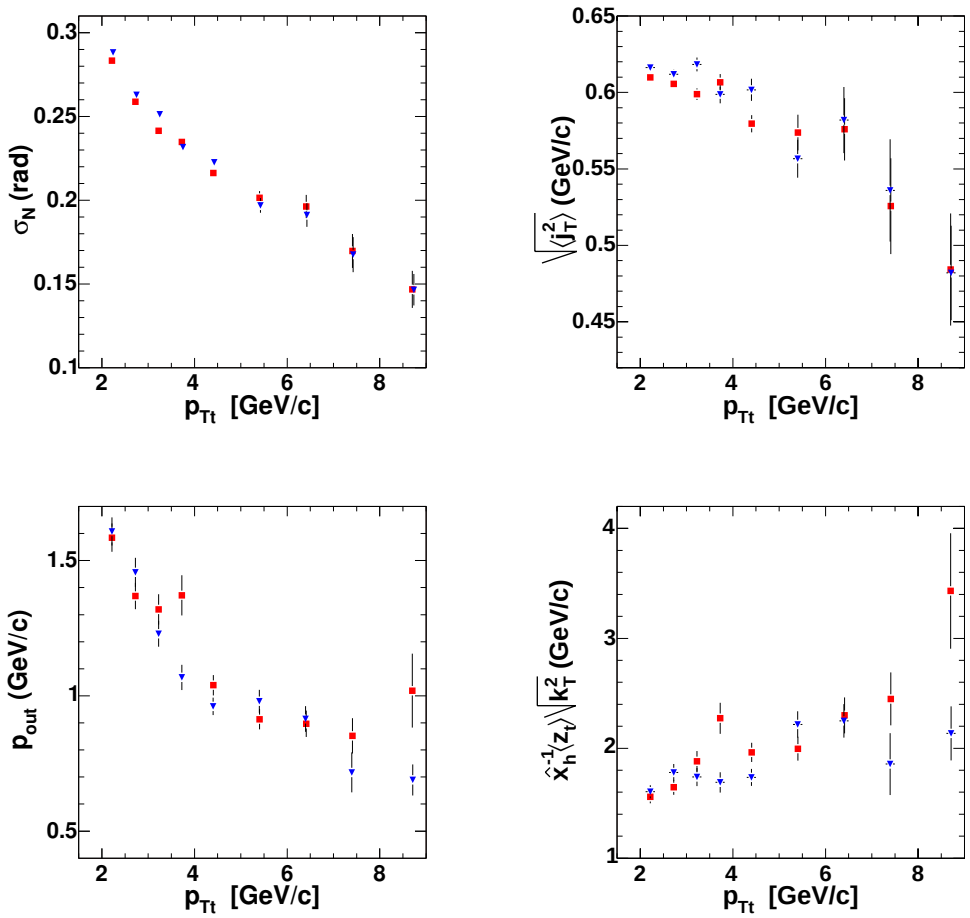

Figure 7.9: PYTHIA MC analysis results. *(top)* shows σ_N and the extracted value j_T. *(bottom)* shows p_{out} and the derived quantity $x_h^{-1} \langle z_t \rangle \sqrt{\langle k_T^2 \rangle}$. In all four graphs red square points are results for $\langle k_T \rangle = 2.75\text{GeV}/c$ (parallel) events and blue triangles are results for $\langle k_T \rangle = 2.5\text{GeV}/c$ (anti-parallel) events.

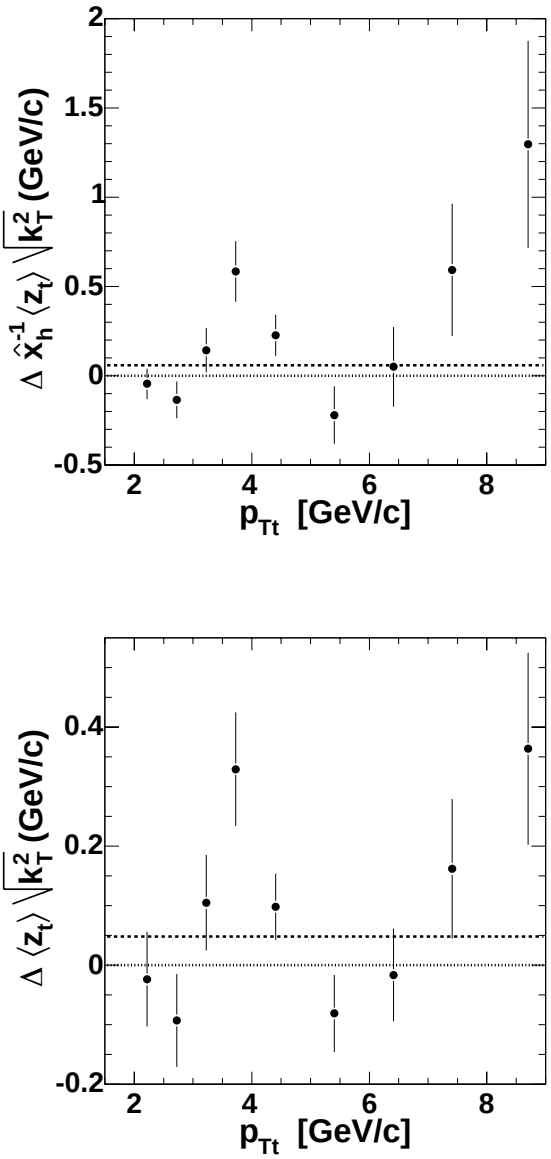

Figure 7.10: PYTHIA MC analysis difference results. *(top)* shows the $x_h^{-1}\,\langle z_t\rangle\,\sqrt{\langle k_T^2\rangle}$ difference between simulated parallel ($\langle k_T\rangle = 2.75\mathrm{GeV}/c$) and anti-parallel helicity ($\langle k_T\rangle = 2.5\mathrm{GeV}/c$) events. *(bottom)* shows the $\langle z_t\rangle\,\sqrt{\langle k_T^2\rangle}$ difference between the two data setsevents. The dashed non-zero horizontal lines represent the error-weighted average value for the bins given by Eq. (6.1).

difference	weighted average
$x_h^{-1} \langle z_t \rangle \sqrt{\langle k_T^2 \rangle}$	(59 ± 49) MeV/c
$\langle z_t \rangle \sqrt{\langle k_T^2 \rangle}$	(48 ± 26) MeV/c

Table 7.2: Results of the $x_h^{-1} \langle z_t \rangle \sqrt{\langle k_T^2 \rangle}$ and $\langle z_t \rangle \sqrt{\langle k_T^2 \rangle}$ differences for the PYTHIA MC analysis.

This analysis on PYTHIA-simulated data indicates that our method and analysis are sensitive to $\sqrt{\langle k_T^2 \rangle}$ differences on the order of 250 MeV/c. The values for $x_h^{-1} \langle z_t \rangle \sqrt{\langle k_T^2 \rangle}$ are not on the same order as the input, and the relation between the two must be understood, although we have not attempted to calculate $\sqrt{\langle k_T^2 \rangle}$ from our data analysis, which can be done using data from ISR[22], which may not be as straightforward as indicated.

Chapter 8

Conclusion

8.1 Conclusions from Results

As a general conclusion, we can say that this analysis has accomplished two things:

- Within the framework of a classical model, the hypothesis by M. Ta-Chung, that if POAM exists, a mean $\sqrt{\langle k_T^2 \rangle}$ difference will also exist betweeen parallel and anti-parallel helicity events.

- The method of two-particle azimuthal correlations for measuring k_T shows promise when applied to the seperate helicity data sets for purposes of measuring the difference between the two sets.

Though limited statistically, the results presented in Chapter 6 bear this statement out. A net effect in the difference between the $\langle z_t \rangle \sqrt{\langle k_T^2 \rangle}$ for parallel and anti-parallel helicity events is measured. The effect is not large; most bin results, although positive, are compatible with zero within their error bars. Several show a

1σ effect. Just as important is to note that within error bars the quantities measured for all events (parallel and anti-parallel helicities combined), fall between the measured quantities for the separated helicity combinations (see Section 6.4).

Certainly these results indicate that with more statistics and better polarization this same method may reach a sensitivity sufficient to see POAM effects. The need for more statistics is obvious since that will reduce the statistical error bars. The advantage of better polarization is that it will enhance the difference between the two event sets.

We have purposefully avoided making any direct claims as to the amount of POAM we are measuring for several reasons:

- Extracting $\sqrt{\langle k_T^2 \rangle}$ from $\langle z_t \rangle \sqrt{\langle k_T^2 \rangle}$ requires some modeling to determine $\langle z_t \rangle$ and increases the error bars. This has been done in the case of non-spin sorted analyses[22] where $\sqrt{\langle k_T^2 \rangle}$ is the desired end. In our case as POAM is the final objective, it presents no real advantage so long as the two next points have not been resolved.

- It is believed that POAM is the main contributor to the asymmetry in the $\sqrt{\langle k_T^2 \rangle}$ for different helicity states, however, it may not be the only contributor, and more theoretical work is needed to determine more precisely how much of the effect can be attributed to POAM.

- Even if if POAM is the only contributor to $\sqrt{\langle k_T^2 \rangle}$ asymmetry, we still have no way to determine POAM quantitatively from $\Delta\sqrt{\langle k_T^2 \rangle}$.

Regardless of how much POAM contributes to the asymmetry in $\sqrt{\langle k_T^2 \rangle}$, the effect is only a fraction of the effect that would be measured if the two beams of protons were completely polarized. In Run3pp the average polarizations were 27% for each

beam, giving us an attenuation factor of:

$$P_B \cdot P_Y \approx .27 \cdot .27 \approx \frac{1}{13.7} \tag{8.1}$$

For polarizations of 50% in both beams for Run5 this would enhance the difference by a factor of 3.5.

Note that we could have shown the results of Fig. 6.4 and Fig. 6.6 augmented by $1/P_B P_Y$ to estimate the difference for complete polarization. We have chosen not to do so for the reasons mentioned above. The error bars would have to be adjusted accordingly and the uncertainty on the polarizations would have to be taken into accunt.

8.1.1 Centrality Determination

The attempt in Section 6.6 to find a correlation with centrality is important although far from conclusive. Until now there has been no possibility of determining centrality with any certainty. While such determination is still unlikely on an event-per-event basis, if POAM does exist and the measured effect is corroborated by more data, by associating lower (even negative) $\sqrt{\langle k_T^2 \rangle}$ asymmetries with lower impact parameters as shown in Fig. 2.3 it may provide a feedback mechanism to work with and compare to other possible centrality measurements. Our understanding of both centrality and POAM may improve iteratively with each result.

Certainly we can see a qualitative and quantitative difference in the results for higher bbc mutiplicity than for the two other bins. The lower, negative values of $x_h^{-1} \langle z_t \rangle \sqrt{\langle k_T^2 \rangle}$ and $\langle z_t \rangle \sqrt{\langle k_T^2 \rangle}$ fit with our naïve expectation of higher centrality and lower impact parameter.

8.1.2 Error Uncertainty

A discussion on the origin and values of the error bars is warranted. In this data set we have shown that the unaccounted errors are small compared with the error bars shown (see Section 6.5), which are statistical in nature, convoluted with the fit error from the Correlation Function. It is not altogether clear that this will continue to be the case as the statistics grow larger. As shown in Eq. (5.3) the error bars on the extracted quantities as well as the fitted quantities depend on the accuracy of the fit. If the hypothesis of two Gaussians plus a constant is not a good one, the error bars will remain undiminished in spite of larger statistics. In order to improve the accuracy of the results a better understanding of the physical causes of deviation from the fit will be necessary.

8.1.3 Simulation

There is much room for more simulation to better understand the interplay between POAM and measured results. The model used in Chapter 7 is a simple classical model. An upgrade to a quantum model, where the interacting parton would have probability determined $L = 0, 1, 2...$ values would make more physical sense.

The introduction of flavor-dependent POAM models is desireable, and would contribute to our understanding. In particular a model with no net L_q would give an estimate of the minimal effect on A_{LL} measurements (see Appendix C).

Another obvious improvement would be to extend the simulation to run through PISA, to verify that detector efficiency doesn't affect the measurement of the asymmetry, and to help understand the origin of non-Gaussian peak features.

8.1.4 General Remarks

Several general remarks can be made regarding the POAM contribution to the proton's spin as it now stands:

- A more synthetic approach to the relationship between the measurement of spin contributions and POAM contributions is necessary (for a specific example of interdependence see Chapter C). All asymmetries must be included in a complete description of the proton including the CNI polarimeter asymmetries as well as the neutron asymmetry used to measure polarization locally at PHENIX. Included in this long term all inclusive iterative process is a characterization of collisions and POAM as a function of impact parameter, presumably by GPDs.

- Originally it seemed that the spin crisis was an ideal opportunity to use the proton to discover more about QCD. As things evolve it seems more likely to be that we are using QCD probes to discover more about the proton. The complex relationships at work mean that many more measurements are required, and in the most broad p_T and rapidity ranges possible.

- The processes that are used currently are mainly from gg or qg interactions. At higher p_T we see a larger qq channel contribution. This is more interesting because we might expect some $\vec{L}_+$ and $\vec{L}_-$ (POAM due to positively charged quarks and negatively charged quarks, respectively; see Section 2.6) even if there is no net POAM. We also expect a correlation between the charge of the associated particle and the flavour of the colliding quark.

- Interestingly, one of the original considerations for the necessity of introducing a new, color, quantum number was the fact that the proton is a stable hadron, in fact, the only stable hadron. It was assumed to be in a ground state and that

its valence quarks must be in a $l = 0$ state and must therefore be differentiated because of Pauli's principle by something other than orbital angular momentum. Of course there are many other solid theoretical and experimental reasons to believe that quarks have color, so a discovery of orbital angular momentum would in no way call into question the fundamental principles of QCD or the existence of color. It could raise interesting questions concerning the the nature of spin: *e.g.* what happens with a spin-3/2 particle? Does the additional spin come from valence quark spin, or from additional orbital angular momentum?

8.2 Future Measurements at RHIC

The RHIC spin program is constantly preparing new venues to explore the mysteries of the proton's spin. Several future projects include:

- Forward calorimeters existing at STAR and being installed in PHENIX will enable A_N in the forward region.
- In the long term, electron cooling will enable increased luminosity to measure Drell-Yan ($q\bar{q} \rightarrow l\bar{l}$)
- Installation of a Silicon Vertex Detector (SVX) at PHENIX will enable secondary displaced vertex resolution for identification of D-mesons and B-mesons as well as W-bosons. This will enable better azimuthal asymmetry measurements because of less fragmentation.

8.2.1 ΔG from $D\bar{D}$

With the installation of a new Silicon Vertex Detector (SVX) an analysis similar to the one described in Appendix B can be done. The near 4π coverage in charged

track detection will enable the identification of secondary vertices, including those corresponding to D-mesons. The distance from the primary to the secondary vertex which correlates to the lifetime of the decaying particle can be measured as well as its position.

An azimuthal correlation between the $D\bar{D}$ pairs will provide a much more accurate estimation of the k_T shift. Moreover the A_{LL} measurement will also improve significantly because of much better decay particle identification, thus improving the signal to background significantly.

In principle we will obtain great A_{LL} and azimuthal correlation measurements. Two caveats should be mentioned:

1. The interdependance of ΔG and L_G must be understood. Unless one of these has a value of zero in the observed range, there will be some element of ΔG that will affect the asymmetry nominally ment to measure L_G, and vice versa: certainly the cross-section for $c\bar{c}$ production from gg fusion might depend on k_T or simply on $\sqrt{s}$ and not just on the spin of g. Even if one of the two is *measured* to be zero it does not guarantee that that is the case (see Appendix C).

2. The production mechanism of open charm (or J/ψ) is poorly understood. It may be that we may learn more from these measurements about heavy quark content and production than about gluonic contributions to the proton's spin. Even the simulations available to us currently have recourse to unorthodox mecanisms to emulate charm production. PYTHIA uses the "beam drag" method to simulate charm production, whereby it accelerates a created charm quark by dragging it behind another consituent parton.

8.2.2 Drell-Yan

Since the Sivers function is process dependant, by selecting a particular kind of process, an attenuated or even different left-right single spin asymmetry should be observed.

This is the theoretical prediction for the Drell-Yan channel: it is the reverse of the semi-inclusive deep inelastic scattering (SIDIS) of a lepton off a polarized proton (Fig. 8.1). While the SIDIS has no final state interaction, the Drell-Yan channel has no initial state interaction and the processes are symmetric.

The biggest problem with measuring this effect is the small cross-section for Drell-Yan. It has been calculated that only with the increased luminosity due to electron cooling, projected to be installed 2010, will there be sufficient data to analyze in this channel.

The anticipation of such a reverse asymmetry is such that a plan for the building of a dedicated Drell-Yan detector to be installed at another interaction region on the RHIC ring is receiving strong consideration.

8.2.3 Forward Rapidity Sivers

Jet-jet azimuthal correlation studies from transversely polarized protons have a distinct advantage in that the absolute direction of k_T from POAM is known to be perpendicular to the spin direction and the beam direction. This enables a much easier extraction of the desired variables. This is the principle behind the future (2006) A_N measurements in RHIC. Because the detection regions of choice for this experiment are in the spin direction, positive and negative, PHENIX will attempt to rotate the beam direction by 90° on its side in order to align polarization direction with detector acceptance.

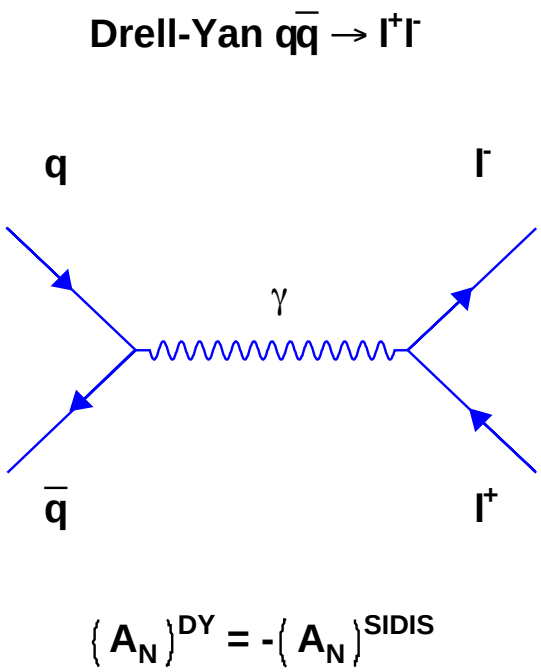

Figure 8.1: Drell-Yan diagram. The left-right asymmetry for Drell-Yan is predicted to be the opposite of the Semi-Inclusive Deep Inelastic Scattering (SIDIS) symmetry

Appendices

Appendix A

Polarimeter Proposal

A.1 AGS/RHIC CNI (Coulomb-Nuclear Interference) Polarimeters

A.1.1 Introduction

Polarimetry of proton beams with energies higher than about 30 GeV poses a difficult challenge. The Analyzing Power of only a few reactions have been measured so far [66, 67], and the value of the Analyzing Power is typically small. For a successful spin physics program at RHIC we need two different polarimeters. During the 2002 run (Run2), a $p+C$ CNI polarimeter provided a fast ($\sim$1 minute) measurement of the beam polarization in each ring, but with large scale uncertainties in the Analyzing Power, set by a previous measurement at the injection energy (E950, see Section A.1.2). This uncertainty is acceptable for tuning purposes, providing a good relative measurement of the polarization. However, to get ΔG to the accuracy desired, the beam polarization needs to be known to $\sim$5%. In order to accomplish this at the full RHIC energy, an absolute polarimeter with a polarized target is needed.

A polarized hydrogen gas-jet polarimeter was installed for Run5. This experiment will measure the p+p Analyzing Power using the known target polarization and thus extract the beam polarization to better than 5%. This will then be used to calibrate the p+C CNI polarimeters to that accuracy, providing fast, absolute and accurate measurements. The proposal we made was to solve the problem of measuring polarization accurately in the time between Run2 and Run5. For this we planned to use an experiment similar to E950 in tandem with an extracted beam frozen spin polarimeter in the AGS.

A.1.2 AGS E950 Results

E950 tested the use of small angle ^{12}C(p,p)^{12}C elastic scattering for polarimetry at RHIC. Elastic scattering in the small angle CNI region ($-t = 0.003 - 0.04(GeV/c)^2$) is predicted to have a calculable Analyzing Power of about 2-4% [68, 69], as well as a large cross section over the whole RHIC energy range from 25 GeV to 250 GeV. A carbon ribbon target was used for the high luminosities required for fast polarization measurements. A ribbon target (5μ wide $\cdot$ $3.7\mu g/cm^2$ thick $\cdot$ 3 cm long) allowed for the low energy carbon recoil to escape the target with minimal energy loss as well as possible measurements of the polarization profile of the proton beam. The sizeable Analyzing Power, the large cross section, and the advantages of a ribbon target makes this process ideal for a fast primary polarimeter for RHIC.

The AGS E950 collaboration finalized its results [70]. The data from this experiment determine the analyzing power of the p+C elastic scattering reaction based on the beam polarization measurement of a simultaneously running external beamline experiment, E925 [71].

A.1.3 Solid Polarized Target Calibration Experiment

During the Run2 proton run at RHIC, the maximum polarization measured in the AGS was approximately 25%, although measurements at injection to the Booster at 200 MeV showed ∼80% polarization. Because of the failure of the Siemens motor-generator, the AGS ramp rate was significantly slower and the depolarizing effects from resonances were greater. In order to avoid these effects, accurate AGS polarization measurements as a function of energy are crucial. In principle, the new AGS polarimeter can measure the polarization during the ramp, providing information on the change in measured asymmetry during acceleration. However, because the physics Analyzing Power is unknown throughout most of the AGS energy range (3 GeV to 24 GeV), only sharp changes in the beam polarization will be discernable from the unknown changes in the Analyzing Power.

We proposed to measure the p+C CNI Analyzing Power as a function of energy from the AGS injection energy to the RHIC injection energy via an internal p+C CNI polarimeter in the AGS (to measure the p+C CNI asymmetry) and an external p+p experiment with a solid polarized ammonia target (to measure accurately the beam polarization) analogous to the E950-E925 set-up previously discussed (Section A.1.2). In addition to calibrating the internal polarimeter over the range of AGS energies, this experiment could make a very precise measurement at the RHIC injection energy.

Because the E950 results relied on beam polarization measurements extracted from a p+p experiment, which in turn relied on asymmetry measurements from previous experiments with large error bars, the systematic uncertainty of the Analyzing Power for the p+C CNI reaction was determined to be ∼20%. Although this is the best measurement to date, and is sufficient for tuning and commissioning of the RHIC polarimeters, it is insufficient for the spin physics program at RHIC. Of course, even if the Analyzing Power were well determined at the RHIC injection energy, it most

probably has an energy dependence that is theoretically not well understood. There are, however, some ideas on determining the Analyzing Power more acccurately at 100 GeV without the polarized gas-jet target. One option discussed is to measure the asymmetry before and after acceleration, and then "down-ramp" back to injection energy and re-measure the asymmetry where the Analyzing Power is known. If this is carefully done, the polarization losses (if any) during the acceleration and deceleration processes should be the same, and any decrease in the measured asymmetry would be twice the decrease during acceleration. This method could determine the Analyzing Power at 100 GeV , albeit with systematic uncertainties which would probably be large compared to the desired 5% level. However, it would allow an absolute polarization measurement independent of theoretical analysis of the energy dependence. If this method were to work, the limiting factor in the knowledge of the polarization may well be the uncertainty of the Analyzing Power determined by E950. A decrease in this uncertainty from 20% to a possible 5% would be strongly desired, especially if the upcoming spin run is successful in generating interesting results.

A.2 Measuring Polarization

In order to interpret measurements made by the various detectors into spin related quantities, an accurate measurement of the beam polarizations must be made. Polarization measurements not only supply the final number to be used in analyses but if taken at various stages of the full accelaration chain, give important feedback to the accelerator physicists and improve understanding of polarization losses. Therfore there are polarimeters placed between the LINAC and the Booster, in the AGS ring and in the RHIC ring itself.

The principle of polarization measurement is rather simple, but unfortunately

somewhat circular: compare a measured asymmetry with a known physics asymmetry to deduce polarization using Eq. (3.1).

In practice the asymmetry A_x is measured by:

$$A_x = \frac{N_{++} - N_{+-}}{N_{++} + N_{--}} \tag{A.1}$$

where N_{++} is the number of detected particles in a certain configuration (in this example: parallel helicity events) and N_{+-} is the number of detected particles in a different configuration (in this example: anti-parallel helicity events). This formula can be modified to adapt to all asymmetry measurements (see Section 3.2.2).

Two different types of targets are used currently at RHIC:

- polarized hydrogen gas jet targets. Since the hydrogen gas jets are of low density and have a low cross-section, they are able to run in the same ring (RHIC or AGS) without damaging the beam. The x process is pp.
- Carbon targets. Here x is pC.

Unfortunately, to obtain the original physics asymmetry a_x, a similar previous experiment must be performed where this time the unknown is the a_x while the polarization P is the known quantity. To break from what appears to be a vicious circle, fixed target experiments, so called "frozen spin", are used to determine the physics asymmetries. In these experiments an unpolarized beam is used upon a polarized target.

The idea is to run such an experiment in the AGS on a extracted beam line in conjunction with another polarimeter in the AGS ring similar to E950. The polarimeter on the extracted beam would be a "frozen spin" target, *i.e.*: frozen NH_4 with the H nuclei polarized and the target kept cold. The advantage here is that the

polarization of the target can be measured extremely precisely, and therfore the beam polarization can be measured precisely. The following steps diagramed in Fig. A.1 outline the method to measuring polarization at RHIC:

1. Using non-polarized p beam on polarized p target on the extracted beam polarimeter (polX), the pp asymmetry (A_{pp}) is measured using Eq. (A.1).

2. The polarization of the frozen spin (P_{pp}) is known accurately and the Analyzing Power (a_{pp}) of polX is calculated using Eq. (3.1).

3. Using polarized beam into the AGS, data (A_{pC}) is taken at the AGS (E950) polarimeter.

4. The polarized beam is dumped into the extracted beam.

5. Using the Analyzing Power (a_{pp}) obtained from (1.) the polarization of the beam (P) is calculated using a new set of data (A_{pp}) measured in the extracted beam by the frozen spin polarimeter, now in a non-polarized state.

6. The data obtained by the AGS polarimeter (3.) is analyzed using the polarization (P) obtained from the frozen spin polarimeter, and the p+C Analyzing Power (a_{pC}) for the E950 polarimeter is calculated using Eq. (3.1) to within 5%.

7. The p+C Analyzing Power (a_{pC}) is now used by the RHIC CNI polarimeter to measure the polarization in RHIC, or by the same E950 polarimeter to measure the polarization in the AGS.

The utility of such an experiment is limited by the fact that the Analyzing Power (a_{pC}) is energy dependent. While we could measure the value of the Analyzing Power in the AGS range (3-24 GeV) we would still be dependent on correct extrapolation of those results to the RHIC range (100-250 GeV) which carries more uncertainty.

Of course, this added uncetainty already exists for the current polarization measurements.

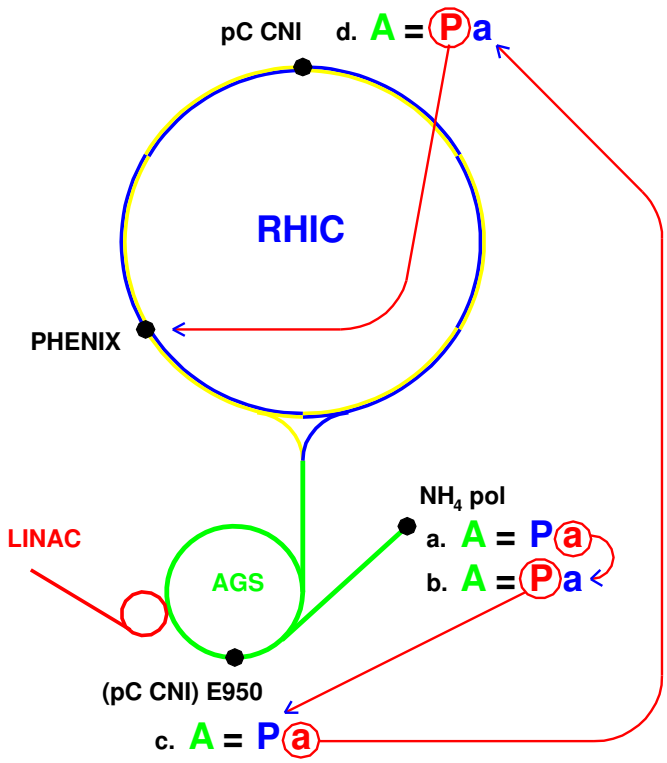

Figure A.1: Measuring polarization at RHIC. This diagram shows the location of the different polarimeters involved in the new proposed polarimetry experiment. Except for the extracted beam frozen spin polarimeter, the polarimeters are all already in place and in use.

A.3 Proposed Polarimeter Study

A.3.1 Principle

The principle behind the proposed polarimeter is to measure the asymmetry in the elastic scattering of protons.

The elastic collision between the incoming proton and the Hydrogen in the NH_4 target constrains the kinematics such that there is only one free parameter:

$$\sin\theta_R \approx \left(1 + \frac{m_P}{p_{beam}}\right)\frac{\sqrt{|t|}}{2m_P} \tag{A.2}$$

where m_P is the mass of the proton θ_R is the angle of the trajectory of the recoil proton, t is the Mandelstam parameter given by:

$$t = -2m_p E_R \tag{A.3}$$

proportional to the recoil energy (Fig. A.2). The energy and angle of the recoil proton are also correlated, as are the energy and angle of the scattered proton. By measuring one of the variables we can measure the elastic scattering signal. By measuring both, we eliminate some of the background. By measuring more kinematical variables which are all interdependent in elastic scattering, we increase the signal to noise ratio. In other words, by over-constraining we should be able to identify elastic scattering events. The maximum asymmetry for CNI p+p scattering has been measured at a t range of 0.22 - 0.38 GeV^2/c^2. The corresponding ranges for θ_R and E_R are given in Table A.1.

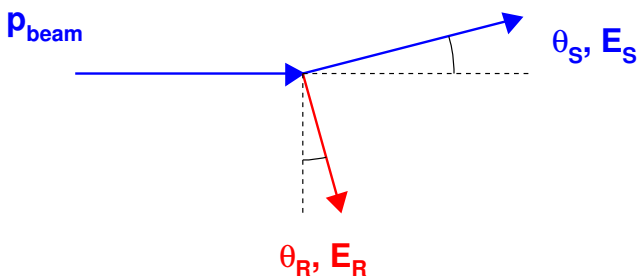

Figure A.2: Elastic scattering kinematic variables

variable	range
t	(0.22 - 0.38) GeV $^2/c^2$
θ_R	13 - 15 °
E_R	110 - 170 MeV

Table A.1: Kinematic variable range for CNI elastic scattering

A.3.2 Experimental Setup

The plan for the experimental setup was to fit the frozen spin target from the University of Virginia [72] used for previous experiments and encase it in an Aluminium can connected to the beam to maintain vacuum around the experiment. The Aluminium container would be fitted with windows in the forward and recoil directions.

The detectors would be either silicon strip or scintillator hodoscopes with good position resolution in the side(recoil) direction. In the forward direction, calorimeters would be used to measure the energy and could be combined with silicon detectors placed in front. In order to get good angular discrimination, the forward detectors would be placed downstream 10 - 20 m.

This polarimeter was proposed in June 2002 before the RHIC Spin Collaboration, Fig. A.3 shows the GEANT generated schema of the extracted beam polarimeter.

A.3.3 Simulation

We used GEANT generated Monte Carlo events to simulate detector response and to optimize signal to background ratios by experimenting with different detector combinations. In addition to the silicon recoil detectors, forward detectors with hodoscopes and calorimetry were used in simulation.

The time of flight of the detected protons in the silicon detectors is shown in Fig. A.4. The simulated times are well below the threshold necessary to ensure discrimination between bunches, which come every 330 ns. The signal events lie within the blue box area, which enables a time of flight cut at the red line to reduce background.

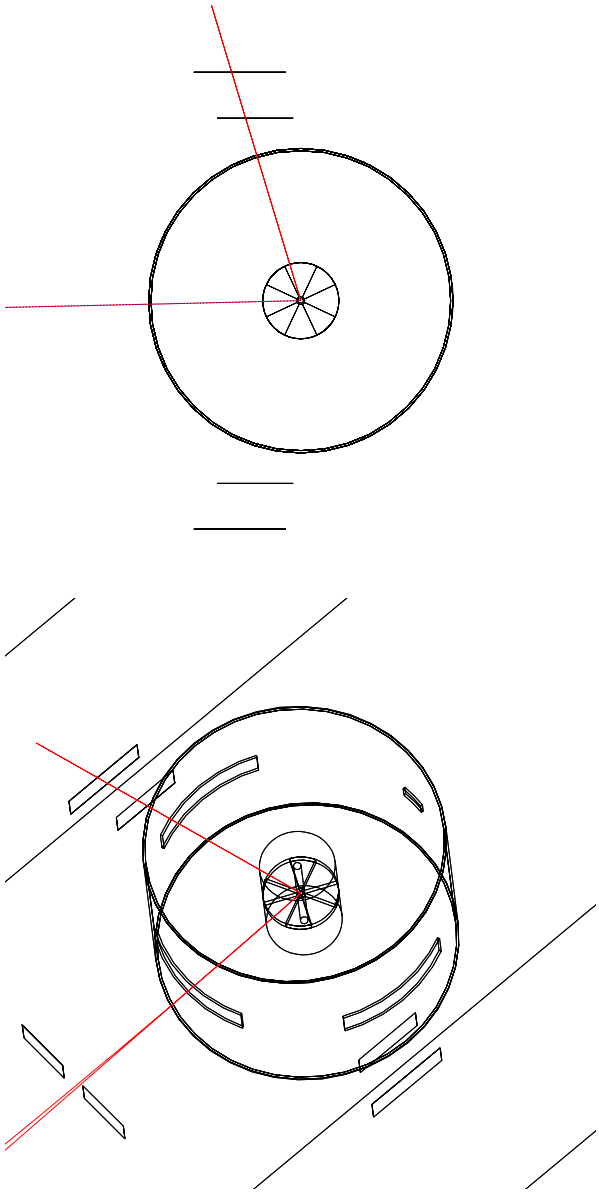

Figure A.3: *(top)* Top view of polarimeter. The outer circle is the Aluminium container, the sectioned inner circle is the actual frozen spin polarimeter that contains the target. The blue line is the forward scattered proton in an elastic scattering event, and the red line is the recoil proton. The path of the recoil proton intersects two silicon detectors.*(bottom)* Side view of polarimeter. Both the forward and recoil proton are now represented by red lines. The windows in the Aluminium can can be seen as well as the forward detectors.

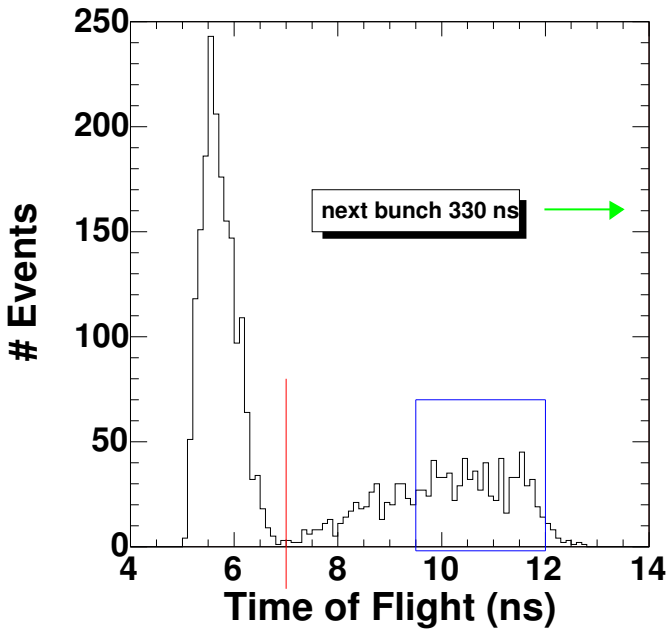

Figure A.4: Polarimeter time of flight in the side silicon detectors. The red line represents a background cut. The signal events are located within the blue box, whose width is determined by the kinematics of elasctic scattering. The large peak at low time consists of charged pions.

Fig. A.5 shows the coincidence events which record a hit in the left forward and right side detectors. The background, though relatively small is still present. The line represents the signal events. Since the signal has only one free parameter, the events show a definite correlation between measured kinematic quantities. Because of the strong correlations, we showed that rather than have two layers of side detectors, it would be more efficient to have a collimator in front of a single side detector.

Fig. A.6 shows that by over-constraining we can eliminate more background. First we plotted recoil energy versus recoil angle, where we saw a definite separation between signal and background. Because elastic scattering conserves kinetic energy,

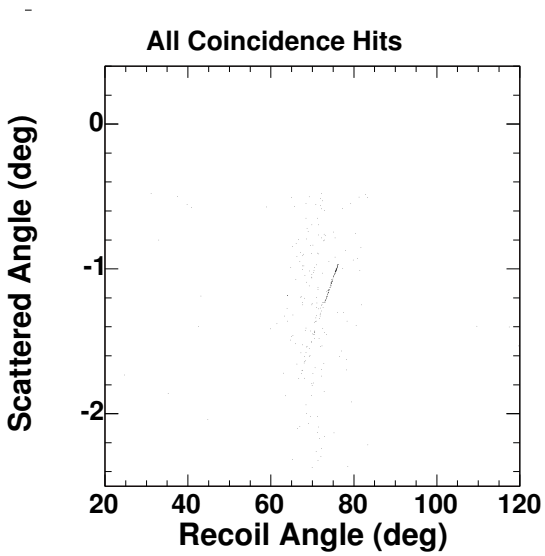

Figure A.5: $\phi - \phi$ correlation. The signal events show a strong correlation between kinematic quantities as evidenced by the visible line.

the forward protons should have nearly all of their initial energy. In the forward energy versus recoil angle plot, the separation between signal and background is even more obvious.

The new forward energy background cut $E_f > 22.9$ GeV is applied in Fig. A.7, with the same measured quantities as in Fig. A.5. The background is completely eliminated. A more advanced study to account for background from sources other than interactions with the target would be necessary to complete a signal to background estimate. Nevertheless, we can say that silicon recoil detectors which measure position and timing coupled with collimators on the sides, combined with forward hodoscopes (for position) and calorimeters (for energy) show good background rejection.

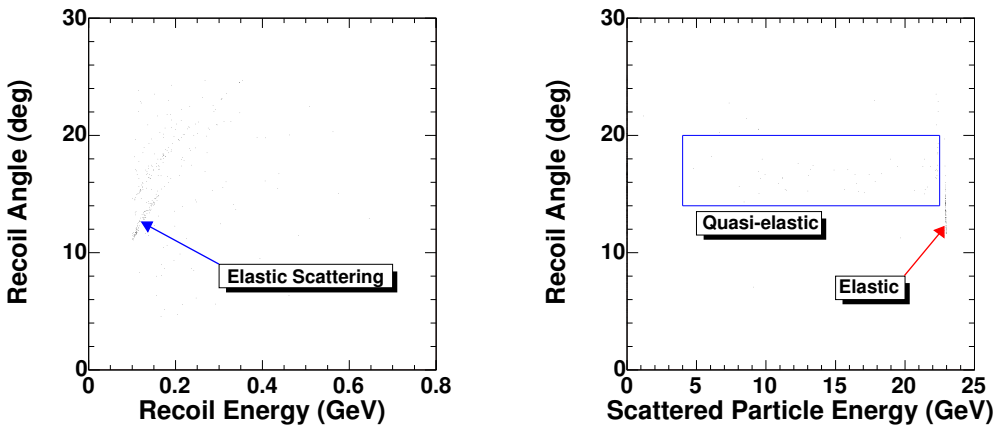

Figure A.6: Over-constraining. *(left)* shows recoil angle plotted versus recoil energy and a separation between signal and background events. *(right)* shows recoil angle versus forward energy and an even more distinctive background cut.

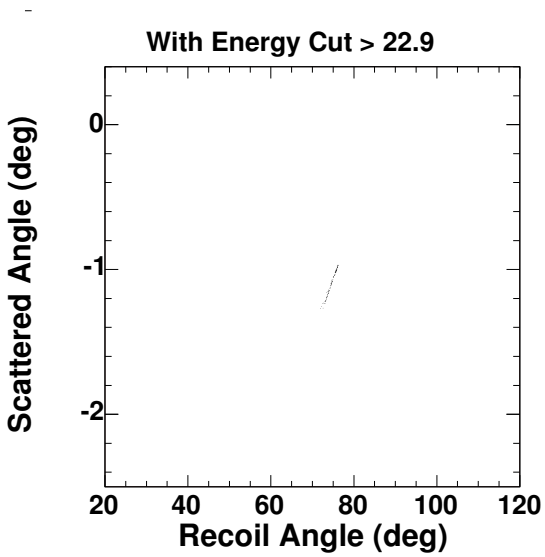

Figure A.7: $\phi - \phi$ correlation with forward energy cut: $E_f > 22.9$ GeV. The background is completely eliminated.

A.4 Proposal Conclusions

To calculate the run time required for our study we considered the following values:

- The AGS would deliver bunches of $1.20 \cdot 10^{10}$ protons per spill
- One spill comes every 4 s.
- Our target has $2 \cdot 10^{23}$ atoms
- Luminosity is then:

$$\mathcal{L} = 1.2 \cdot 10^{10} \times 1/4 \times 2.0 \cdot 10^{23} = 6.0 \cdot 10^{32} cm^{-2} s^{-1} \tag{A.4}$$

- Our event rate would then be:

$$N = \mathcal{L} \cdot \sigma(5.0 \cdot 10^{-27}) \cdot acc(0.01) \cdot eff(50\%) = 5000 \text{ evt } s^{-1} \tag{A.5}$$

We would need 1 week (21 shifts) of runtime to collect data. In addition to which we would need 2 weeks for tuning and testing etc.

Our proposal was not accepted, in large part because it was deemed to be a considerable financial effort for such a limited time, knowing that the RHIC gas-jet polarimeter would be installed for run5.

Appendix B

ΔG Measurement from Open Charm Decay Coincidence Events

B.1 Introduction

This appendix details an attempt to measure ΔG, the gluon contribution to the proton's spin, through the measure of the asymmetry of $e\mu$ (and other) coincidence events from open charm decay. At relatively low p_T, it is believed that open charm production in p+p collisions is dominated by gluon-gluon fusion (see Fig. B.1). Therefore, one has but to determine the number of open charm events for both parallel and anti-parallel collisions to obtain a measure of ΔG. The measured asymmetry A_{LL} is related to ΔG by:

$$A_{LL}^{c\bar{c}}(x_1, x_2) = \frac{\Delta G}{G}(x_1)\frac{\Delta G}{G}(x_2)\, a_{LL}^{gg\to c\bar{c}} \tag{B.1}$$

where $\frac{\Delta G}{G}(x)$ is the gluonic contribution to the proton's spin for a gluon with momentum fraction x, $a_{LL}^{gg\to c\bar{c}}$ represents the theoretical asymmetry in $c\bar{c}$ production

from gluon-gluon fusion, and $A_{LL}^{c\bar{c}}$ the measured asymmetry in $c\bar{c}$ production from polarized p+p collisions. The equation for $a_{LL}^{gg\to c\bar{c}}$ is given by:

$$a_{LL}^{gg\to c\bar{c}} = \frac{\sigma^{\to\to}_{gg\to c\bar{c}} - \sigma^{\to\leftarrow}_{gg\to c\bar{c}}}{\sigma^{\to\to}_{gg\to c\bar{c}} + \sigma^{\to\leftarrow}_{gg\to c\bar{c}}} \tag{B.2}$$

Here we see that a_{LL} is the normalized difference of partonic cross-sections. The cross-sections are calculated to NLO [73] for $gg \to c\bar{c}$ for two spin configurations: when the gluon helicities are parallel ($\to\to$) and when the gluon helicities are anti-parallel ($\to\leftarrow$). The equation for $A_{LL}^{c\bar{c}}$ is:

$$A_{LL}^{c\bar{c}} = \frac{\sigma^{++} - \sigma^{+-}}{\sigma^{++} + \sigma^{+-}} \tag{B.3}$$

where σ^{++} and σ^{+-} are the cross-sections of a specific reaction channel (here open charm production) when the protons have parallel ($++$) and anti-parallel ($+-$) helicities, respectively. The strength of this asymmetry depends on how correlated the gluons' polarization is compared to the proton's (Eq. (B.1)). Practically, since the cross section can be written by experimental yield (N) divided by integrated luminosity ($\hat{\mathcal{L}}$) and overall efficiency (ϵ) and ϵ can be assumed to be helicity independent, we use:

$$A_{LL}^{c\bar{c}} = \frac{1}{P_B \cdot P_Y} \frac{N^{++} - RN^{+-}}{N^{++} + RN^{+-}} \tag{B.4}$$

where:

- P_B and P_Y: the polarization of the blue and yellow beams, respectively.
- N^{++} and N^{+-} are the number of signal events measured when the the beam helicities are parallel ($++$) or when the beam helicities are anti-parallel ($+-$), respectively.

- R: the relative luminosity

$$R = \frac{L_{++}}{L_{+-}} \tag{B.5}$$

- L_{++} and L_{+-} are the parallel helicity and anti-parallel helicity total luminosities, while P_B and P_Y are the polarizations of the two beams, blue and yellow.

For Run3pp the values used are:

$$P_B = P_Y = \sqrt{P_B \cdot P_Y} \approx 27\% \tag{B.6}$$

$$R = \frac{L_{++}}{L_{--}} \approx 97.25\% \tag{B.7}$$

Complications are inevitable when moving from theory to practice, in this case some of the complications are as follows:

- $c\bar{c}$ quarks are not the end particles, they fragment with other quarks to form charmed hadrons such as D mesons or Λ_c baryons. These in turn decay strongly, weakly or electromagnetically into stable particles that are produced copiously through other production channels, thus creating the problem of being able to distinguish signal from background.

- In Eq. (B.1) $\Delta G/G$ is a function of the momentum fraction x of the interacting parton. The A_{LL} that we seek to ascertain is a function, not a value, and relating final state particles to intial state variables is complicated.

- The factor $\Delta G/G$ appears twice in A_{LL}, it is the product of the contribution from the two interacting gluons.

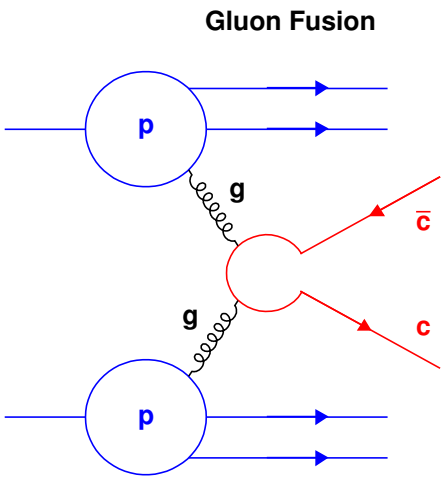

Figure B.1: Schematic diagram of the main LO process in open charm production.

The primary utility of these analyses becomes clear by examining Eq. (B.1). The asymmetry is a function of the momentum fraction values of both interacting gluons. By detecting a decay particle corresponding to one of or both of the two gluons we can make better comparisons to the different models (Fig. B.3), knowing from Pythia simulations that there is a strong correlation between the type of particle detected and the momentum fraction of the gluon, due simply to the detector acceptance for the different particles (Fig. B.2) in PHENIX. This also underscores the need for A_{LL} measurements from different decay channels, as they will probe different x regions of the $\Delta G/G$ models.

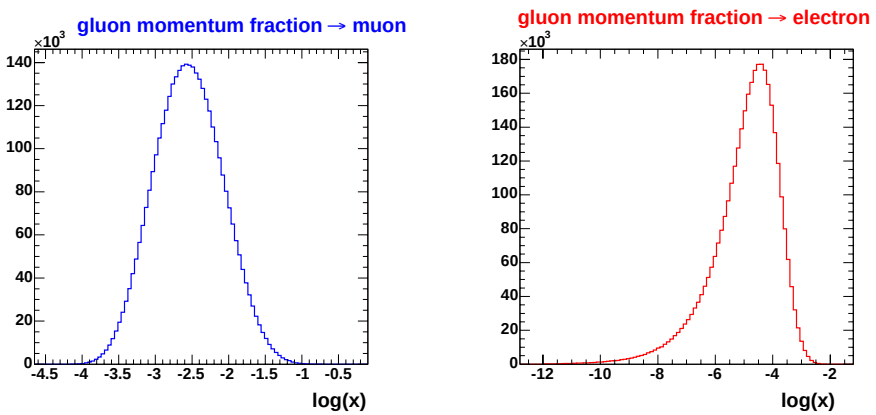

Figure B.2: Gluon momentum fractions in log scale for $e\mu$ coincidence events. *(left)* gluon momentum fraction for gluons that decay to muons that are within PHENIX muon acceptance. *(right)* gluon momentum fraction for gluons that decay to electrons that are within PHENIX electron acceptance. The different values reflect the PHENIX acceptance for the different leptons and not any physics processes.

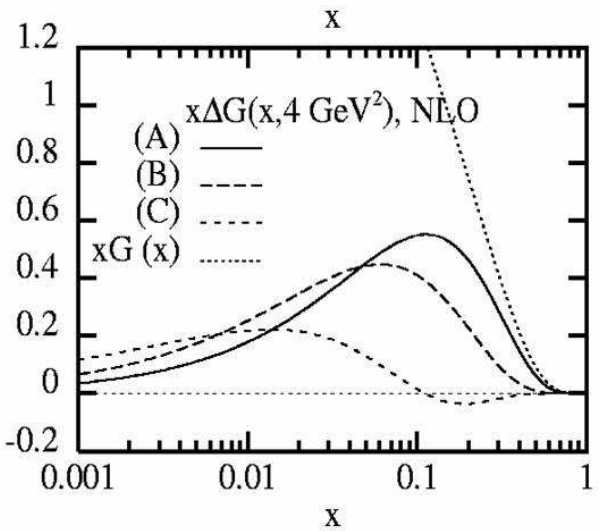

Figure B.3: $x \cdot \Delta G$ plotted as a function of x from NLO calculations for various models

B.2 Methodology

The idea of coincidence event studies is to improve upon the signal to background ratio; the disadvantage is that it decreases the statistics available for study. We are therefore looking for a coincidence signal from open charm decay that has, if possible:

- Good signal to background
- High statistics
- Low theoretical uncertainty

To consider the different coincidence signal possibilities, we look for the different possible decay channels. We are interested primarily in semi-leptonic decay modes, as PHENIX is designed to detect electrons, muons and photons, with a limited amount of particle identification for hadrons (TOF). From PYTHIA, we know that $c\bar{c}$ pairs hadronize into D mesons 99.5% of the time, with the constraint that the final state particles be leptons within PHENIX acceptance. In turn, the D mesons $(D^0, \bar{D}^0, D^+, D^-)$ decay along various different channels. Some branching ratios include:

- $D^0 \rightarrow e^+ + X(7\%)$
- $D^0 \rightarrow \mu^+ + X(7\%)$
- $D^+ \rightarrow e^+ + X(17\%)$
- $D^+ \rightarrow \mu^+ + X(10\%)$
- $D^0 \rightarrow e^+ + K^- + X(5\%)$
- $D^+ \rightarrow e^+ + K^- + X(4\%)$

We could detect $e^{\pm}\mu^{\mp}$ pairs, $e^{\pm}K^{\pm}$, or $e^{\pm}K^{\mp}$. The opposite sign eK pairs would come from the same D meson, while the same sign eK pairs would have each particle decay from a different D meson. The muon arm momentum acceptance would make it impossible to detect a μK pair from the same meson, but $\mu^{\pm}K^{\pm}$ from 2 different D mesons is possible.

A look at PYTHIA generated open charm production from p+p collisions with generic PHENIX acceptance cuts would help us determine what the best signal might be. The results are shown in Table B.1.

Mode	Produced	Accepted	%
$e^{\pm}\mu^{\mp}$ (emu)	695M	957K	0.1
$e^{\pm}K^{\pm}$ (elk)	485M	5.3M	0.4
$e^{\pm}e^{\mp}K^{\pm}$ (eek)	847M	222K	0.03
$e^{\pm}\mu^{\mp}K^{\mp}$ (emuk)	2.35G	477K	0.02

Table B.1: MC acceptance modes

We see that asking for three particles would severely limit our statistics. Although electrons are relatively easy to come by, both muons and Kaons have a rather limited PHENIX acceptance, muons from a kinematic standpoint $p_{\mu} > 2.2\text{GeV}/c$ and Kaons from a geometrical standpoint (they can only be identified in the TOF). The two most promising candidates are the $e\mu$ (emu) and the eK (elK). The advantage of $e\mu$ is that both single electron and single muon studies from open charm decay are currently underway and we can refer to both working groups for cuts and analysis techniques.

Nevertheless, there are important differences between our study and the single lepton analyses. For the single lepton studies which rely on statistical methods to determine signal, any electron (respectively, muon) that originates from an open charm decay is considered signal, regardless of the decay process. In our analysis, for there to be correlations between the detected particles we only consider leptons and Kaons that originate exclusively from semi-leptonic D meson decay. This means our signal number is somewhat shrunk again and that a contribution from open charm exists in our background asymmetry.

The theoretical improved signal to background cannot be proved, because unlike the J/ψ study, we cannot detect all decaying particles and reconstruct the D meson masses; we can only estimate our signal to background ratio by calculating the number of $e\mu$ events Eq. (B.8). Using the same cuts as developped by the Single Muon and Single Electron Working groups (Table B.2), the number of coincidence events is determined and compared to the number of open charm events calculated from the formula:

$$N = L \cdot \sigma_{p\bar{p}\to c\bar{c}X} \cdot \Gamma_{c\bar{c}\to D\bar{D}} \cdot \Gamma_{D\bar{D}\to e\mu} \cdot \varepsilon_{e\mu acc} \cdot \left(\varepsilon_{ereco} \cdot \varepsilon_{eacc}\right)_{CNT} \cdot \varepsilon_{\mu reco} \tag{B.8}$$

where:

- L : Collected Luminosity. Includes down time and vertex cut losses. Collected for Run 3: 300 nb^{-1}.
- $\sigma_{p\bar{p}\to c\bar{c}X}$: Cross-section for $p\bar{p}$ to $c\bar{c}$. Value used: 644 μb as measured by PHENIX.
- $\Gamma_{c\bar{c}\to D\bar{D}}$: Branching ratio for $c\bar{c}$ pair to $D\bar{D}$ pair. Calculated using 4M Pythia events: 99.5%, when constrained by PHENIX geometric and kinematic acceptance for leptons.

Electron	Muon
EMC dphi sigma < 3	no ghostflag
EMC dz sigma < 3	No Muon Tracker Hits ≥ 12
energy/momentum ratio cut < 2.5	Track Chi Square < 20
fiducial cuts	No Tracks Cut ≤ 10
No RICH Hits > 3	No Muon ID Hits ≥ 7
BBC vertex Cut ≤ 20	BBC vertex Cut ≤ 20cm

Table B.2: Muon/Electron Working Groups particle ID cuts

- $\Gamma_{D\bar{D}\to e\mu}$: Branching ratio for $D\bar{D}$ pair to $e\mu$ pair. Calculated using 4M Pythia events: 1.67%.
- $\varepsilon_{e\mu acc}$: Acceptance of $e\mu$ pairs. Percentage of $e\mu$ pairs that fall into geometric and kinematic range of the muon detector and the central arm acceptance · efficiency study for the central arm (see next item). Using the following cuts for the 4M Pythia events, we obtained: 7.56% for (Selection 1 and Selection 2), 1.91% for Cut Selection 2 Only (see Table B.4).
- $(\varepsilon_{eacc} \cdot \varepsilon_{ereco})_{CNT}$: Electron acceptance·efficiency in the Central Arm. Value taken from PPG037: 3% for Selection 2, and 2.4% for Selection 1.
- $\varepsilon_{\mu reco}$: Muon Arm efficiency. Standard value from Single Muon Working Group: 70%.

The number of $e\mu$ coincidence events from open charm decay is given in Table B.3

Run	Luminosity (pb^{-1})	$e\mu$ events ($ep_T > 0.4$ GeV/c)	$e\mu$ events ($ep_T > 0.8$ GeV/c)
Run 3/Run 4	0.3	817	248
Run 5	10	27258	8263

Table B.3: Number of $e\mu$ coincidence events from open charm

The statistical relative error on A_{LL} is given by the formula:

$$\frac{\delta A_{LL}}{A_{LL}} = \frac{1}{P_B \cdot P_Y \cdot \sqrt{N}} \tag{B.9}$$

which, considering the number of calculated $e\mu$ coincidence events in Run3pp is very large, especially considering that our N can only get smaller as we explore phase space correlations. At best for Run3 we can obtain a qualitative feel for an asymmetry. Then there are other sources of uncertainty, such as the uncertainty in the polarizations which gives an additional:

$$\frac{\delta A_{LL}}{A_{LL}} \sim 60\% \tag{B.10}$$

B.3 Analysis

The first step is to compare our single muon p_z spectrum with that of the single muon asymmetry studies [74]. The cuts used by the single lepton groups and our analysis are given in Table B.2, and the comparison of our single muon results to those shown previously is shown in Fig. B.4.

Selection 1	Selection 2
$P_\mu > 2.1$ Gev	$P_\mu > 2.1$ Gev
$1.2 < \lvert\eta_\mu\rvert < 2.4$	$1.2 < \lvert\eta_\mu\rvert < 2.4$
$0.4 < Pt_{el} < 0.8$	$Pt_{el} > 0.8$
$\lvert\eta_e\rvert < 0.5$	$\lvert\eta_e\rvert < 0.5$

Table B.4: MC acceptance cuts

By using PYTHIA generated Monte Carlo $e\mu$ events from $c\bar{c}$ production, we looked for phase space correlations.

The first consideration was that the momentum acceptance for the muons made it extremely likely that the muon direction was related to the decaying D meson

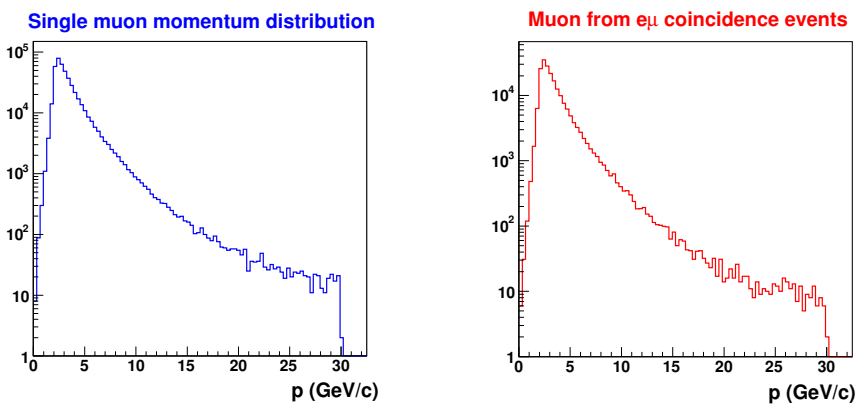

Figure B.4: Muon momentum distribution. *(left)* for single muons, *(right)* for muons in $e\mu$ cincidence events.

direction. This was confirmed in PYTHIA simulation (Fig. B.5).

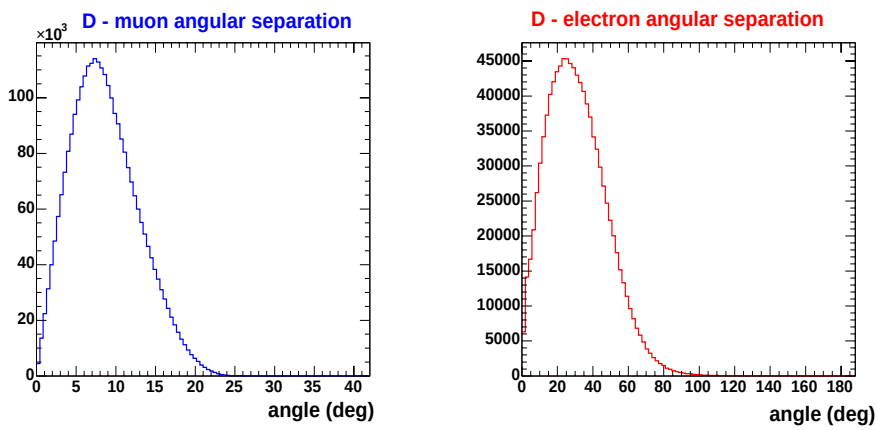

Figure B.5: Angular deviation in degrees of lepton from parent D-meson for *(left)* muons, and *(right)* electrons ($p_T >$ 0.7GeV)

The distribution of the angle between the leptons is indicative of the geometrical acceptance of the PHENIX detectors and the momentum fractions of the interacting gluons, and therefore the z-component of the detected lepton momenta. By looking exclusively in the transverse plane, a more back-to back correlation is observed in PYTHIA. By adding the cut on the p_T of the electron, $p_T > 0.7$ GeV/c (used in the fiducial cuts to identify the electron in the data), we introduce a stronger correlation. Because of a smaller spread in the decay angle from the D meson to the electron. A definite angular correlation in the p_T-plane is observed, as shown inFig. B.6.

Whereas fully 52.5% of the pythia generated events show a δ_T angle between leptons greater than 140 °(Fig. B.6), the data is relatively invariant with respect to this angle, showing, if anything a fall-off at large angles.

Similarily, for electron-Kaon coincidences, angular correlations in the transverse plane can be seen using PYTHIA Monte Carlo. Here there are two cases of interest: the Kaon and the electron can decay from the same charmed hadron, in which case

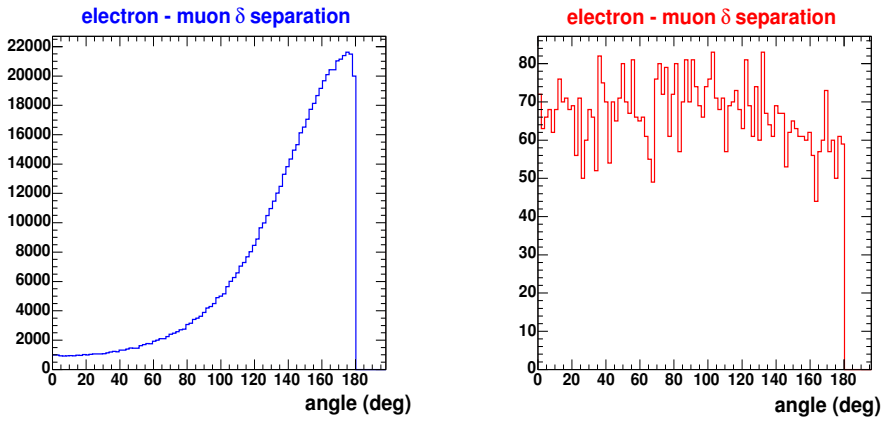

Figure B.6: Angular electron - muon separation in the transverse plane in degrees for *(left)* PYTHIA simulated coincidences, and *(right)* in Run3pp data.

they will most likely be of opposite charge, or from the different charmed hadrons, in which case they will most likely have the same charge. Using the cut p_T>0.7 GeV for both the electron and the Kaon we see the correlations shown in Fig. B.7. For the Kaon coincidences, an additional problem factor arises. The central arm detectors

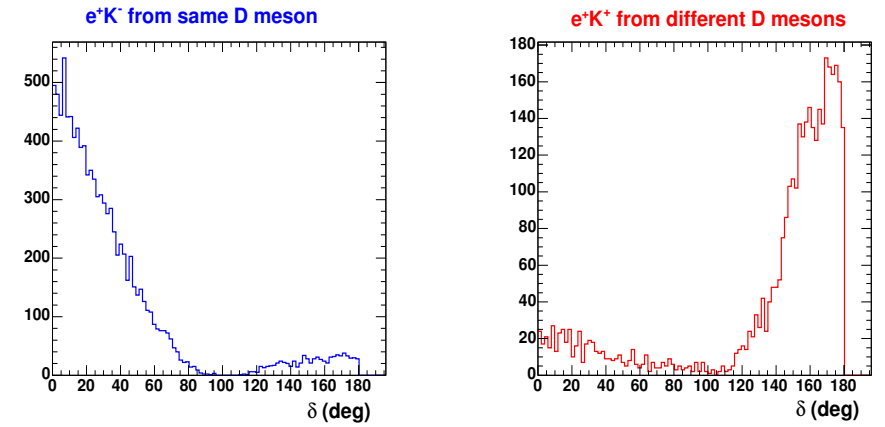

Figure B.7: Angular electron - Kaon separation in the transverse plane. *(left)* $e^{\pm}K^{\mp}$ from the same D meson. *(right)* $e^{\pm}K^{\pm}$ from different D mesons.

for PHENIX during run3 were not equipped for particle identification execpt in the TOF, which covers only a small fraction of the phase space covered even by the central detectors, thus making the analysis even more statistically challenging.

From the observed correlations we want to define a region in phase space where there is a strong signal, and a region where there is none (or a very small signal). We measure the asymmetries in the two regions, and using the estimated number of signal events we deduce the signal asymmetry. This method introduces even more uncertainty, as the uncertainty on each factor of Eq. (B.8) must be taken into account.

Fig. B.8 shows some of the more probing results.

The first figure shows a comparison of the number of $e\mu$ events in the case of like sign leptons and unlike sign leptons. From our definitions of signal and from Monte Carlo we know that our signal is almost completely unlike-signed. The second figure (bottom left) shows a comparison of parallel and anti-parallel helicity unlike-sign $e\mu$ events. The top right figure shows the number difference between these two and the last panel shows the asymmetry. All of these are plotted as a function of the angular separation between the electron and muon in the transverse plane (δ_T). The minimum p_T requirements are muon $p_T > 0.8\text{GeV}/c$ and electron $p_T > 0.8\text{GeV}/c$ The scale (in %) of the y-axis and the fluctuations give an idea of the order of magnitude of the uncertainties. Asymmetry values are calculated for two angular regions $\delta_T > 140^\circ$ and $\delta_T < 90^\circ$ for both like and unlike-sign pairs. The values are shown in Table B.5.

The error bars shown in Table B.5 are only statistical. To those values, the scaling error due to the uncertainty on the polarizations must be added ($\pm$ 60 %), as well as uncertainties due to the relative luminosity. The asymmetry values shown are a mixture of signal and background asymmetries.

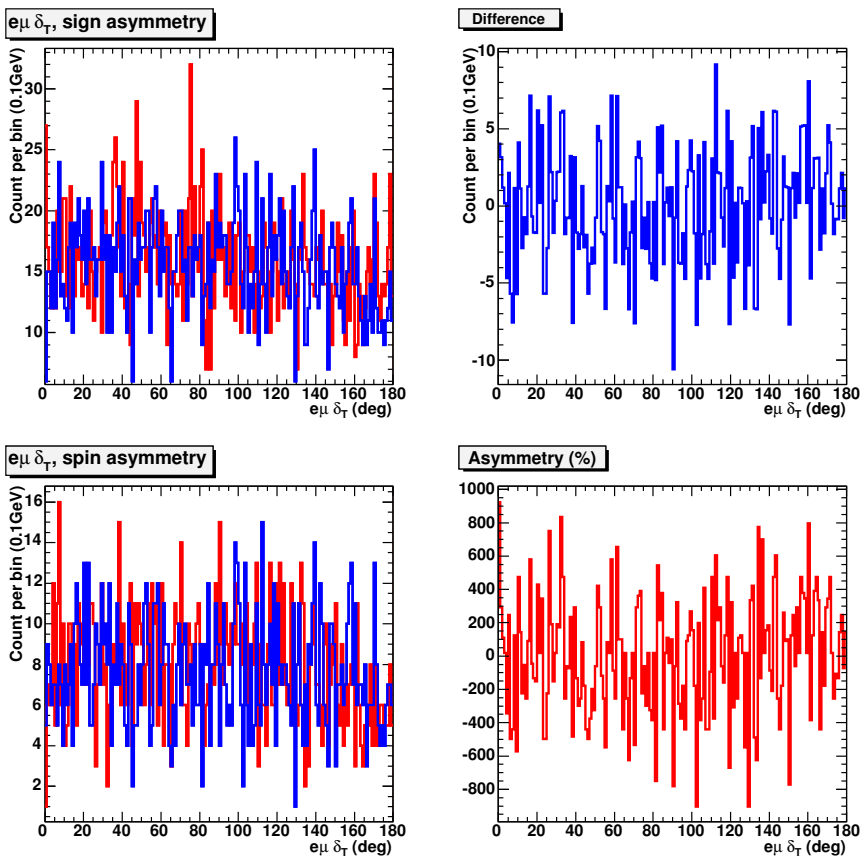

Figure B.8: $e\mu$ coincidence event asymmetries. All plots are a function of angular separation in the transverse plane.*(1. top left)* the blue line show like-charge $e\mu$ pairs (background) and the red line shows like-sign $e\mu$ pairs (potential signal). *(2. bottom left)* The blue line shows the number of like-sign parallel helicity $e\mu$ pairs, while the red line shows the number of like-sign anti-parallel $e\mu$ pairs. *(3. top right)* The difference between the two functions plotted in *2.* is shown. *(4. bottom right)* the asymmetry between the two functions is plotted.

	$\delta_T < 90°$	$\delta_T > 140$	all $e\mu$ events
like-sign	(-29 ± 49)%	(19 ± 52)%	(18 ± 22)%
unlike-sign	(-66 ± 116)%	(147 ± 428)%	(-21 ± 26)%

Table B.5: $e\mu$ coincidence asymmetries

The size of the error bars precludes even the most cautious qualitative statement concerning the significance of the results, and this is without attempting to extract a value for the signal $A_{LL}^{c\bar{c}}$. Knowing the number of expected signal $e\mu$ pairs and the ratio of signal events in the two angle bins calculated using PYTHIA (Fig. B.6): 63.7% have $\delta_T > 140°$ and 7.8% are in the $\delta_T < 90°$ bin, we could in theory attempt to extract $A_{LL}^{c\bar{c}}$ for our narrowly defined signal $e\mu$ pairs. The added systematic errors due to the uncertainty for each factor in Eq. (B.8) would be very large. Moreover this type of analysis only works if we can resonably assume that the background asymmetry is constant. This is clearly not an assumption we can make in this.

The improved scale and statistical uncertainties commensurate with a larger data set with better polarization, such as Run5, will not compensate for the inherent problems mentioned above, and will not enable a reasonable estimate on $A_{LL}^{c\bar{c}}$ from $e\mu$ (and other) concidence events.

A definitive analysis for A_{LL} from open charm will have to wait until the installation of the silicon vertex detector, which with the ability to identify displaced vertices as well as a near 4π coverage for charged tracks will enable the identification of D mesons directly.

Appendix C

Revisiting the π^0 A_{LL} Measurement

C.1 Introduction

If POAM exists then its effects would manifest themselves in other measurements. For example, POAM could contribute to the π^0 A_{LL}. It seems likely than such effects would be minor compared to the ΔG contribution, just as other contributions to the two particle azimuthal angle asymmetry are small compared to the POAM asymmetry. Nevertheless, it is interesting to get an idea of the size of POAM effects in π^0 A_{LL}, which we will do in this appendix by considering two origins of A_{LL} asymmetry from POAM:

1. The modification of parton-parton $\sqrt{\hat{s}}$.

2. An increase in π^0 p_T due to the k_T kick.

C.2 Modification of $\sqrt{s}$

As shown in Fig. C.1 (left), colinear proton collisions with PAOM can lead to non-colinear partonic collisions. In addition to creating final state dependencies, this will change the $\sqrt{s}$ of the collision and may be different depending on the helicity configurations. The principle of how this would create an asymmetry is shown in the right panel of Fig. C.1:

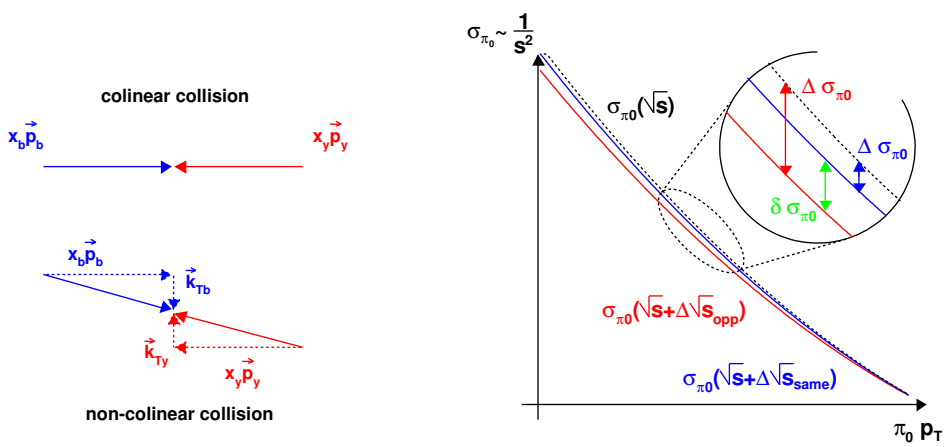

Figure C.1: *(left)* Colinear proton collisions with PAOM can lead to non-colinear partonic collisions, which will modify the $\sqrt{s}$ of the partonic collision. *(right)* The difference in $\sqrt{\hat{s}}$ resulting from non-colinear partonic collisions inside colinearly colliding protons due to POAM, results in a change of the π^0 cross-section, because the cross-section has a $1/s^2$ dependency. An increase in $\sqrt{\hat{s}}$, which we can consider equal to a change in $\sqrt{s}$ when calculating the cross-sectional dependence, results in fewer π^0 and the difference in $\sqrt{s}$ on average between parallel and anti-parallel helicity events would result in a difference in cross-section which would be measured as A_{LL}.

Using the model assumptions developed in Chapter 7, we will examine the consequences of a non-colinear partonic collision. The well-known relation between energy,

mass and momentum for a relativistic parton with k_T is:

$$E^2 = \vec{p}^2 + m^2 = x^2 p_z^2 + k_T^2 + m^2 \tag{C.1}$$

where E and m are the energy and mass of the parton, but p_z is the momentum of the proton, which is then modified by x. The partonic center of mass energy is:

$$\hat{s} = m_1^2 + 2E_1E_2 - 2x_1x_2\vec{p}_1 \cdot \vec{p}_2 - 2\vec{k}_{T1} \cdot \vec{k}_{T2} + m_2^2 \tag{C.2}$$

We shall neglect the parton mass terms and incorporate them into the momenta by setting $p_z = 100$ GeV/c. This gives us $\sqrt{s} = 200$ GeV in the absence of POAM. We will denote $\sqrt{s}^*$ the POAM-modified center of mass energy and $\sqrt{\hat{s}} = x_B x_Y \sqrt{s}^*$ the POAM-modified partonic center of mass energy.

Eq. (C.1) becomes:

$$E_B = \sqrt{\vec{k}_{Bx}^2 + \vec{k}_{By}^2 + x_B^2 \frac{s}{4}} \tag{C.3}$$

By factoring out $x_B^2 s/4$ and using the binomial theorem, we obtain:

$$E_B = \frac{x_B\sqrt{s}}{2}\left(1 + \frac{2\vec{k}_B^2}{x_B^2 s}\right) \tag{C.4}$$

substituting into Eq. (C.2) gives us:

$$x_B x_Y s^* = \frac{x_B x_Y}{2}\left(\sqrt{s} + \frac{2\alpha^2\vec{s}_B^2}{x_B^2\sqrt{s}}\right)\left(\sqrt{s} + \frac{2\alpha^2\vec{s}_Y^2}{x_Y^2\sqrt{s}}\right) - 2\left(\vec{k}_B \cdot \vec{k}_Y - x_B x_Y \frac{s}{4}\right) \tag{C.5}$$

The dot product of the two k_T vectors depends on the helicity states. We remember from Section 7.3 that $\|\vec{k}_B\|$ and $\|\vec{k}_Y\|$ are proportional to $\|\vec{s}_B\|$ and $\|\vec{s}_Y\|$, respectively (by a factor α), that the $\vec{k}_{B,Y}$ vectors are related to the $\vec{s}_{B,Y}$ vectors by

the equation Eq. (7.13), and that the components of $\vec{s}_B$ and $\vec{s}_Y$ can easily be broken down as in Eq. (7.14):

$$\begin{cases} \text{parallel:} & \vec{k}_B \cdot \vec{k}_Y = \alpha^2 \left(-(y_0)^2 - (x_0 + \frac{b}{2})(x_0 - \frac{b}{2}) \right) \\ \\ \text{anti-parallel:} & \vec{k}_B \cdot \vec{k}_Y = \alpha^2 \left((y_0)^2 + (x_0 + \frac{b}{2})(x_0 - \frac{b}{2}) \right) \end{cases} \tag{C.6}$$

For the first term, we multiply out which gives us:

$$\left(\sqrt{s} + \frac{2\alpha^2 \vec{s}_B^2}{x_B^2 \sqrt{s}} \right) \left(\sqrt{s} + \frac{2\alpha^2 \vec{s}_Y^2}{x_Y^2 \sqrt{s}} \right) = \left(s + 2\alpha^2 \left(\frac{\vec{s}_B^2}{x_B^2} + \frac{\vec{s}_Y^2}{x_Y^2} \right) + \frac{4\alpha^4 \vec{s}_B^2 \vec{s}_Y^2}{x_B^2 x_Y^2 s} \right) \tag{C.7}$$

by substituting these results into Eq. (C.5), we obtain:

$$\begin{cases} \text{parallel:} & x_B x_Y (s^* - s) = k + 2\alpha^2 \left(y_0^2 + x_0^2 - \frac{b}{2}^2 \right) \\ \\ \text{anti-parallel:} & x_B x_Y (s^* - s) = k - 2\alpha^2 \left(y_0^2 + x_0^2 - \frac{b}{2}^2 \right) \end{cases} \tag{C.8}$$

where:

$$k = 2\alpha^2 x_B x_Y \left(\frac{\vec{s}_B^2}{x_B^2} + \frac{\vec{s}_Y^2}{x_Y^2} \right) + \frac{4\alpha^4 \vec{r}_B^2 \vec{r}_Y^2}{x_B x_Y s} \tag{C.9}$$

For mid-rapidity, we have $x_B x_Y \approx x_B^2 \approx x_Y^2$ to first order, and we also have:

$$\left(\vec{r}_B^2 + \vec{r}_Y^2 \right) = \left(\left(x_0 + \frac{b}{2} \right)^2 + y_0^2 + \left(x_0 - \frac{b}{2} \right)^2 + y_0^2 \right) \tag{C.10}$$

Knowing that:

$$x_B x_Y (s^* - s) = (x_B x_Y)^{-1} (\hat{s}^* - \hat{s}) \tag{C.11}$$

we can substitute these last two equations into Eq. (C.8), which gives us:

$$\begin{cases} \text{parallel:} & (x_B x_Y)^{-1}(\hat{s}^* - \hat{s}) = 4\alpha^2 \vec{r}_0^2 + \frac{4\alpha^4 \vec{r}_B^2 \vec{r}_Y^2}{x_B x_Y s} \\ \text{anti-parallel:} & (x_B x_Y)^{-1}(\hat{s}^* - \hat{s}) = \alpha^2 b^2 + \frac{4\alpha^4 \vec{r}_B^2 \vec{r}_Y^2}{x_B x_Y s} \end{cases} \tag{C.12}$$

We can write:

$$\Delta\sqrt{\hat{s}} = (\sqrt{\hat{s}}^* - \sqrt{\hat{s}}) = \frac{\hat{s}^* - \hat{s}}{\sqrt{\hat{s}}^* + \sqrt{\hat{s}}} \approx \frac{\hat{s}^* - \hat{s}}{2\sqrt{s}} = \frac{(x_B x_Y)^{-1}(\hat{s}^* - \hat{s})}{2\sqrt{\hat{s}}} \tag{C.13}$$

and finally:

$$\begin{cases} \text{parallel:} & \Delta\sqrt{\hat{s}} = \frac{2\alpha^2 \vec{r}_0^2}{\sqrt{\hat{s}}} + \frac{4\alpha^4 \vec{r}_B^2 \vec{r}_Y^2}{x_B x_Y s^{3/2}} \\ \text{anti-parallel:} & \Delta\sqrt{\hat{s}} = \frac{\alpha^2 b^2}{2\sqrt{\hat{s}}} + \frac{4\alpha^4 \vec{r}_B^2 \vec{r}_Y^2}{x_B x_Y s^{3/2}} \end{cases} \tag{C.14}$$

Note that the extra term is identical for both cases so the difference in the change of $\sqrt{\hat{s}}$ is given by:

$$\delta\sqrt{\hat{s}} = \Delta\sqrt{\hat{s}}_{par} - \Delta\sqrt{\hat{s}}_{anti} = \frac{\alpha^2}{2\sqrt{\hat{s}}}\left(4\vec{r}_0^2 - b^2\right) \tag{C.15}$$

A change in $\sqrt{\hat{s}}$ translates as the same change in $\sqrt{s}$, so from now on we will use $\Delta\sqrt{s} = \sqrt{s}^* - \sqrt{s}$. To simplify things further for Monte Carlo simulation, we make the approximation that the momentum fractions are approximately equal in the central rapidity region, as well as being approximately equal to x_T. We used:

$$x_B = x_Y = x_T = \frac{2p_T}{\sqrt{s}} \tag{C.16}$$

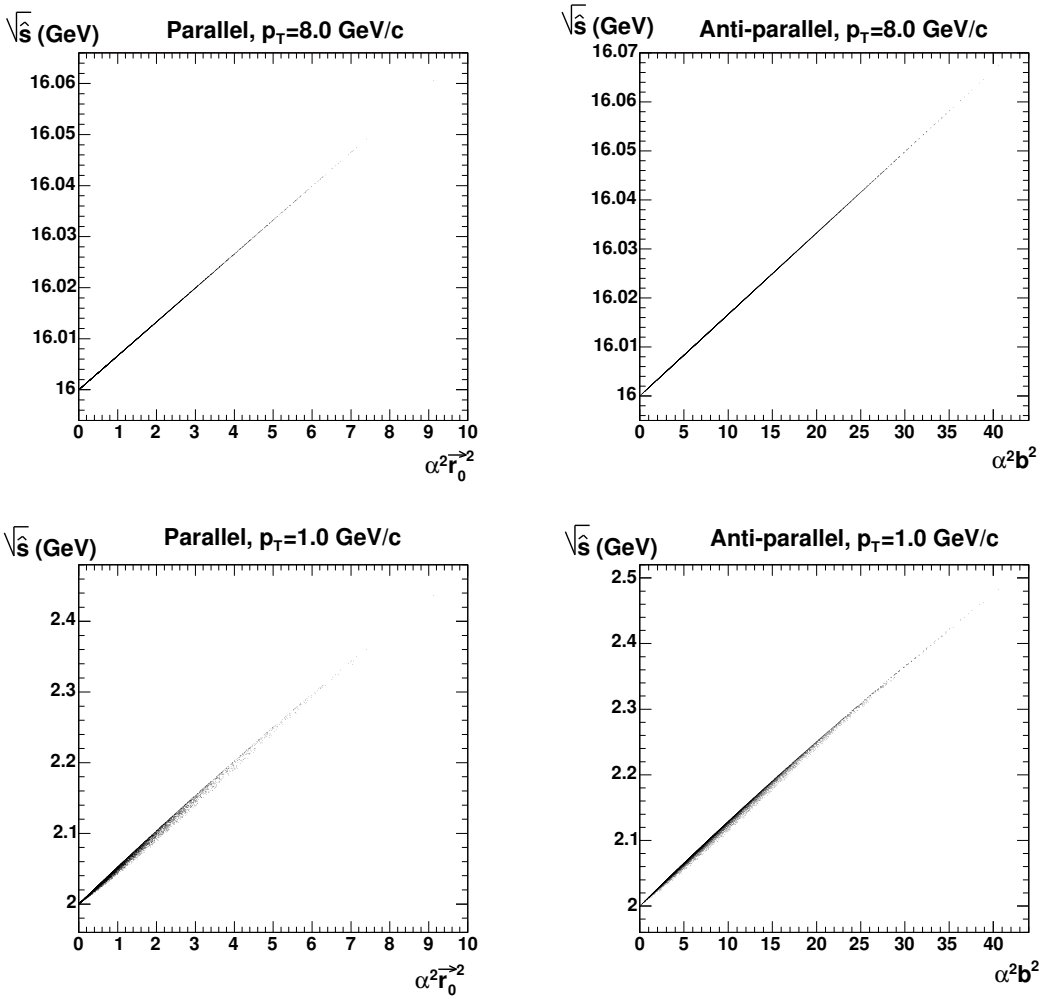

Figure C.2: $\Delta\sqrt{s}$ dependencies for parallel and anti-parallel helicity event simulation. *(top left)* shows the change in $\sqrt{s}$ ($\Delta\sqrt{s}$) for parallel helicity events at high p_T plotted versus the square of the interaction point vector, $\vec{r}_0$. *(top right)* A similar dependency of $\Delta\sqrt{s}$ on b^2 for high p_T anti-parallel helicity events is apparent. *(bottom left and right)* The same variables as in the top row are shown, but at low p_T. We see that the dependencies are smeared by the second terms in Eq. (C.14).

We ran the 3-Dimensional Monte Carlo model with Woods-Saxon potential (with $a = 5fm$) developed in Chapter 7 to randomly determine the impact parameter and interaction point. We then calculate $\sqrt{s}^*$ from Eq. (C.2) and Eq. (C.3) with the appropriate k_T values. The p_T input value was varied in steps of 0.2 GeV/c from 0.8 GeV/c to 8.0 GeV/c and 10,000 events were generated per helicity combination and per bin. Our results are shown in Fig. C.2 and Fig. C.3:

The dependencies on b^2 and $\vec{r}_0^2$ are shown in Fig. C.2. Note that at low p_T (small x) we see the appearance of slight smearing due to the second term in Eq. (C.14).

The distributions for the change in $\sqrt{s}$ values for parallel and anti-parallel helicity events are shown in Fig. C.3. We take the mean value for every bin and calculate the percentage deviation in the cross-section from the (unPOAM-altered) $\sqrt{s}$ cross-section for each p_T bin, knowing that there is a s^{-2} dependency [22]:

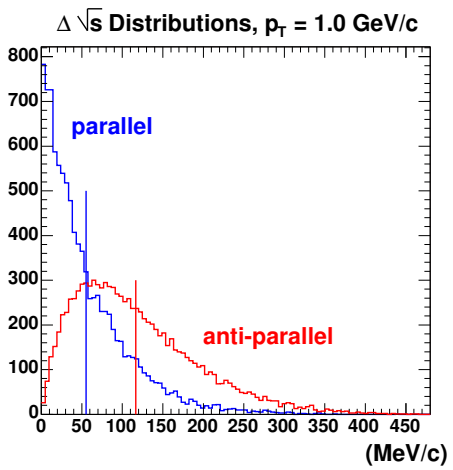

Figure C.3: $\Delta\sqrt{s}$ distributions for $p_T = 1.0$ GeV/c. The distributions for the two different helicity states are quite different. The vertical lines represent the means, which are the values used per bin for the calculation of the asymmetry.

$$\Delta\sigma = \frac{s^{-2} - (\sqrt{s} + \Delta\sqrt{s})^{-4}}{s^{-2}} = 1 - \frac{s^2}{(\sqrt{s} + \Delta\sqrt{s})^4} \tag{C.17}$$

The results are shown in Fig. C.4. We see a smaller cross-section than without p_T. Because the anti-parallel events have on average a greater $k_{TB} \cdot k_{TY}$, this results in a greater $\Delta\sqrt{s}$, which in turn gives a smaller cross-section. Since we define our asymmetries as the difference between the parallel and anti-parallel helicities, the difference (and A_{LL}) is positive. We note a larger effect at lower p_T (smaller x).

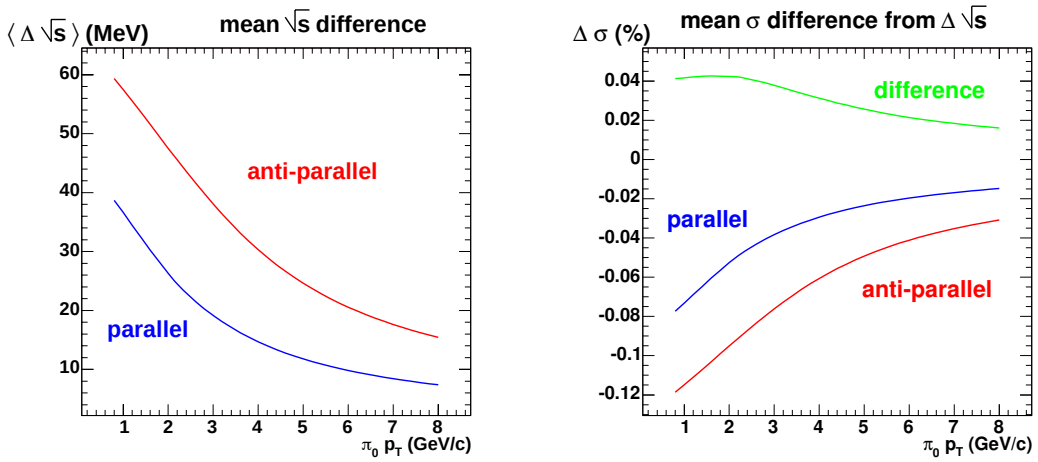

Figure C.4: $\Delta\sqrt{s}$ effect results. *(left)* The mean values for $\Delta\sqrt{s}$ per bin are fitted to show a p_T dependency. *(right)* The change in cross-section is shown: we see a negative effect, the greater the change in $\sqrt{s}$, the smaller the cross-section. The green line shows the difference in the two effects, and is positive. This is only the difference between the red and blue lines and not A_{LL}. The two quantities are related by: $\delta\sigma \approx 2A_{LL}$.

C.3 The k_T Kick in p_T

A second effect to consider when including POAM in the measurement of π^0 A_{LL} is that the addition of the k_T from POAM might affect the "natural" value of the π^0 p_T. The measured p_T is the sum of the p_T due to the physics interaction between colliding protons, which we will denote p_{T0} modified by an eventual k_T push due to

orbiting constituents as shown in Fig. C.5.

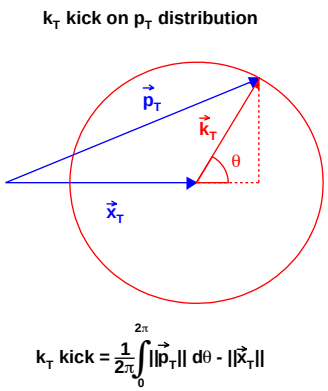

Figure C.5: The measured p_T of the π^0 is modified by the k_T due to POAM. Because of the lack of information regarding the k_T direction relative to the jet-jet direction, we must assume an isotropic distribution. The mean k_T kick is obtained by integrating over 2π.

The relative direction of the jets and the k_T kick is unknown and assumed to be isotropic. We take the average value of the integral over all azimuthal angles:

$$k_{T\,kick}(p_{T0}, k_T) = \frac{1}{2\pi}\int_0^{2\pi} p_T d\theta - p_{T0} \tag{C.18}$$

where:

$$p_T = \sqrt{(p_{T0} + k_T \cos\theta)^2 + (k_T \sin\theta)^2} \tag{C.19}$$

In order to be consistent with the previous section, we will choose the 3-dimensional model with Woods-Saxon ($a = 5fm$) density distribution. The values we use for k_T in Eq. (C.19) are the mean values for the parallel and anti-parallel helicities found by modeling in Chapter 7 and shownn in Fig. 7.7: 633 MeV/c for simulated parallel helicity events and 435 MeV/c for anti-parallel helicity events. Note that those

values were calculated at the partonic level and so when we integrate Eq. (C.18) numerically, we will use $\hat{p}_T$, the partonic p_T as input, and our output will be the partonic k_T kick: $\hat{k}_{Tkick}$. Our $\hat{p}_T$ values range from 1.0 GeV/c to 12.0 GeV/c in steps of 0.2 GeV/c. The values for $\hat{k}_{Tkick}$ are plotted and fitted in Fig. C.6.

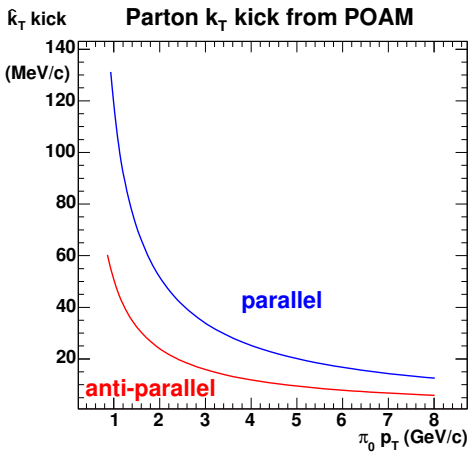

Figure C.6: Net $\hat{k}_T$ kick due to POAM as a function of parton p_T. A greater effect is noted for the parallel helicity events, as was expected (see Chapter 7).

In order to obtain the k_T kick for π^0 p_T we must modify the graph in Fig. C.6 by z, the ratio of the partonic transverse momentum to the detected hadronic transverse momentum.

$$z = \frac{p_T}{\hat{p}_T} \tag{C.20}$$

We know that the ratio of k_T kick to p_T is the same for the π^0 and the parton, and use z as a function of π^0 p_T to find the corresponding $\hat{p}_T$. From PYTHIA simulation we can plot the values of z as a function of π^0 p_T. At higher p_T where the values start to fluctuate through lack of statistics, we fit an assymtotic function:

$$z(p_T) = A\left(1 - e^{-kp_T}\right) \tag{C.21}$$

We can then plot the k_T kick as a function of π^0 p_T (Fig. C.7).

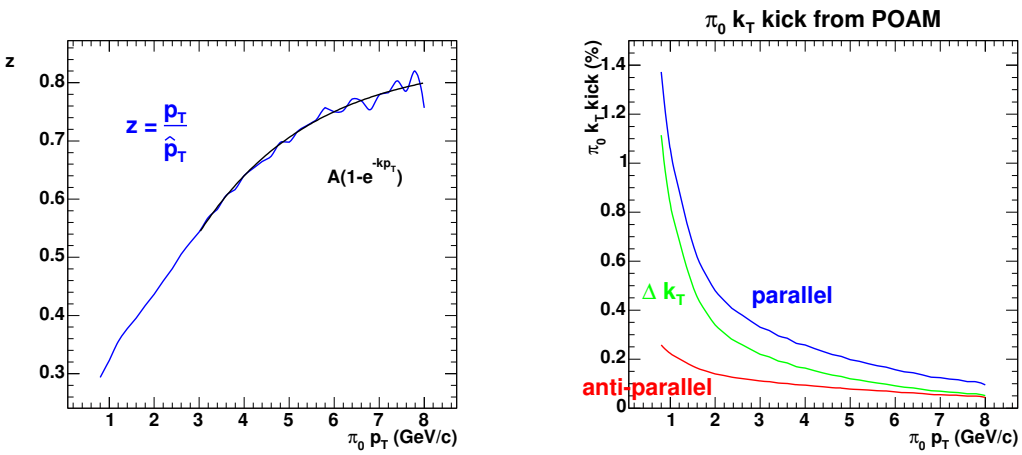

Figure C.7: *(left)* shows the z distribution as a function of π^0 p_T. *(right)* Net k_T kick due to POAM as a function of π^0 p_T.

This k_T kick pushes the cross-section graphs toward positive x direction. Asymmetry is measured as a function of p_T, *i.e.* in the y direction (see Fig. C.8). Using the k_T kick results we can calculate the asymmetries in cross-section, knowing that the p_T distribution of π^0 is proportional to $(p_T)^{-4}$ [22]. The modified cross-section is given by:

$$\sigma_{par,anti} = \frac{\alpha}{(p_{T0} - k_{Tpar,anti})^4} \tag{C.22}$$

where $k_{Tpar,anti}$ is not the k_T kick calculated at p_{T0} (using the notation of Fig. C.8), but the k_T calculated at p_{Tpar} and p_{Tanti}, respectively. In other words, the new parallel and anti-parallel cross-sections are calculated with the p_T value had there been no k_T kick. The k_T values to be subtracted for calculation of $\sigma_{par,anti}$ are calculated from the right graph in Fig. C.7.

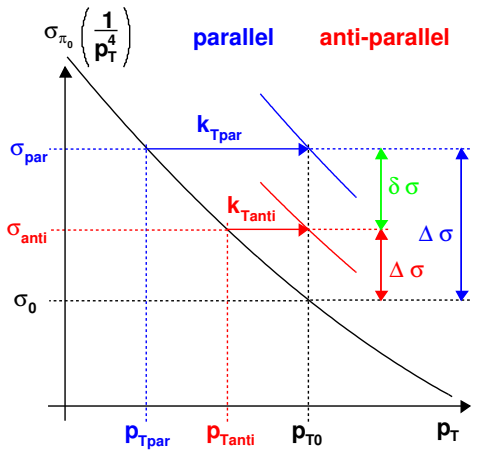

Figure C.8: From k_T kick to σ asymmetry. The $k_{T\,par,anti}$ values to be subtracted for calculation of $\sigma_{par,anti}$ are calculated from the right graph in Fig. C.7, then substituted into Eq. (C.22).

The results are shown in Fig. C.9 and combined with the cross-section asymmetry due to the modified partonic $\sqrt{s}$ calculated in the previous section. The combined results for certain π^0 p_T values are given in Table C.1.

In the second graph the different A_{LL} functions are calculated by:

$$A_{LL} = \frac{\sigma_{par} - \sigma_{anti}}{\sigma_{par} + \sigma_{anti}} \tag{C.23}$$

then multiplied by the Run3pp beam polarizations to give an estimated measured effect. The effect is much greater for the k_T kick than for $\Delta\sqrt{s}$ which reflects the ${p_T}^{-4}$(or s^{-2}) dependence and how a small horizontal shift in the graph causes a large shift in the vertical direction.

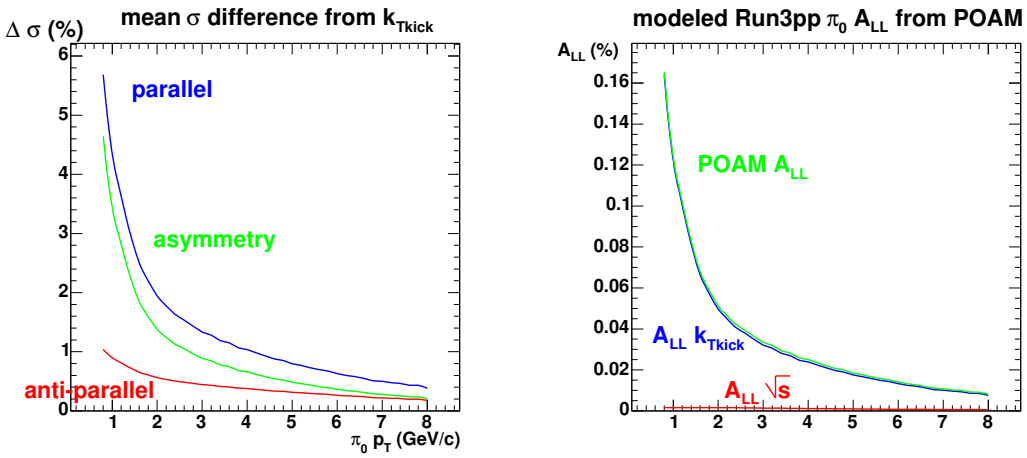

Figure C.9: π^0 A_{LL} due to POAM. *(left)* The change in the cross-sections given as a percentage of the unmodified cross-sections is shown. *(right)* The A_{LL} due to POAM (green line) is the sum of the A_{LL} due to the asymmetry in the modification of the $\sqrt{s}$ and the A_{LL} due to the asymmetry in mean k_T kick. A_{LL} has been multipled by the beam polarizations for Run3pp to give an estimate of an expected measured effect.

Monte Carlo	$p_T = 1.0$ GeV/c	$p_T = 3.0$ GeV/c	$p_T = 8.0$ GeV/c
A_{LL} theory	1.7%	0.46%	0.11%
A_{LL} Run3pp	0.12%	0.033%	0.0081%
A_{LL} Run5pp	0.38%	0.10%	0.024%

Table C.1: Monte Carlo π^0 A_{LL} from POAM results. The first row is the theoretical value calculated, while the Run3pp and Run5 values have been multiplied by $P_B P_Y$.

C.4 Conclusion

The purpose of this simulation is not to discredit the π^0 A_{LL} analysis. Nor are we claiming that a π^0 A_{LL} result or lack thereof is necessarily a consequence of POAM. For starters let us remind ourselves that these results are based on a classical model of the proton with an arbitrary scale of constant $p_\theta = 300\text{MeV}/c$ at a proton radius of $1.3fm$. Even so, for Run3pp, the effect is estimated to be small even at low p_T where POAM would have the greatest impact. Nevertheless, it is important to consider the different possible sources of asymmetry present in all asymmetry measurements and to keep in mind the complex relationships at play.

To first order a π^0 A_{LL} result will most certainly be a consequence of ΔG. In the case of confirmed zero results, however, interpretation becomes more difficult, as POAM could play a role. In Run5 with an increased polarization a larger (though still rather small) effect is expected (Table C.1). A zero result (or a small result on the scale of our calculated asymmetry) with enough precision might also have consequences for POAM; although disentangling that information from ΔG is as problematic as the opposite. ΔG could be very small or zero, POAM could be very small or zero, our model could be inaccurate, ΔG and POAM could cancel or contribute equally in π^0 A_{LL} or nearly any combination of these factors are part of a long list of possible explanations.

References

[1] R. Feynman, Phys. Rev. Lett. **23**, 1415 (1969).

[2] A. W. Thomas and W. Weise, *The Structure of the Nucleon* (WILEY-VCH GmbH, Berlin Germany, 2001).

[3] C. Caso *et al.*, Eur. Phys. J. **C 3**, 1 (1998).

[4] L. Bourhis, M. Fontannaz, J. P. Guillet, and M. Werlen, Eur. Phys. J. **C19**, 89 (2001).

[5] A. Martin *et al.*, Eur. Phys. J. **C 4**, 463 (1998).

[6] J. Ashman *et al.*, Phys. Lett. **B206**, 364 (1988).

[7] J. Ashman *et al.*, Nucl. Phys. **B328**, 1 (1989).

[8] B. Adeva *et al.*, Phys. Rev. **D58**, 112002 (1998).

[9] P. L. Anthony *et al.*, Phys. Rev. **D54**, 6620 (1996).

[10] K. Abe *et al.*, Phys. Rev. **D58**, 112003 (1998).

[11] K. Abe *et al.*, Phys. Rev. Lett. **79**, 26 (1997).

[12] P. L. Anthony *et al.*, Phys. Lett. **B463**, 339 (1999).

[13] K. Ackerstaff *et al.*, Phys. Lett. **B404**, 383 (1997).

[14] A. Airapetian *et al.*, Phys. Lett. **B442**, 484 (1998).

[15] A.D.Martin *et al.*, Phys. Lett. **B604**, 61 (2004).

[16] K. Kurek, Nucl. Phys. **A755**, 321 (2005).

[17] S. S. Adler *et al.*, Phys. Rev. Lett. **93**, 202002 (2004).

[18] M. Hirai, S. Kumano, and N. Saito, Phys. Rev. **D69**, 054021 (2004).

[19] T.-C. Meng, J.-C. Pan, Q.-B. Xie, and W. Zhu, Phys. Rev. **D40**, 769 (1989).

[20] S. Brodski, *Orbital Angular Momentum on the Light-Front and QCD Observables* (Joint UNM/RBRC Workshop on Parton Orbital Angular Momentum, Upton NY, 2006).

[21] F. W. Busser *et al.*, Phys. Lett. **B46**, 471 (1973).

[22] N. Ajitanand *et al.*, PHENIX PPG029, 2005.

[23] M. Tannenbaum and J. Rak, PHENIX AN455, 2005.

[24] L. Apanasevich *et al.*, Phys. Rev. **D59**, 074007 (1999).

[25] S. S. Adler *et al.*, Phys. Rev. Lett. **92**, 051802 (2004).

[26] X.-D. Ji, Phys. Rev. **D55**, 7114 (1997).

[27] F. Sabatié, Nucl. Phys. **A755**, 81 (2005).

[28] D. E. Fields, *Orbital Angular Momentum from Helicity Dependent k_T* (Joint UNM/RBRC Workshop on Parton Orbital Angular Momentum, Upton NY, 2006).

[29] C. Aidala, *Transverse Spin at PHENIX: Results and Prospects* (Transversity 2005, Como Italy, 2005).

[30] D. Adams, Phys. Lett. **B261**, 261 (1991).

[31] D. Sivers, Phys. Rev. **D41**, 83 (1990).

[32] D. Sivers, Phys. Rev. **D43**, 261 (1991).

[33] J. Adams, Phys. Rev. Lett. **92**, 171801 (2004).

[34] D. Sivers, *Process Dependence of Single-Spin Asymmetries from Orbital Structures* (Joint UNM/RBRC Workshop on Parton Orbital Angular Momentum, Upton NY, 2006).

[35] J. Collins, Nucl. Phys. **B396**, 161 (1993).

[36] F. Yuan, *Can we learn quark orbital motion from the SSAs?* (Joint UNM/RBRC Workshop on Parton Orbital Angular Momentum, Upton NY, 2006).

[37] A. Radyushkin, Phys. Lett. **B 380**, 417 (1996).

[38] X.-D. Ji, Phys. Rev. Lett. **78**, 610 (1997).

[39] M. Anselmino, *The average intrinsic $k_\perp$ of quarks* (Joint UNM/RBRC Workshop on Parton Orbital Angular Momentum, Upton NY, 2006).

[40] W. Vogelsang, *Some thoughts on the helicity dependence of jet k_T* (Joint UNM/RBRC Workshop on Parton Orbital Angular Momentum, Upton NY, 2006).

[41] I. Alekseev *et al.*, Nucl. Instrum. Meth. **A499**, 392 (2003).

[42] I. Alekseev *et al.*, Configuration Manual Polarized Proton Collider at RHIC.

[43] J. J. Woods, Ph.D. thesis, UCLA, 2005.

[44] K. Adcox *et al.*, Nucl. Instrum. Meth. **A499**, 469 (2003).

[45] M. Allen *et al.*, Nucl. Instrum. Meth. **A499**, 549 (2003).

[46] A. K. *et al.*, Nucl. Instrum. Meth. **A499**, 489 (2003).

[47] A. S. H. *et al.*, Nucl. Instrum. Meth. **A499**, 480 (2003).

[48] A. M. *et al.*, Nucl. Instrum. Meth. **A499**, 508 (2003).

[49] A. H. *et al.*, Nucl. Instrum. Meth. **A499**, 537 (2003).

[50] A. Hoover, Ph.D. thesis, New Mexico State University, 2003.

[51] J. Newby, Ph.D. thesis, University of Tennessee, 2003.

[52] A. Al-Jamel, Ph.D. thesis, New Mexico State University, 2004.

[53] A. Bazilevsky *et al.*, PHENIX AN225, 2003.

[54] A. Bazilevski *et al.*, *Measurement of Single Transverse-spin Asymmetry in Forward Production of Photons and Neutrons in pp Collisions at $\sqrt{s}$= 200 GeV* (AIP Conference Proceedings, Melville NY, 2003).

[55] H. Sato, Ph.D. thesis, Kyoto University, 2003.

[56] S. Adler *et al.*, Nucl. Instrum. Meth. **A499**, 560 (2003).

[57] A. L. S. Angelis *et al.*, Phys. Lett. **B97**, 163 (1980).

[58] M. Della Negra *et al.*, Nucl. Phys. **B127**, 1 (1977).

[59] J. Rak *et al.*, PHENIX AN251, 2003.

[60] N. Grau *et al.*, PHENIX AN329, 2004.

[61] S. S. Adler *et al.*, Phys. Rev. Lett. **91**, 241803 (2003).

[62] C. Aidala *et al.*, PHENIX AN224, 2003.

[63] A. Bazilevsky *et al.*, PHENIX AN277, 2004.

[64] A. Bazilevsky *et al.*, PHENIX AN471, 2005.

[65] K. Tanida *et al.*, PHENIX AN222, 2003.

[66] I. From *et al.*, Phys. Rev. **C28**, 2565 (1983).

[67] G. Pauletta *et al.*, Phys. Rev. **C27**, 282 (1983).

[68] N. H. Buttimore *et al.*, Phys. Rev. **D18**, 694 (1978).

[69] B. Kopeliovich and T. Trueman, Phys. Rev. **D64**, 034004 (2001).

[70] J. Tojo, Phys. Rev. Lett. **89**, 052302 (2002).

[71] C. E. Allgower *et al.*, Phys. Rev. **D65**, 092008 (2002).

[72] M. Hauger *et al.*, Nucl. Instrum. Meth. **A462**, 382 (2001).

[73] I. Bojak and M. Stratmann, Phys. Rev. **D67**, 034010 (2003).

[74] H. Sato *et al.*, PHENIX AN482, 2004.